# Metrology Of Sub-10 nm Block Copolymers To Control The Crystallization And Microphase Separation

**Dissertation**

zur Erlangung des Doktorgrades

an der Fakultät für Mathematik, Informatik und Naturwissenschaften

Fachbereich Physik

der Universität Hamburg

vorgelegt von

**Alexander Said Meinhardt**

Hamburg

2025

| | |
|---|---|
| Gutachter/innen der Dissertation: | Prof. Dr. Dorota Koziej<br>Dr.-Ing. Thomas F. Keller |
| Zusammensetzung der Prüfungskommission: | Prof. Dr. Daniela Pfannkuche<br>Prof. Dr. Dorota Koziej<br>Dr.-Ing. Thomas F. Keller<br>Prof. Dr. Patrick Huber<br>Prof. Ph.D. Ivan Maximov |
| Vorsitzende/r der Prüfungskommission: | Prof. Dr. Daniela Pfannkuche |
| Datum der Disputation: | 21.08.2025 |
| Vorsitzender des Fach-Promotionsausschusses PHYSIK: | Prof. Dr. Wolfgang J. Parak |
| Leiter des Fachbereichs PHYSIK: | Prof. Dr. Markus Drescher |
| Dekan der Fakultät MIN: | Prof. Dr.-Ing. Norbert Ritter |

# Abstract

Properties of polymers are largely governed by their structure on the nanoscale. Therefore, precise control over polymer morphology enables novel design strategies for bottom-up nanofabrication and the tailored fabrication of emerging functional nanomaterials. However, the vast structural and chemical diversity of polymers requires extensive case-by-case investigation, resulting in a sustained effort to elucidate the relationship between morphology and properties. Especially in thin films, the nanoscale modulation of the topography leads to pronounced interfacial effects, with direct implications for the development of structured, functional nanomaterials.

This cumulative thesis studies dynamic processes in polymer thin films with *in situ* Atomic Force Microscopy (AFM), aiming to provide specific suggestions and developing novel strategies for the design of nanomaterials.

First, a conductive, perchlorate-doped polypyrrole (PPY) thin film is investigated using *in situ* electrochemical Atomic Force Microscopy (EC-AFM). In electrolyte, the film thickness, roughness, and elastic properties closely follow the applied electric potential, revealing a correlation between film topography and elastic properties. Repeated potential cycling results in osmotic expansion of the film and passive swelling. Furthermore, the rough nodular PPY topography leads to a highly heterogeneous distribution of the elastic modulus on the film surface. These findings have important implications for the future design of conductive polymer interfaces in electroactive devices, potentially improving overall device lifetime and performance.

The design of interfaces is particularly relevant in the field of block copolymer (BCP) thin films, since interfacial energies govern the orientation of microphase-separated BCP domains. Bottom-up self-assembly techniques have emerged as a promising tool for the fabrication of patterned surface nanostructures. However, for next-generation lithography, nanofabrication has to advance towards the sub-10 nm regime, requiring the development of highly segregating, short-chain BCPs, so-called 'high $\chi$, low $N$' BCPs.

In the second study, thin films of a double-crystalline, short-chain poly(ethylene)-*block*-poly(ethylene oxide) (PE-*b*-PEO) are investigated on neutral substrates using *in situ* AFM with a heating stage. It is demonstrated how the BCP films form defined, extended-chain vertical lamellae during thermal annealing. The lamellae formation mechanism is identified as breakout crystallization, which disrupts

the initially microphase separated morphology. This is attributed to the surface energy changes associated with crystallization of extended-chain crystals. Additionally, the results demonstrate that macroscopic alignment of the nanolamellae is achievable with physical guiding patterns, providing a novel pathway for bottom-up nanofabrication towards the sub-10 nm regime. These findings illustrate how the effective segregation strength can be improved by crystallization and that extended-chain crystallization offers a unique way of direct control over the pitch of the lamellar nanostructures.

Furthermore, the PE-*b*-PEO thin films are exposed to solvent vapor atmosphere to investigate the influence of solvent exposure on the annealing dynamics and morphology. By varying the solvent vapor annealing (SVA) conditions, standing cylinder morphologies or vertical lamellae can be observed. It is found that the final SVA morphologies are significantly affected by the initial chain orientation in the film due to slow kinetics at the chosen annealing temperature. Although the solvent promotes chain mobility in the BCP to some degree, the low annealing temperature restricts structural reorganization during SVA. These results emphasize the need to extensively study the chain kinetics during SVA in order to elucidate potential kinetic pathways for the formation of surface nanostructures.

In conclusion, the present work illustrates that the interfaces of polymers play a pivotal role in influencing the morphology and properties of polymer thin films. Correlating internal structure and surface effects is essential for further advancing polymer-based nanotechnology and developing novel functional nanomaterials. Furthermore, dynamic *in situ* studies of these processes are crucial for understanding the structure-property relationship in polymer thin films. Therefore, this work contributes to the efforts in the development of novel bottom-up nanofabrication techniques by providing valuable insights to the structure-property relationship of polymers.

# Zusammenfassung

Die Eigenschaften von Polymeren sind in erster Linie auf ihre Morphologie im Nanometerbereich zurückzuführen. Eine präzise Kontrolle der Polymermorphologie ermöglicht neuartige Konzepte für 'bottom-up' Nanofabrikation und die Entwicklung zukünftiger funktionaler Nanomaterialien. Allerdings erfordert die enorme strukturelle und chemische Vielfalt von Polymeren umfangreiche Untersuchungen zu jedem einzelnen Polymersystem, um den Zusammenhang zwischen Morphologie und Eigenschaften zu erforschen. Vor allem in Dünnfilmen führt die Modulation der Topographie im Nanometerbereich zu ausgeprägten Grenzflächeneffekten, was direkte Auswirkungen auf die Entwicklung strukturierter, funktionaler Nanomaterialien nach sich zieht.

Diese kumulative Arbeit untersucht dynamische Prozesse in Polymerdünnfilmen mit *in situ* Rasterkraftmikroskopie (AFM), um konkrete Vorschläge und neuartige Strategien für das Design von Nanomaterialien zu entwickeln.

In der ersten Studie wird ein leitfähiger, Perchlorat-dotierter Polypyrrol (PPY) Dünnfilm mittels *In-situ* Elektrochemie-AFM (EC-AFM) untersucht. In einer Elektrolytlösung folgen die Filmdicke, Rauigkeit und elastische Eigenschaften dem angelegten elektrischen Potenzial, was eine Korrelation zwischen Filmtopographie und elastischen Eigenschaften nachweist. Wiederholtes, zyklisches Fahren des Potenzials führt zu osmotisch bedingter Ausdehnung und passivem Schwellen des Films. Zusätzlich führt die raue, nodulare Topographie des Polypyrrols zu einer stark heterogenen Verteilung des Elastizitätsmoduls auf der Oberfläche des Dünnfilms. Diese Ergebnisse haben wichtige Implikationen für das zukünftige Design leitfähiger Polymer-Grenzflächen in elektroaktiven Materialien und könnten die Lebensdauer sowie die Leistung dieser Bauteile insgesamt verbessern.

Das Design von Grenzflächen ist in Blockcopolymer (BCP) Dünnfilmen von besonderer Bedeutung, da die Grenzflächenenergien die Orientierung der mikrophasenseparierten Blockcopolymerdomänen bestimmen. 'Bottom-up' Selbstassemblierungstechniken bieten vielversprechende Möglichkeiten für die Herstellung oberflächenstrukturierter Nanostrukturen. Allerdings müssen Lithografietechniken der nächsten Generation Strukturen im Bereich unter zehn Nanometer ('sub-10 nm') herstellen können, was die Entwicklung stark segregierender, kurzkettiger Blockcopolymere, sogenannten 'high $\chi$, low $N$' Blockcopolymeren, erfordert.

In der zweiten Studie werden Dünnfilme eines doppelkristallinen, kurzkettigen Polyethylen-block-polyethylenoxids (PE-b-PEO) auf neutralen Substraten mittels

*In-situ* AFM und eines Heizsystems untersucht. Es wird gezeigt, wie die Blockcopolymer-Dünnfilme durch Wärmebehandlung vertikale Lamellen aus gestreckten Ketten bilden. Der Mechanismus der Lamellenbildung wird als Ausbruchskristallisation ('breakout' crystallization) identifiziert, welche die ursprünglich mikrophasenseparierte Morphologie überschreibt. Dies wird auf die Änderung der Oberflächenenergie bei der Kristallisation gestreckter Kettenkristalle zurückgeführt. Darüber hinaus zeigen die Ergebnisse, dass eine makroskopische Ausrichtung der Nanolamellen mit physischen Führungsmustern möglich ist, was einen neuartigen Ansatz für die 'bottom-up' Nanofabrikation im Bereich unter 10 nm ermöglicht. Diese Ergebnisse verdeutlichen, wie die effektive Segregationsstärke durch Kristallisation verbessert werden kann, und dass die Kristallisation gestreckter Ketten eine einzigartige Möglichkeit bietet, die Periode der lamellaren Nanostrukturen direkt zu kontrollieren.

Zusätzlich werden die PE-b-PEO Dünnfilme unter einer Atmosphäre aus Lösungsmitteldampf untersucht, um den Einfluss des Lösungsmittels auf die Dynamik und Morphologie während der Behandlung mit Lösungsmitteldampf (Solvent Vapor Annealing, kurz SVA) zu ermitteln. Durch Variation der SVA-Bedingungen können stehende Zylindermorphologien oder vertikale Lamellen beobachtet werden. Die finalen Morphologien nach dem SVA sind durch die anfängliche Orientierung der Ketten im Film gegeben, da die Kinetik im Film bei der gewählten Behandlungstemperatur verlangsamt ist. Obwohl das Lösungsmittel im Film die Mobilität der Ketten zum Teil fördert, schränkt die niedrige Behandlungstemperatur die strukturelle Reorganisation bei der Lösungsmittelbehandlung ein. Diese Ergebnisse verdeutlichen die Notwendigkeit, die Kinetik der Ketten während dem SVA umfassend zu untersuchen, um potenzielle kinetische Wege für die Bildung von Oberflächennanostrukturen zu finden.

Zusammenfassend zeigt die vorliegende Arbeit, dass die Grenzflächen von Polymeren eine entscheidende Rolle bei der Beeinflussung der Morphologie und der Eigenschaften von dünnen Polymerfilmen spielen. Die Korrelation zwischen interner Struktur und Oberflächeneffekten ist für die Weiterentwicklung der Nanotechnologie auf Polymerbasis und die Entwicklung neuartiger funktioneller Nanomaterialien unerlässlich. Dynamische *In-situ* Studien dieser Prozesse können entscheidend zum Verständnis der Zusammenhänge zwischen Struktur und Eigenschaften in dünnen Polymerfilmen beitragen. Somit leistet diese Arbeit einen wichtigen Beitrag zur Entwicklung neuartiger 'bottom-up' Techniken zur Nanofabrikation.

# Contents

# List of Figures

# List of Tables

# Acronyms

**AFM** Atomic Force Microscopy

**BCP** block copolymer

**DMT** Derjaguin-Muller-Toropov

**DSA** directed self-assembly

**EC-AFM** electrochemical Atomic Force Microscopy

**EP** electropolymerization

**HOMO** highest occupied molecular orbital

**JKR** Johnson-Kendall-Roberts

**LUMO** lowest unoccupied molecular orbital

**M3M** methyl-3-mercaptopropionate

**OWRK** Owens, Wendt, Rabel and Kälble

**PE** polyethylene

**PE-*b*-PEO** poly(ethylene)-*block*-poly(ethylene oxide)

**PEO** polyethylene oxide

**PPY** polypyrrole

**QNM** quantitative nanomechanical mapping

**SVA** solvent vapor annealing

**TA** thermal annealing

# Nomenclature

$\chi$ Flory-Huggins interaction parameter

$\chi_{eff}$ Effective Flory-Huggins interaction parameter

$\Delta\omega_{12}$ Exchange energy

$\Delta G$ Gibbs free energy

$\Delta H$ Free enthalpy

$\Delta S$ Free entropy

$\Delta T$ Temperature difference/supercooling

$\delta$ Indentation depth for nanoindentation and polypyrrole. Otherwise: Solubility parameter

$\delta_{p,d,h}$ Polar, disperse, and hydrogen contribution to solubility parameter

$\gamma'$ or $\sigma'$ Cilia surface energy

$\gamma_L$ or $\sigma^l$ Lateral surface energy

$\nu$ Poisson's ratio

$\sigma$ or $\gamma$ Surface tension

$\sigma^{p,d}$ or $\gamma^{p,d}$ Polar or disperse contribution to surface tension

$\sigma_e$ Fold surface energy

$\sigma_{A-B}$ or $\gamma_{A-B}$ Interfacial energy between A and B

$\theta$ Contact angle

$\theta_C$ Critical contact angle

$d$ or $L$ Layer thickness

$d_{ext}$ Extended chain length

$E$ Elastic modulus (Young's modulus)

$E^*$ Reduced elastic modulus

$F$ Force

$f_i$ or $\phi_i$ Volume fraction (block length ratio)

$F_{adh}$ Adhesion force

$F_{max}$ Peak force

$F_{pi}, F_{di}, E_{hi}$ Polar, disperse, and hydrogen group contributions to solubility parameter

$k$ Boltzmann constant

$l$ Lamellar stem length

$l_{min}$ Smallest stable lamellar stem length

$M_N$ Number-average molecular weight

$M_n$ Molar mass

$M_W$ Weight-average molecular weight

$N_A$ Avogadro constant

$N_i$ Number of polymers within fraction

$p/p_{sat}$ Degree of saturation of solvent vapor pressure

$R$ Tip radius for nanoindentation and polypyrrole. Otherwise: Gas constant

$r$ Segment-size in Flory-lattice; for polymers = polymerization degree

$R^*$ Critical radius of nucleus

$S$ Tip-sample separation

$T$ Temperature

$T_c$ Crystallization temperature

$T_g$ Glass transition temperature

$T_m$ Melting temperature

$T_m^\infty$ Melting temperature of perfect, infinite polymer crystal

$T_{ODT}$ Order-disorder-transition temperature

$V$ or $V_m$ Molar volume

$W_i$ Weight of polymer fraction

$z$ Lattice coordination number

$Z_c$ Cantilever deflection

$Z_p$ Piezo position

$\mathbf{P_S}$ Parachor

PDI Polydispersity index

# 1. Introduction

Functional nanomaterials based on soft matter, such as polymers, play an pivotal role in existing and emerging technologies.[1] Generally, polymers posses high flexibility, biocompatibility, inexpensive production, and exact tailoring of their functionality through the synthesis route, enabling them to cover a wide range of potential applications. For example, highly conductive polymers find application as actuators in 'artificial muscles', organic solar cells, sensors, or supercapacitors for energy storage.[2–5] Other types of polymers, such as block copolymers, are used for their inherent ability to form ordered nanostructures via self-assembly, which paves the way for their use in photolithography and microfabrication of low-cost, easily scalable templates and masks, as well as in photonics, as adhesives, or as membranes.[6–8]

However, there remain many challenges associated with the design of polymeric functional nanomaterials. The width of applications for polymers, stemming from the variety in structure and properties of the polymer chains, requires a detailed understanding of the fundamental processes within the polymer system.[1] Especially thin polymer films play a crucial role in various devices and applications. The properties of these films often deviate significantly from their bulk counterparts as a result of pronounced interfacial effects and their high surface-to-volume ratio. As a consequence, the modulation of interfaces gives rise to spatial heterogeneity and dynamic behavior of the film when it is exposed to conditions that closely mimic real life. The spatial heterogeneities and dynamic behavior in thin films, as well as the influence of topography on polymer properties, enable linking polymer structure and properties, thus opening pathways for the development of functional nanomaterials.[9]

One example is the redox behavior of conductive polymer thin films in aqueous solutions, leading to diffusion of ions and solvent into or out of the film. This causes a volume change, which can be either advantageous for, e.g., electromechanical actuator applications, or detrimental for, e.g., electrode materials. Since the volume change depends on film porosity, which is controlled by the deposition protocol and chemical environment used during electropolymerization, it becomes clear that internal film structure and actuation strength are linked together.[10] Additionally, the thin film topography influences the elastic properties of thin films. Adhesion and elastic modulus can be tuned to improve cell adhesion, enabling the application of conductive polymer films as biomaterials.[4, 11]

Another example is the complex formation mechanism of heterogeneous surface nanostructures based on self-assembly of block copolymer (BCP) thin films. Strongly segregating copolymer blocks with low molar mass (block lengths) can be employed in order to generate sub-10 nm features with high spatial resolution.[12, 13] The miniaturization demand of the microelectronics industry has motivated the development of sub-10 nm nanofabrication methods using so-called high-$\chi$, low-$N$ BCPs. While the microphase separation caused by the chemical incompatibility of the different copolymer blocks is an inherent property of the BCP, the confinement in thin films, and the interfacial energies at the interfaces strongly influences the morphology.[6, 14] Although BCP surface nanostructures for, e.g., high resolution photolithography demonstrate the vast technological potential of BCPs, precise control over the orientation and alignment of the microdomains is required.[7, 8, 15] This control can be achieved via directed self-assembly (DSA).[16] Furthermore, BCP crystallization can be exploited to control the orientation of the crystalline microdomains. The final morphology depends on the competition between microphase separation and crystallization, resulting in various complex phenomena occurring during the crystallization of double-crystalline BCPs.[17]

Thin polymer films exhibit striking dynamic properties, such as the volume change of conductive polymer films under an applied electric potentials. These properties have direct practical implications for thin film applications, highlighting the need for appropriate tools to investigate such dynamic processes.[9] Atomic Force Microscopy (AFM) is such a tool for elucidating the structure and properties of polymer surfaces. With AFM, the surface morphology and topography can be imaged with high spatial resolution under *in situ* conditions, while simultaneously measuring and mapping physical properties. This provides unique means for linking structure to properties, deciphering their relationship, and opening pathways for the development of more advanced materials.[9]

## 1.1. Scope of Thesis

Following the general introduction, the next chapter (Section 2.) introduces the basic concepts of polymer physics and explains polymer terminology as well as properties relevant to this thesis, such as polymer crystallization. Special emphasis is placed on conductive polymers and crystallizable BCPs.

Next, Section 3. illustrates the operating principle of AFM, a real-space scanning technique which uses a sharp tip to probe sample topography, addresses its

resolution limits, and highlights its capability for nanomechanical probing of elastic properties of polymer thin films.

Section 4. discusses the complex relationship between topography and elastic properties of a conductive polymer thin film by presenting an in situ electrochemical Atomic Force Microscopy (EC-AFM) study. The effect of an applied external electrical potential on the oxidation and reduction of a polypyrrole (PPY) film submerged in an electrolyte is elucidated, and the film's topography is correlated with two-dimensional elastic modulus maps obtained from force curve measurements.

Section 5. focuses on thin BCP films, which form heterogeneous surface nanostructures. Since there is an ongoing miniaturization drive towards bottom-up nanofabrication with feature sizes below 10 nm, the ability of a double-crystalline, short-chain BCP to form vertical lamellae is explored. The lamellae formation mechanism is studied using a combined heating stage and AFM setup to examine the effect of crystallization in poly(ethylene)-*block*-poly(ethylene oxide) (PE-*b*-PEO). The use of DSA is also investigated for aligning vertical lamellae across large arrays within fabricated trench patterns.

Furthermore, Section 6. examines the solvent vapor annealing (SVA) process of PE-*b*-PEO thin films under a saturated solvent vapor atmosphere to elucidate its effect on ordering, morphology, and wetting of the thin film.

Lastly, the thesis concludes with a comprehensive summary of the key findings, thereby highlighting the importance of understanding the structure-property relationships in polymer thin films as a foundation for advancing their application in diverse technological fields.

# 2. Properties of Polymers

The word *polymer* is derived from the classical Greek words *poly* meaning 'many' and *meres* meaning 'parts'. Simply stated, a polymer is a long-chain molecule that is composed of a large number of repeating units of identical structure. While some are found in nature, many others are produced synthetically.[18] These so called macromolecules play a central role in many emerging technologies. Examples include 'plastic electronics', gene therapy, artificial prostheses, optical data storage, electric cars, and fuel cells.[1] The breadth of applications for polymers stems from the variety in structure and properties of the polymer chains. While covalent bonds are the intramolecular forces that connect the mer repeating units in the polymer chain, intermolecular forces, such as hydrogen bonds, dipole-dipole interactions, London forces, and others lead to entangled or network-like assemblies of these polymer chains in the bulk state.[1]

The following sections will introduce the basic concepts of polymer physics in order to describe ensembles of chain molecules, and illustrate the structure-property relationships of polymer thin films.[19]

## 2.1. Polymer Synthesis and Structure

### 2.1.1. Synthesis

The composition and structure of polymer chains is determined during the polymerization. Polymerization is defined as the combination reaction of *monomers*, the educt molecules, to form long-chain macromolecules. In principle, several polymerization mechanisms can be distinguished:

- Step-growth polymerization
- Chain-growth polymerization
- Controlled polymerization (or ionic polymerization)
- Other mechanisms (e.g., electropolymerization (EP))

Step-growth polymers are formed through a series of reaction steps.[1] Two monomers with each two or several reactive moieties react to form a dimer, followed by successive step-reactions until the final product forms. A typical step-growth polymerization mechanism is the condensation reaction. One example is

the peptide bond formation in amino acids to form polypeptides and proteins as shown below:

$$R_1COOH + R_2NH_2 \longrightarrow R_1{-}CO{-}NH{-}R_2 + H_2O \tag{2.1.1}$$

In contrast, chain-growth polymerization proceeds by three common steps: initiation, propagation, and termination. For example, a free-radical polymerization starts with the dissociation of the initiator (I) to form reactive radical species ($I^*$), followed by propagation, where monomer units (M) are subsequently added at the free-radical location at the reactive chain end ($P_i^*$). Termination occurs either by combination of two radicals, or by disproportionation of two radicals, effectively deleting the reactive site from the polymer chain (P). The process is schematically illustrated below:[1, 18]

$$\textit{Initiation} \qquad I \longrightarrow I^{\bullet} \tag{2.1.2}$$

$$\textit{Propagation} \qquad I^{\bullet} + M \longrightarrow IM^{\bullet} \xrightarrow{M} P_i^{\bullet} \tag{2.1.3}$$

$$\textit{Termination} \qquad P_i^{\bullet} + P_j^{\bullet} \longrightarrow P_{i+j} \tag{2.1.4}$$

In the earlier cases of industrial radical polymerization of ethylene, the highly reactive radical sites often led to broad molecular weight distributions and branching of the chains, resulting in polyethylene (PE) with low crystallinity (low density PE). However, by stabilizing the reactive free radical sites using a Ziegler-Natta type catalyst, the branching could be suppressed, resulting in the development of linear PE with high crystallinity (high density PE).

The development of controlled radical polymerization and other controlled polymerization schemes has enabled the polymerization of linear chains with narrow molecular weight distributions. These schemes are often labeled 'living' polymerization, as they can continue in a controlled manner, as long as monomer is available.[18] They enable the large-scale production of, e.g., block copolymers (BCPs) and branched polymers.[1] One example is ionic polymerization. While the polymerization steps are similar to the chain-growth polymerization (initiation, propagation, termination), the reactive species is either a carbanion or carbcation at the active site of the carbon backbone. A catalyst or initiator stabilizes and protects the active site, and monomer is inserted at the active site. The polymerization mechanism then turns the inserted monomer into the new active carbion, and the polymerization continues.

EP differs from the described chemical polymerization methods above. It provides several advantages over chemical methods, since it directly produces an electroactive, conductive film on the electrode surface and offers high yields. Additionally, the film properties (e.g., porosity, conductivity) can be controlled directly by the preparation protocol (e.g., chemical environment, electrochemical potential work function).[10, 20] Typically, the EP of a conductive polymer (e.g., polypyrrole (PPY)) proceeds by oxidation of the monomer at the work electrode (anode), followed by dimerisation/coupling of the monomer cation radicals, and subsequent chain growth. The film thickness can be exactly controlled by monitoring the transferred charge during EP. Ions from the solution are incorporated in the conductive polymer matrix during polymerization as charge compensation, leading to 'doping' of the conductive polymer.[20]

A polymerization will nearly always produce a distribution of polymer chains of varying length. For assessing the molecular weight distribution, several useful quantities can be defined:

The *number-average molecular weight* $M_N$,

$$M_N = \frac{\sum N_i M_i}{\sum N_i} \tag{2.1.5}$$

the *weight-average molecular weight* $M_W$,

$$M_W = \frac{\sum W_i M_i}{\sum W_i} = \frac{\sum N_i M_i^2}{\sum N_i M_i} \tag{2.1.6}$$

and the *index of polydispersity* PDI

$$\mathrm{PDI} = \frac{M_W}{M_N} \tag{2.1.7}$$

with the number $N_i$ of polymer molecules within the fraction of molecular weight $M_i$ and the total weight of this fraction $W_i = N_i \times M_i$. For a PDI = 1, the sample is referred to as "monodisperse", as it contains only one value of $M$. In reality, most polymerization schemes give PDIs $> 1$.[1] The length distribution of the polymer chains in the sample have an effect on the dynamics of the chains (e.g., crystallization, diffusion in the bulk, etc.), making the PDI a useful quantity for characterizing a polymer.[18]

### 2.1.2. Structure

A polymer consist of a long chain of repeating units that contains a so-called carbon backbone and functional side groups. The carbon atoms in the backbone are covalently joined together and possess tetrahedral binding angles (around 109.5°), which is why structural drawings will often depict polymer chains as zigzag pattern. The spatial arrangement of the carbon backbone and substituent side groups gives rise to different types of isomerism in polymers. The polymer *configuration* refers to the sequence of atoms in the polymer chain and is determined during polymerization. It cannot be changed without breaking chemical bonds. On the other hand, polymer *conformation* describes the geometrical arrangement of the atoms in the polymer chain. For example, through rotation, the polymer may change its conformation, allowing different placements of the substituent groups in the polymer chain.[18]

An example for polymer isomerism is illustrated in Fig. 2.1.1. It shows two polyolefin chains with each a substituent group 'R' and the hydrogen atoms. The triangles indicate the position of the atoms/substituents, with the dashed triangles pointing away from the reader and the solid triangles towards the reader. These chains have a different *configuration*. Rotating around the carbon backbone will not align the 'R' side groups in the same direction; they are so-called enantiomers. The configuration cannot be changed unless chemical bonds are broken. However, if the side groups can be aligned via rotation, they have different *conformation*.

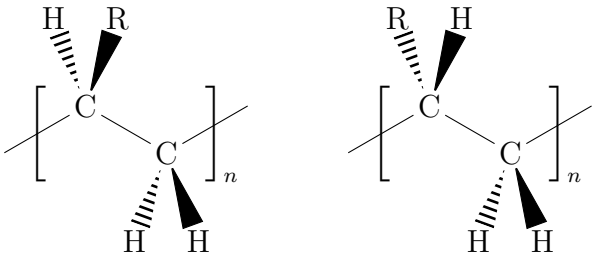


***Fig. 2.1.1.*** Illustrated are two polyolefin chains with different configuration and different conformations. Hydrogen atoms and a substituent group 'R' extend from the carbon backbone. The direction of the extension is given by the triangles (dashed: backwards, solid: outwards). The 'R' side groups cannot be matched by rotating around the carbon backbone.

The placement of functional side groups along the polymer chain gives rise to polymer tacticity. Depending on the position of the side groups as shown in

Fig. 2.1.2, different types of tacticity are distinguished. In general, tactic polymers (i.e., isotactic or syndiotactic) can be partially crystallized, while atactic polymers are amorphous. In addition to crystallinity, other polymer properties, such as thermal and mechanical behavior, can be significantly affected by the tacticity of the polymer.[18]

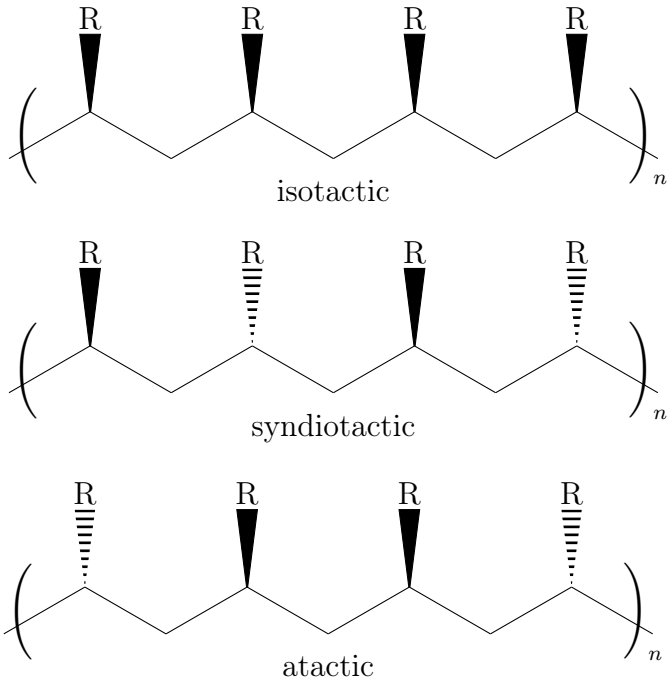


***Fig. 2.1.2.*** Examples of tacticity in polyolefins, showing isotactic (same), syndiotactic (alternating), and atactic (random) conformations based on the positions of the substituent groups 'R'. Adapted with permission from[19].

A free polymer chain can rotate around individual bonds and assume many conformations in three-dimensional space. Different models exist for describing the free polymer chain behavior, starting with, for example, the freely jointed and volumeless chain. Generally, from the chain models different chain quantities can be determined, such as the end-to-end distance vector, the Kuhn segment length, or the radius of gyration.[1, 18, 19] However, real polymer chains differ from the idealized freely jointed model. The tetrahedral C-C bond angles in the backbone, the bulky substituent groups, and the finite van der Waals volume of the chain bonds limit and hinder rotation, thus leading to unfavorable high-energy conformational states as shown in Fig. 2.1.3. The trans-conformation, where the bulky substituents in Fig. 2.1.3a are the furthest from each other, is energetically more favorable than the gauche-conformation in Fig. 2.1.3b, where the bulky sub-

stituents are closer to each other. A typical polymer with, for example, 10 000 bonds/rotational axes with three rotational conformations per bond (one trans, two gauche) would result in $3^{10000} \simeq 10^{4771}$ possible total conformations.[1] However, depending on the size of the substituents, the rotational energy barriers in Fig. 2.1.3c will shift, and some conformations will be favored over others. Describing semi-flexible polymer chains in the framework of the worm-like-chain model, the conformational space will show a length dependent change in behavior. While shorter chains will possess rigid rod-like behavior, longer chains will crossover to coil-like behavior, similar to the double helix formation of DNA, or other helix-forming polymers.[1, 19] Further details of the different chain models can be looked up in common polymer literature.[1, 18, 19]

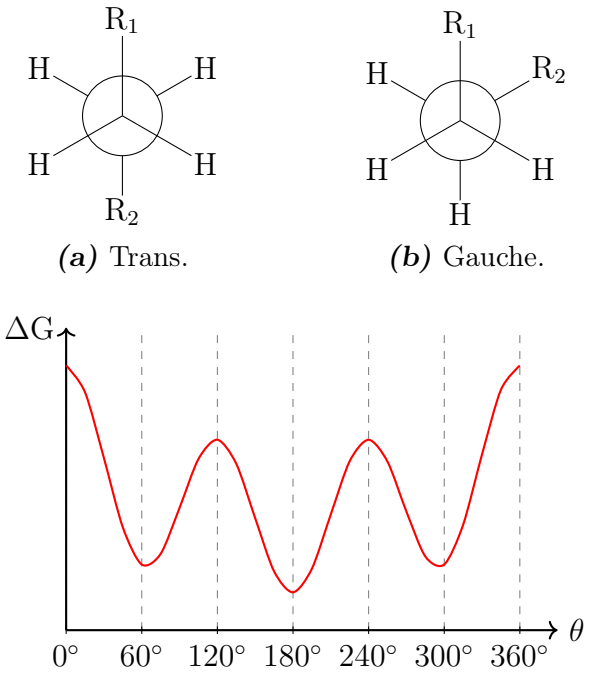


***(a)*** Trans. ***(b)*** Gauche.




***(c)*** Rotational energy.

***Fig. 2.1.3.*** Bulky substituents across the tetrahedral C-C bond give rise to a rotational energy landscape. (a) Newman projection across the C-C bond. The bulky substituents '$R_{1,2}$' are in *trans*-conformation. (b) Newman projection of the same C-C bond with the substituents in *gauche*-conformation. The bulky substituents are closer to each other in *gauche*-conformation than in *trans*-conformation, resulting in the rotational energy landscape shown in (c).

## 2.2. Polymer Crystallization

Stereoregular polymers (e.g., iso- or syndiotactic) can crystallize from an isotropic, entangled melt to form a regular, densely packed structure. Crystallization and melting are reversible phase transitions that can be described by the Gibbs equation:

$$\Delta G = \Delta H - T\Delta S \tag{2.2.1}$$

with the Gibbs free energy change $\Delta G$, the enthalpy change $\Delta H$, temperature $T$, and entropy change $\Delta S$. It proceeds by the process of nucleation and growth.[1] Ignoring kinetic effects, crystallization proceeds if the Gibbs free energy of the crystal is smaller than that of the liquid, as illustrated in Fig. 2.2.1 for an ideal crystal.

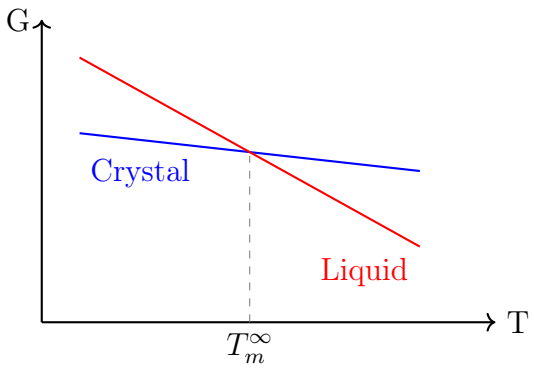


***Fig. 2.2.1.*** Temperature dependent Gibbs energies for crystal and liquid states. $T_m^\infty$ corresponds to the melting temperature of an ideal infinite crystal. Adapted with permission from[1].

The melting temperature $T_m^\infty$ of an ideal infinite crystal is defined as the intersect of crystal and liquid Gibbs free energy, when the Gibbs free energy change of melting $\Delta G_m = 0$. This yields for the equilibrium melting temperature:[19]

$$T_m^\infty = \frac{\Delta H_m}{\Delta S_m} \tag{2.2.2}$$

with the enthalpy change $\Delta H_m$ and entropy change $\Delta S_m$ of melting. Under ideal thermodynamic equilibrium conditions the crystallization temperature $T_c$, melting temperature $T_m$, and melting temperature of an infinite crystal $T_m^\infty$ are equal. However, in reality the melting temperature is always lower than the equilibrium value $T_m^\infty$. This melting point depression stems from the kinetic effect of a finite heating or cooling rate, limited crystallite size, or from the presence of

impurities.[18] This is also true for the crystallization temperature, which is even lower than the melting temperature due to the kinetics of crystallization. Heating and cooling experiments will show a hysteresis between $T_m$ and $T_c$, which is a feature of first-order phase transitions. The supercooling can be defined as:

$$\Delta T = T_m^{\infty} - T_c \tag{2.2.3}$$

and also reflects the nucleation and growth mechanism of polymer crystallization.[19] For a first-order phase transition, such as crystallization or melting, a discontinuity occurs in the first derivative of the Gibbs free energy. As illustrated in Fig. 2.2.2a, volume, enthalpy, or entropy experience a discontinuous change at constant pressure during crystallization.[18]

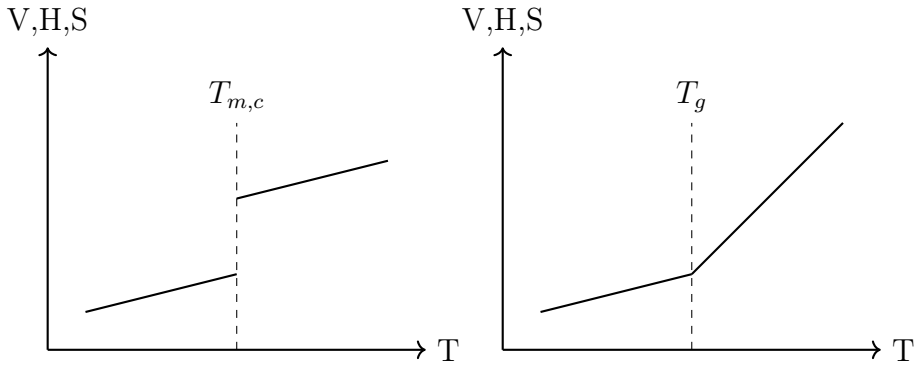


***(a)*** First order transition. ***(b)*** Second order transition.

***Fig. 2.2.2.*** First and second order transitions of volume $V$, enthalpy $H$, and entropy $S$ at constant pressure with temperature. Melting and crystallization ($T_{m,c}$) are typical thermodynamic first order transitions, while the glass transition at $T_g$ shows characteristics of a second order transition. Adapted with permission from[1].

In principle, crystallizable polymers can also form an amorphous 'glass', when sufficiently fast cooling rates impede all long-range chain relaxations. A glass state is a non-equilibrium state; the position of the glass transition temperature $T_g$ depends strongly on the cooling and heating rate due to kinetic effects, but the transition shows characteristics of a second order phase transition illustrated in Fig. 2.2.2b.

The packing of a crystalline polymer exhibits several hierarchical structures on different scales as shown in Fig. 2.2.3.[19] On the smallest scale, the periodic

packing of chains yields a crystal unit cell. A unit cell is comprised of the lattice constants $(a, b, c)$ and the angles $(\alpha, \beta, \gamma)$. Conventionally, the $c$-axis of the unit cell is defined as being oriented along the chain direction, while $a$-axis and $b$-axis are oriented along the parallel packing directions of polymer chains.[19] Seven crystal classes (cubic, trigonal, hexagonal, tetragonal, orthorhombic, monoclinic, and triclinic) are distinguished.[1] The chains, densly packed in the crystal unit cell, align themselves to form crystalline lamellae consisting of an array of chains. Due to kinetics during lamellae formation, the chains fold back into the lamellar crystal at regular intervals. These metastable, folded chain crystal lamellae illustrated in Fig. 2.2.3 are anisotropic. The lamellar surface consists of the fold surface and the lateral surface. The fold surface is comprised of chain folds, loops, and cilia (chain ends expelled from the bulk crystal), while the lateral crystal surface consists of parallel chain stems. Lamellar growth proceeds by attaching single chains to the lateral surface of the crystal. The lateral stem length is usually much smaller compared to the dimensions of the fold surface (see, e.g., Fig. 2.2.3), leading to the typical two dimensional appearance of polymer single crystals grown from dilute solutions.[19] In bulk, the lamellae grow and branch to form spherulites. The lamellae, nucleated at a single point in the center of the spherulite, grow radially outwards. Therefore, the spherulite growth direction and radius are perpendicular to the chain orientation in the lamellae.[1]

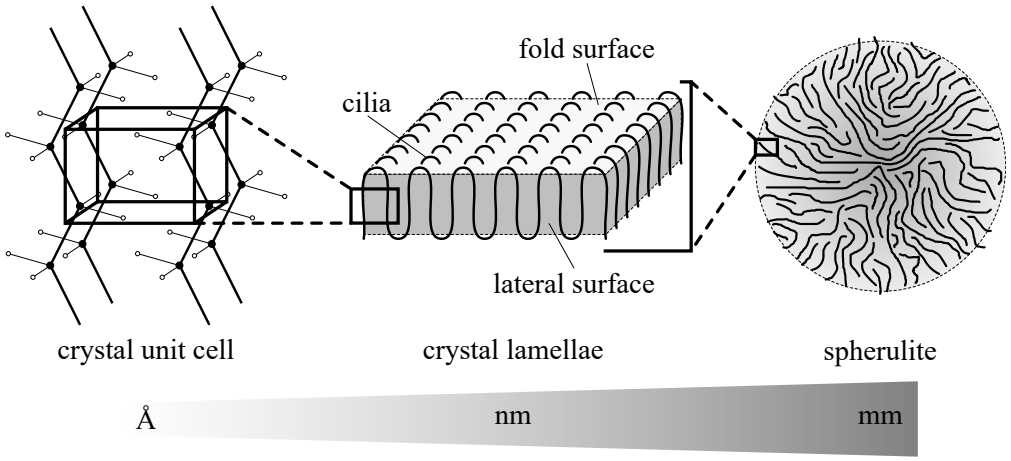


***Fig. 2.2.3.*** Illustration of the hierarchies occurring in polymer crystals. (left) A schematic crystal unit cell is comprised of several tightly packed chains. (middle) the chains fold back into the crystal at the fold surface, forming a folded chain lamellar crystal. The folded chain lamellae grow laterally. (right) In bulk, bundles of lamellae grow radially outwards, forming spherulites with dimensions $\sim$ 0.1 mm. Adapted with permission from[1].

The crystallization process can be separated into nucleation and growth. Nucleation refers to the formation of stable domains, which must be sufficiently large to become stable. The bulk energy gain of crystallization must be large enough to overcome the unfavorable free surface energy needed to create the nucleus. The formation of the nucleus can be either homogeneous or heterogeneous. Homogeneous nuclei form due to random fluctuations, while heterogeneous nuclei are usually impurities. Nucleus formation, or primary nucleation is often the rate limiting step in crystallization.[1] In classical nucleation theory, the critical radius $R^*$ shown in Fig. 2.2.4 denotes the smallest radius, at which a spherical nucleus remains stable. However, for a lamellar folded chain nucleus with lateral sizes $a, b$ and thickness $l$ as shown in Fig. 2.2.5, the Gibbs free energy is given as:

$$\Delta G(a,b,l) = abl\Delta G_V - 2al\sigma^l - 2bl\sigma^l - 2ab\sigma_e \tag{2.2.4}$$

with the lateral surface energy $\sigma^l$, fold surface energy $\sigma_e$, and the free energy change per unit volume $\Delta G_V$.[19] Since the lateral sizes are much larger than the thickness ($a, b >> l$), we obtain:

$$\Delta G(a,b) = abl\Delta G_V - 2ab\sigma_e \tag{2.2.5}$$

For nucleation, $\Delta G(a,b) = 0$ and it follows:

$$\Delta G_V = \frac{2\sigma_e}{l} \tag{2.2.6}$$

With Eq. 2.2.1 and Eq. 2.2.2 the lamellar thickness $l$ is given by the Gibbs-Thomson equation:

$$l = \frac{2\sigma_e T_m^\infty}{\Delta H(T_m^\infty - T_m)} \tag{2.2.7}$$

where $\Delta H$ is the heat of fusion per volume element, and $T_m^\infty - T_m$ the melting point depression (undercooling).[19] From Eq. 2.2.7 it is apparent that the lamellar thickness is proportional to the degree of undercooling. A small undercooling allows the chains to reorganize themselves to form thicker, more stable lamellae, whereas high undercooling leads to thinner, metastable folded-chain lamellae as a consequence of limited chain rearrangement.

The lateral growth of the lamellae consists of secondary nucleation steps. It involves the attachment of new chains at the lateral growth front of the existing nucleus, forming a single new layer. A simplified schematic is shown in Fig. 2.2.5.

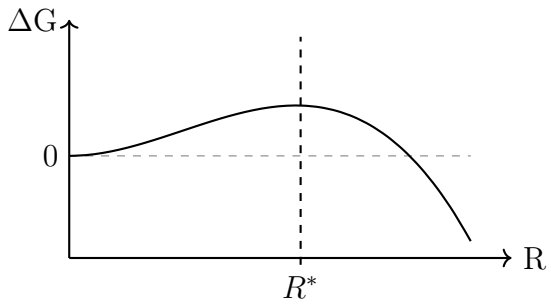


***Fig. 2.2.4.*** Gibbs free energy difference as function of the radius of a spherical nucleus. The free surface energy required to create the nucleus and the bulk crystallization enthalpy both contribute to $\Delta G$. Above the critical radius $R^*$, the nucleus is stable and can continue its growth. Adapted with permission from[1].

It is apparent that the surface area provided by the existing nucleus facilitates secondary nucleation.

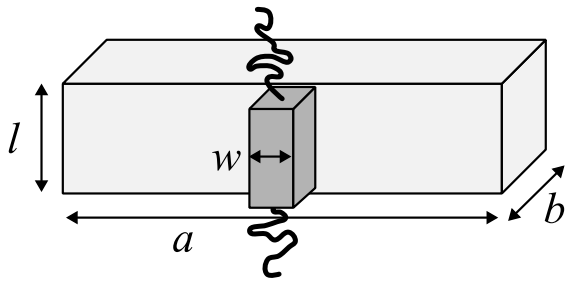


***Fig. 2.2.5.*** Simplified sketch of the attachment of a new lateral stem of thickness $w$ during secondary nucleation. The stem attaches on the lateral surface of the lamellar crystal with lamellar thickness $l$ and widths $a, b$. Adapted with permission from[1].

The attachment of the secondary nucleus (rate of secondary nucleation) and the rate of growth of a single new layer along the lateral sides $(a, b)$ in Fig. 2.2.5 both influence the crystal growth velocity and crystal shape. It is largely dependent on the undercooling, and different crystallization regimes can be distinguished. In Regime I crystallization (low undercooling) the rate of secondary nucleation is much smaller than the growth rate. Once nucleated, the layer along the lateral surface fills in completely before a new layer is nucleated. In Regime II crystallization at higher undercooling, the secondary nucleation rate and growth rate are similar, leading to nucleation on lateral growing, uncompleted layers. In Regime III crystallization at even higher undercooling, the secondary nucleation rate is much higher than the growth rate of the single layers.[1] For further reading, refer

to the Hoffmann and Lauritzen theory on polymer crystallization.[21, 22]

Under specific conditions, polymers can be crystallized as extended chain crystals. Earlier experiments (1960s) on crystalline PE achieved extended chain crystals by employing high pressure ($\sim$ 5000 atm) and low undercooling.[23] These extreme conditions are necessary since the high conformational entropy of polymer systems will nearly always favor an entangled chain conformation over the extended *all-trans* conformation. The kinetics of polymer crystallization will therefore generally favor the metastable folded chain crystal conformation at regular pressure. The growth of an extended chain crystal from a folded chain crystal proceeds by subsequent unfolding of the chains, leading to a thickening of the crystal lamellae.

This lamellar thickening process is caused by sliding diffusion of the chains in the crystal, resulting in a wedge-shaped crystal shape illustrated in Fig. 2.2.6 during the growth of extended chain crystals.[24, 25]

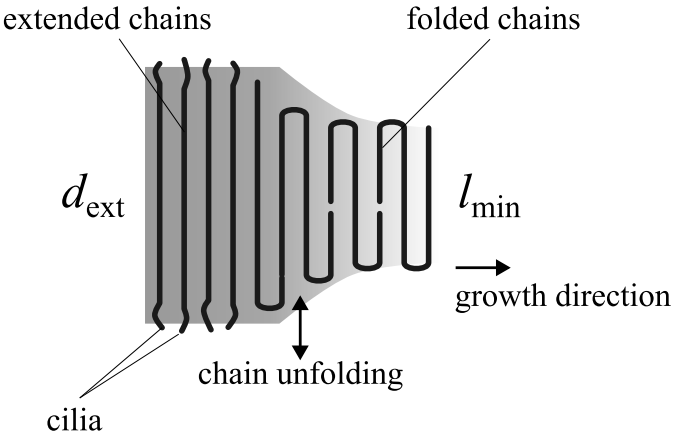


***Fig. 2.2.6.*** The lamellar thicknening process during crystallization leads to partial chain unfolding and the formation of a wedge-shaped growth front during secondary nucleation. The wedge-shaped front consists of folded chains with the minimum stable lamellar thickness $l_{min}$. Unfolding of the chains via sliding motion may lead to an extended chain conformation, where the lamellar thickness corresponds to the extended chain length $d_{ext}$. Adapted with permission from[19].

Regular long-chain macromolecules possess high conformational entropy. All possible accessible conformations of the chain depend on the rigidity of the backbone, temperature, the degree of polymerization, inter-/intramolecular forces, and more.[1] From a statistical standpoint, the conformational entropy of a polymer chain can be reduced by reducing the chain length, e.g. for oligomers. The reduced conformational entropy leads to preferred formation of extended chain crys-

tals in oligomer crystallization, instead of folded chain crystal formation. Efficient packing of oligomer chains in the crystal is easier achieved, since no chain disentanglement and unfolding is necessary.[1] In an extended chain crystal the registration of chain ends is not perfect, resulting in a transient layer of cilia on the crystal surface and a surface free energy which is different from the fold surface free energy $\sigma_e$ of a folded chain crystal.[26]

## 2.3. Conductive Polymers

Conductive polymers are a subclass of polymers which exhibit high electrical conductivity. Their common feature is polyconjugation in the $\pi$-system of their carbon backbone. They possess the electronic properties of metals, while retaining the mechanical properties and processability of conventional polymers, thus making them an attractive material for various applications.[20] The electrical and ionic conductivity of conductive polymers can be tuned by incorporation of dopants (e.g., ions) into the polymer matrix. In that regard, they behave similar to semiconductors and are often referred to as 'synthetic metals'.[20] Two examples of conductive polymers, polyacetylene and polythiophene, are given in Fig. 2.3.1, but many other conductive polymers, such as polyaniline, polypyrrole (PPY), polyphenylene, etc. exist. The charge transport along the delocalized, conjugated $\pi$-system of the double bonds or aromatic rings can proceed either through hopping or by band transport, depending on the doping level.[2]

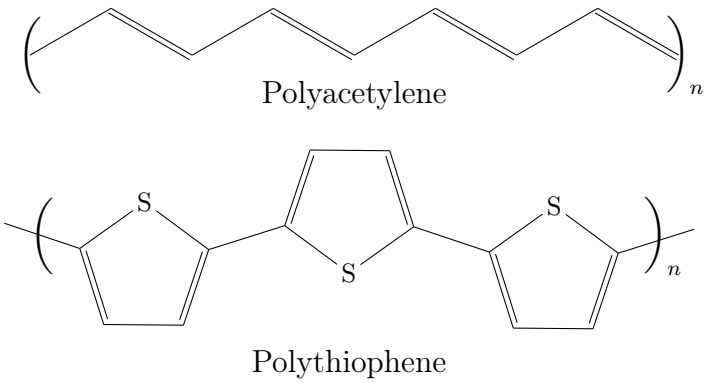


***Fig. 2.3.1.*** Examples for conjugated/$\pi$-bonded organic molecules. Several repeating units are shown for better visualization of the conjugated backbone.

The injection of electrons or holes into the polyconjugated chain leads to chain relaxation or deformation. The characteristic bond deformations can be described

by a variety of quasiparticles, e.g., solitons, polarons, and bipolarons, each with characteristic transport properties. Dopant ions are also known to partake in the charge transport in conductive polymers.[2] The conductivity increases with decreasing band gap between the highest occupied molecular orbital (HOMO) and the lowest unoccupied molecular orbital (LUMO).[18] The excitation process of an electron-hole pair in a conductive polymer, and the analogue process in a solid-state semiconductor is exemplarily shown in Fig. 2.3.2b. The HOMO of the conductive polymer corresponds to the valence band in semiconductors, while the LUMO corresponds to the conduction band. Doping of the conductive polymer or semiconductor with electron donors (e.g., anions) or acceptors (e.g., cations) shifts the Fermi level $E_f$ to either n-type or p-type conduction, respectively. The band gap and position of HOMO and LUMO can be tuned by molecular design.[27]

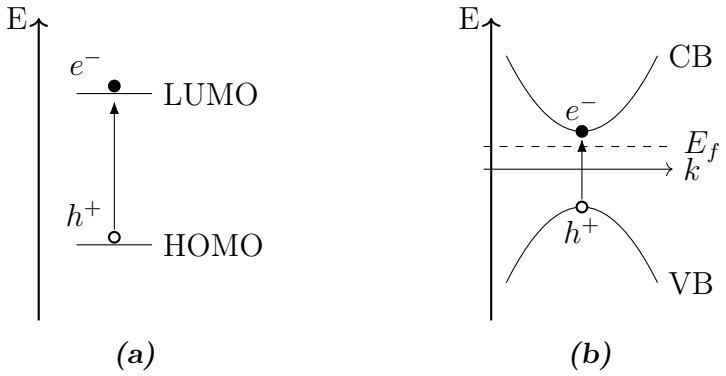


***Fig. 2.3.2.*** a) Electron excitation from the HOMO into the LUMO in a molecule. b) Electron-hole pair generation in a n-type semiconductor, where VB denotes the valence band, CB the conduction band, and $E_f$ is the fermi energy.

Thin conductive films can be easily deposited via electropolymerization (EP) as described earlier (Section 2.1.1.), making conductive polymers ideal materials for coatings and electrode materials. The electrical and mechanical properties of conductive thin films ultimately depend on the general morphology of the film set by the synthesis and processing conditions.[2] For example, electropolymerized PPY films possess properties that depend significantly on the deposition protocol.[10] Especially the electrochemical control function, such as galvanostatic (constant electrical current), potentiostatic (constant electrical potential), and potentiodynamic (cyclic electrical potential, e.g., cyclic voltammetry), determines film porosity and roughness. Investigations have shown that in aqueous environment electropoly-

merized PPY, the porosity and roughness increase when comparing potentiostatic to potentiodynamic and galvanostatic control functions.[10]

The choice of solvent during EP also influences the film morphology, since the solvent has an effect on the conjugation length of the growing chain network. PPY films synthesized in non-aqueous media, such as acetonitrile, show low roughness, porosity, and high conductivity.[20]

Additionally, the type of dopant salt effects the film properties. Dopant ions are incorporated into the PPY matrix during EP for charge balance. For example, on average one positive charge is stabilized by three PPY repeating units and counterbalanced by one anion in the oxidized state of PPY.[20] Depending on the size and charge of the ions, an excess of either cations or anions is deposited in the film. In electrolyte solution, electrochemical potential cycling switches the film between reduced and oxidized state, leading to ion and solvent transport into and out of the polymer matrix. The ion transport can be mixed with cations and anions, or dominated by a single type of ion.[4] A schematic example of anion dominated transport is shown in Figure 2.3.3 for PPY. Changing the PPY from oxidized to reduced state by applying an external current will expel anions from the polymer matrix for charge balance.

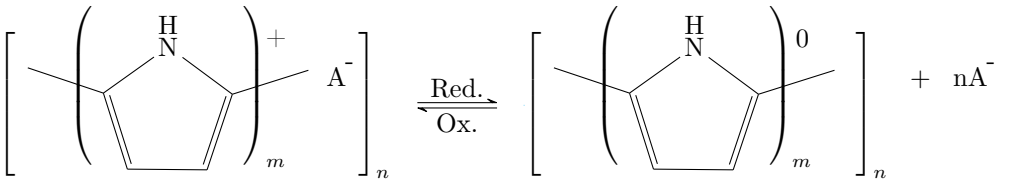


***Fig. 2.3.3.*** Schematic redox reaction of PPY. In the oxidized state, three PPY repeating units ($m = 3$) share one positive charge, which is counterbalanced by an anion incorporated in the polymer matrix. Reducing the PPY to its neutral state will expel the anion out of the polymer matrix for charge neutrality.

The insertion and expulsion of ions is associated with a volume change of the conductive film.[4] The volume change is in part caused by changes of the polymer backbone upon oxidation/reduction, but a large part stems from ion and solvent transport. Figure 2.3.4 illustrates how flux of solvated ions leads to reversible swelling and shrinking of a PPY film depending on the oxidation state. Additionally, osmotic pressure causes an additional influx of solvent molecules apart from the oxidation-state dependent charge transport.[28] Long term relaxations and rearrangement of the polymer network may effect the film thickness over longer timescales.[29, 30]

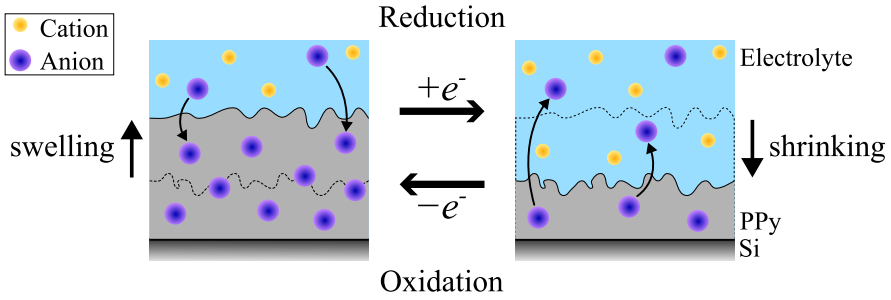


***Fig. 2.3.4.*** The PPY redox reaction causes a corresponding swelling or shrinking of the film due to solvent and ion diffusion. The illustrated case shows anion dominated transport. Not shown is how solvent moves together with the anions into/out of the PPY matrix.

In addition to volume changes, the mechanical properties such as the elastic modulus change upon oxidation and reduction. The exact behavior depends on the type of ion transport and internal film morphology.[31–33] Actuators and artificial muscles have been designed based on the volume changes during oxidation/reduction. Their unique properties make conductive polymers attractive materials in the fields of energy storage (e.g., supercapacitors), biomedical applications (e.g., drug delivery, artificial muscles), sensors, electrode materials, organic electronics, and more.[4, 29]

## 2.4. Block Copolymers

Copolymers are a subclass of polymers consisting of different chemically distinct repeating units, which are covalently joined together. An overview is given in Fig. 2.4.1. This sections' focus lies on linear diblock copolymers, which consist of two linear covalently connected copolymer blocks spanning across the polymer backbone.

Chemical or other incompatibilities of block A and block B often result in phase separation of both blocks. However, diblock copolymers can form only molecular-scale small domains of microphases rather than experience macroscopic phase separation, because of the constraint of the covalent bond between the two components. Based on compositions (volume fractions), the major component forms the continuous matrix, while the minor component forms the microphase domains. The most common equilibrium geometric shapes of microdomains in bulk can be lamellae, gyroids, cylinders and spheres, as illustrated in Fig. 2.4.2, which pack orderly into a nanoscale periodic pattern and can be used as nanoscale templates for the fabrication of functional nanomaterials.[19] As illustrated in Fig. 2.4.2, the

—A–A–A–A–A–A—
homopolymer

—A–B–A–B–A–B—
alternating copolymer

—A–B–B–A–B–A—
random copolymer

—AAAA–BBBB–AAAA–BBBB—
(linear) block copolymer (BCP)

***Fig. 2.4.1.*** The different classes of copolymers can be distinguished by their chain architecture and arrangement of repeating units (A,B), or blocks. Linear diblock copolymers consist of regular sequences of blocks, which are set during polymerization.

block length ratio $f_i$ determines the microphase-separated morphology, while the segregation strength of the block copolymer (BCP) is given by the product of the Flory-Huggins interaction parameter and chain length ($\chi \times N$). The transition from a homogeneous melt to a micro-phase structure is termed the order-disorder-transition and occurs at a critical value of $\chi_{\mathrm{ODT}} \times N$. The temperature, at which the transition occurs, is termed the order-disorder-transition temperature $T_{\mathrm{ODT}}$. For a symmetrical BCP (where volume fractions $f_A = f_B = 0.5$) the critical value for $\chi \times N = 10.5$.[18] For values beneath 10.5, the BCP system is miscible. For values above 10.5, weakly segregated and strongly segregated regimes are distinguished.

Energetically, microphase separation is controlled by a competition between the tendency to minimize the interfacial energy between immiscible polymers and the maximization of mixing entropy between chains of block A and block B that decreases upon phase segregation.[18] Flory and Huggins developed a theory based on a simple lattice model to describe the mixing of polymers in solutions. As illustrated in Fig. 2.4.3, the lattice sites in the model are the size of the solvent molecule, and the polymer chain is segmented, so that each segment occupies a single lattice site.[18] The theory is also used to describe the mixing of two different polymers, as for example, in a BCP.

For the simple case of a blend of two solvents, the general expression for the Gibbs free energy $\Delta G_{mix}$ is given by the mixing enthalpy $\Delta H_{mix}$ and mixing entropy $\Delta S_{mix}$:

$$\Delta G_{mix} = \Delta H_{mix} - T\Delta S_{mix} \tag{2.4.1}$$

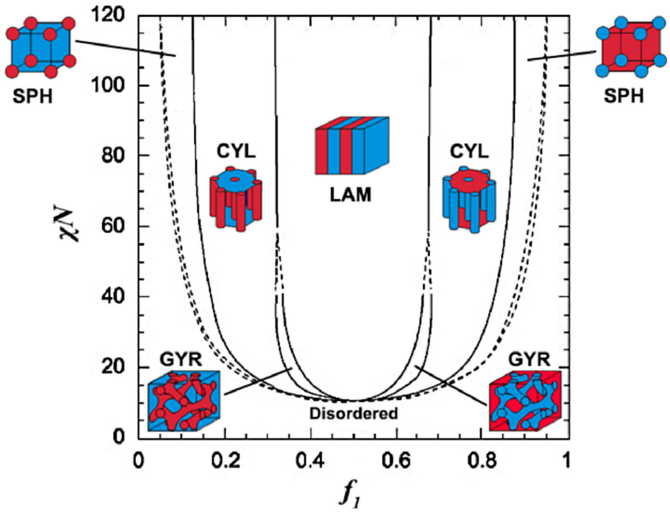


***Fig. 2.4.2.*** Phase diagram of a diblock copolymer. Depending on the volume fraction $f_A$ of block A, the BCP adapts various microstructures, from a spherical cubic morphology, to cylinders, gyroid, lamellar, and the corresponding inverted microphases. The y-axis is given by the segregation strength $\chi N$ and is inverse proportional to temperature. Adapted with permission from[34, 35].

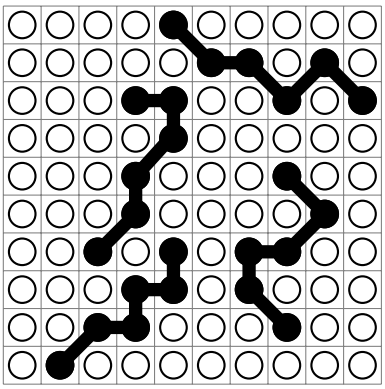

***Fig. 2.4.3.*** Flory-Huggins lattice model for the mixing of solvents and polymers. The size of a solvent molecule corresponds to a single lattice site. Each polymer chain is separated into $r_i$ segments of size $n_i$, where each polymer segment occupies a single lattice cite.

From the Flory-Huggins lattice model, the entropy of mixing can be derived as:[18]

$$\Delta S_{mix} = -k(n_1 \ln(\phi_1) + n_2 \ln(\phi_2)) \tag{2.4.2}$$

with the number of molecules $n_{1,2}$ and the lattice volume fractions $\phi_{1,2}$ of the solvents. The mixing enthalpy of a regular solution ($\Delta H_{mix} \neq 0$) is given by:[18]

$$\Delta H_{mix} = z n_1 r_1 \phi_2 \Delta\omega_{12} \tag{2.4.3}$$

where $z$ is the lattice coordination number or number of cells that are first neighbors to a given cell, $r_1$ represents the number of 'segments' in a solvent molecule for consideration of the most general case, and $\Delta\omega_{12}$ is the change in internal energy for formation of an unlike molecular pair. From $z$ and $\Delta\omega_{12}$, a single dimensionless energy parameter, the Flory-Huggins interaction parameter $\chi$, can be defined:[18]

$$\chi = \frac{z r_1 \Delta\omega_{12}}{kT} \tag{2.4.4}$$

It characterizes the interaction energy per solvent molecule (having $r_1$ segments). Additionally, it has an inverse relation to temperature and is concentration-independent.[18] With this, the mixing enthalpy becomes:

$$\Delta H_{mix} = kT\chi n_1 \phi_2 \tag{2.4.5}$$

Combining mixing entropy and enthalpy gives the Flory-Huggins expression for the Gibbs free energy of mixing of two solvents:[18]

$$\Delta G_{mix} = kT(n_1 \ln\phi_1 + n_2 \ln\phi_2 + \chi n_1 \phi_2) \tag{2.4.6}$$

For a blend of two polymers, the general expression for the two solvent blend in Eq. 2.4.6 needs to be adapted. In the lattice model, the polymer chains are divided into a number of segments $n_i$ with regular size $r_i$. For a two polymer blend, the occupation by one polymer in the lattice is given by:

$$N_{1,2} = r_{1,2} n_{1,2} \tag{2.4.7}$$

While the total occupation/total number of lattice sites is given as:

$$N = N_1 + N_2 \tag{2.4.8}$$

And the volume fraction $\phi_i$ of each polymer in the lattice is given by:

$$\phi_{1,2} = \frac{N_{1,2}}{N} \tag{2.4.9}$$

Therefore, for a binary blend of two polymers with chain lengths $r_i$ (corresponds to the polymerization degree for polymers) and the volume fractions $\phi_i$, the Gibbs free energy of mixing is:[19]

$$\Delta G_{mix} = NkT(\frac{\phi_1}{r_1}\ln\phi_1 + \frac{\phi_2}{r_2}\ln\phi_2 + \chi\phi_1\phi_2) \tag{2.4.10}$$

The two first terms contribute to the entropy of the system. If $r_i$ is large, e.g., for very large polymer chains, the common mixing driving force (mixing entropy) will be small. Therefore, regular long-chain polymers are difficult to mix.[19] However, solubility can be improved either by temperature or by improving compatibility by chemical modification of polymer side groups, which effectively reduces $\chi$. Note that the Flory-Huggins theory is limited by the simple lattice model, which neglects volume changes upon mixing, yields a concentration and composition independent $\chi$ parameter, and does not consider energetically preferred arrangements of polymer segments in the lattice.[18] Despite these limitations, the Flory-Huggins theory is still widely used and offers a compact thermodynamic formalism for the mixing of polymers.

The technological drive to develop 'soft' nanotemplates based on microphase-separated BCPs for nanofabrication has stimulated research into BCPs with sub-10 nm features. Since the sizes of the microstructures that emerge from the self-assembly process are largely governed by the volume fraction of each block and the overall degree of polymerization $N$ of the BCP, a reduction of $N$ to achieve sub-10 nm features simultaneously requires sufficient incompatibility between the copolymer blocks for self-assembly.[13] Therefore, the development of sub-10 nm nanopatterning techniques based on strongly segregating, short-chain BCPs, called 'high $\chi$ low $N$' BCP, offers the potential for future applications beyond current photolithographic limits.[13]

### 2.4.1. Block Copolymer Thin Films

Molecular self-assembly is a promising approach for the preparation of structured nanotemplates. For future applications in photolithography, BCP based nanotemplates have to be studied as thin films. In bulk, the BCP morphologies are

goverened mostly by the Flory-Huggins interaction parameter $\chi$ and the block lengths, or volume fractions of the copolymer blocks. In contrast, BCP thin films are confined in two dimensions. They are often characterized by oriented domains. The orientation is a direct result of surface and interfacial energy minimization.[6]

Upon annealing, which is usually applied to induce BCP microphase separation, the polymer films become structured and oriented. A minimization of internal energy is achieved by redistribution and reorientation of polymer chains.[14] Confined to the thin film, the BCP chains experience unfavorable internal stretching/compression forces and self-assemble into morphologies that relieve the stress or mitigate the entropic penalty with favorable enthalpic interactions at the substrate or free surface.[36] The affinity of the substrate with each copolymer block determines the wetting of the substrate, while the copolymer block with lower surface energy is exposed to the free surface. Both substrate and free interface thus control the orientation of the domains. The domains arrange into parallel or perpendicular morphologies, as illustrated in Fig. 2.4.4a.[14] Depending on the intrinsic structure periodicity, i.e. the equilibrium polymer domain spacing of the BCP, and the film thickness, different thickness dependent morphologies can form, see, e.g., Fig. 2.4.4b to 2.4.4e.[14] Some examples include surface-parallel lamellae/cylinders, half-lamellae, surface-perpendicular lamellae/cylinders, and mixed hybrid structures.[6] Of these morphologies, only perpendicular orientations of cylinders, gyroids, or lamellae, forming heterogeneous surface nanostructures, allow for their use as shadow masks during lithography processing.[14]

Perpendicular morphologies are known to form under 'neutral' wetting conditions, when both copolymer blocks possess similar wetting affinity to the substrate interface.[6, 14, 36–38] The affinity of two materials can be evaluated by comparing their surface free energies or surface tensions. However, for accurate determination of wetting affinity, the interfacial energies of the copolymer blocks with the substrate need to be determined. Using a modified Young's equation by Owens, Wendt, Rabel and Kälble (OWRK), the interfacial energy $\gamma_{A-s}$ between substrate and copolymer block can be calculated by[39]:

$$\gamma_{A-s} = \gamma_A + \gamma_s - 2\sqrt{\gamma_A^d \gamma_s^d} - 2\sqrt{\gamma_A^p \gamma_s^p} \tag{2.4.11}$$

With the disperse ($\gamma^d$) and polar ($\gamma^p$) contributions to the surface energy of substrate $s$ ($\gamma_s$) and copolymer block $A$ ($\gamma_A$).[14] In comparison, the interface at the free surface is often covered by the block with the lower surface energy.

Modification of the substrate surface with random copolymers or self-assembled

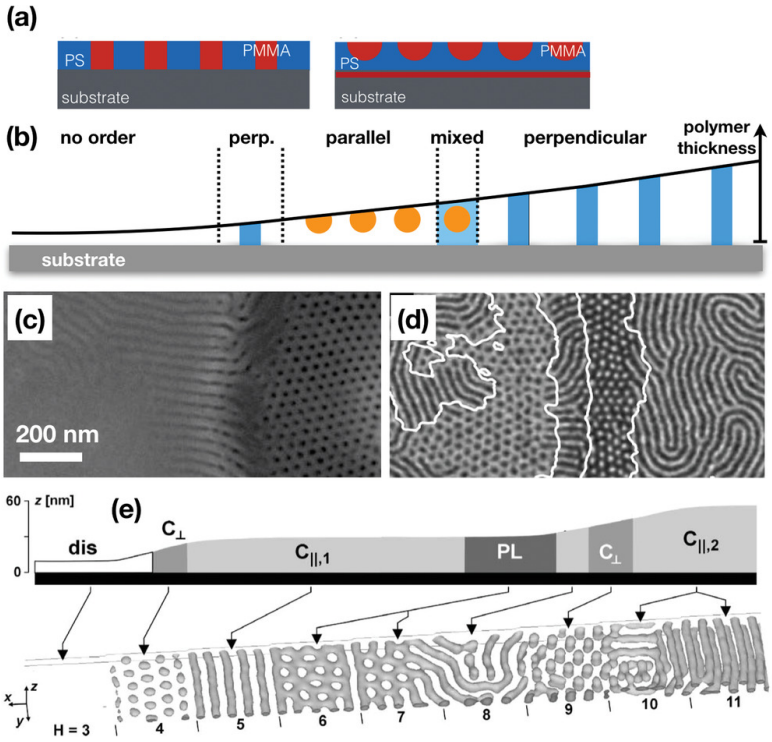


***Fig. 2.4.4.*** a) Sketch showing perpendicular (left) or parallel (right) orientation of PMMA cylinders in a PS matrix. b) Sketch presenting the changing polymer cylinder orientation (blue if perpendicular, orange if parallel) with increasing polymer film thickness. c) SEM image of microphase-separated PS-b-PMMA exhibiting an increasing film thickness from left to right. d) TM-SFM image of a microphase-separated SBS triblock copolymer with increasing film thickness from left to right. e) Sketch presenting the different polymer domain orientations with increasing film thickness. C and PL are cylinders and perforated lamella, respectively. Reproduced with permission from[14].

monolayers are two common approaches to modify the wetting affinity. The random copolymer method relies on the statistical composition of the copolymer to tune the substrate surface energy and surface chemistry. The random copolymers form a brush layer covering the substrate. Self-assembled monolayer methods for BCP studies usually involve chlorosilane chemistry on silicon oxide surfaces, or thiol chemistry on gold surfaces, where the thiol containing surfactant exhibits a specific functional moiety at the opposite end of the thiol group to tune the surface energy of the substrate.[36] Therefore, control of the interfacial energy between polymer species and substrate enables orientation control.[14] Beside equilibrium arguments, however, it is necessary to consider the pathway of the formation of ordered microphases to gain deeper insights into the nature of the ordering phenomena of copolymers at near neutral surfaces.[37]

### 2.4.2. Crystallization in Block Copolymers

Crystallization offers an additional mechanism for controlling the final morphology of BCPs.[40] BCP crystallization itself may couple or compete with the microphase separation. The competition determines the final structures and morphologies of polymer assemblies, opening up pathways for the crystallization-driven hierarchical ordering of BCPs.[41] Since crystallization is described as a phase separation process, the ordering from the crystallizing melt may expel impurities, e.g. the opposite copolymer block, therefore providing a driving force for microphase separation which may be stronger than $\chi$. For example, weakly segregated, crystallizable BCP systems have been shown to exhibit strongly phase segregated morphologies after crystallization.[42] BCP crystallization may yet serve as a way to increase the effective $\chi$, offering great potential for the development of high $\chi$, low $N$ BCPs.

In diblock copolymers, one or both blocks can be crystallizable. They are classified into single- and double-crystalline BCPs.[41] When both blocks are crystallizable, they crystallize cooperatively or independently when cooled from a microphase separated melt.[43] The possible crystallization pathways are shown in Fig. 2.4.5. The pathways depend on the relative positions of the crystallization temperatures ($T_{c1,c2}$) of both blocks with respect to each other and the order-disorder-transition temperature $T_{\mathrm{ODT}}$. The relative sequence of crystallization is important, as in, e.g., sequential crystallization the crystallization of the first block is influenced by the composition (and microphase separated morphology), while the second block is further restricted by the immobility of the first block in its crystal and possible confinement due to the lamellar spacing of the first block. In

contrast, it also has been observed that the crystallization of the first block may act as a nucleating agent (stretching or stiffening of chains of the second block) for the second crystallization. The effects are more complicated when coincident crystallization ($T_{c1} \approx T_{c2}$) dominates.[44]

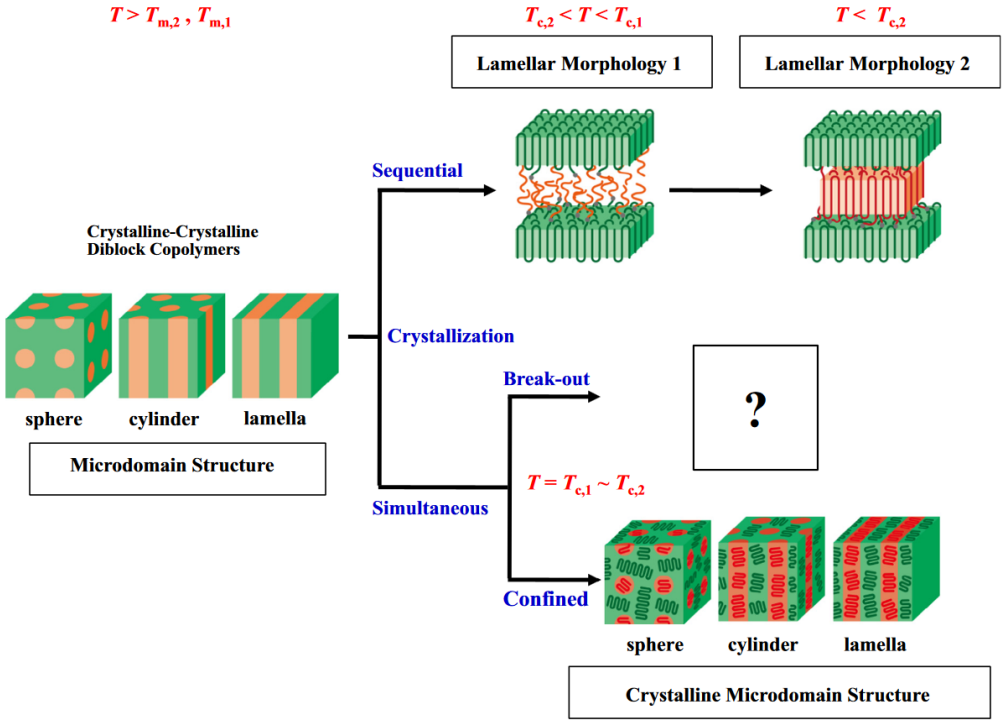


***Fig. 2.4.5.*** Possible crystallization mechanism of microphase-separated crystalline–crystalline diblock copolymers. When the crystallizable temperatures of two blocks $T_{c,1}$ and $T_{c,2}$ are widely separated, sequential crystallization occurs to form a crystalline lamellar morphology (upper route), whereas when they are close enough, simultaneous crystallization might be observed to form characteristic morphologies in the system (lower route). With permission from[43].

In the case of coincident crystallization, the segregation and confinement strength of the microphase separated morphology determines whether the crystallization proceeds confined to the domains of the respective blocks, or if breakout crystallization occurs. Breakout crystallization primarily occurs in weakly segregated BCPs and refers to the overwriting of the existing microphase separated morphology by the forming crystalline lamellae. Independent of the volume fractions of the blocks, breakout crystallization may destroy the microphase separated morphology and lead to the formation of a lamellar morphology.[41, 45] The effects, which confinement has on BCP crystallization, can be separated in space confinement, caused by the domain size of the microphase separated morphology, and

chain confinement. Space confinement corresponds to a change in nucleation mechanism caused by confining the crystallization to the respective microdomains. In selected cases, fractionated crystallization has been reported, indicating different types of heterogeneous nuclei, or suppressed crystallization, due to a homogeneous nucleation mechanism.[42] For chain confinement, the chain ends of the copolymer blocks are fixed at the nanodomain interface, which restricts the chain mobility and changes the crystallization dynamics compared to, e.g., homopolymer crystallization in nanodomains.[42, 43] The confinement can lead to a depression of the crystallization and melting temperatures compared to the values of the corresponding homopolymer.[17] However, simulations have also shown that the local chain ordering close to the microphase interface (chain prestretching) may facilitate primary nucleation instead, causing the emergence of perpendicular or parallel crystallites.[46]

The confinement also has an effect on the orientation of the chains in the crystal lamellae. In double-crystalline lamellar microdomains formed by two different blocks both blocks share the same interface, which requires that both domains take up the same surface area. When the chain packing, i.e., crystal lattice, of the two blocks mismatch, the crystalline stems may tilt or eventually become parallel to the lamellar interface to match the preferred interfacial area of both crystalline blocks, keeping the interfacial curvature constant at zero.[17, 45] This is seen, e.g., in double-crystalline, short-chain poly(ethylene)-*block*-poly(ethylene oxide) (PE-*b*-PEO), where the polyethylene (PE) chains adapt a 22° tilt with respect to the lamellar normal.[47]

Confined crystallization of BCPs in thin films has additional implications for the orientation of the chains in the lamellar crystals. The free surface allows for changes in volume by dewetting and crystal thickening.[44] Generally, there are two predominant lamellar orientations for thin films of crystalline homopolymers (i.e., flat-on and edge-on). As shown in Fig. 2.4.6a, in flat-on orientation the c-axis of the chains in the lamellae is normal to the substrate, while in edge-on orientation the c-axis of the chains in the lamellae is parallel to the substrate.[48] The interactions between the homopolymer chains and the substrate severely influence the chain mobility and conformation, leading to film thickness-dependent kinetics for the primary nucleation.[49] The formation of oriented nuclei at interfaces and the nucleation rate ultimately determine the final crystalline morphology in a homopolymer thin film. For strongly interacting homopolymer-substrate systems, flat-on lamellar crystals form, whereas repulsive or neutral interaction of the chain

with a substrate will lead to edge-on formation.[49, 50]

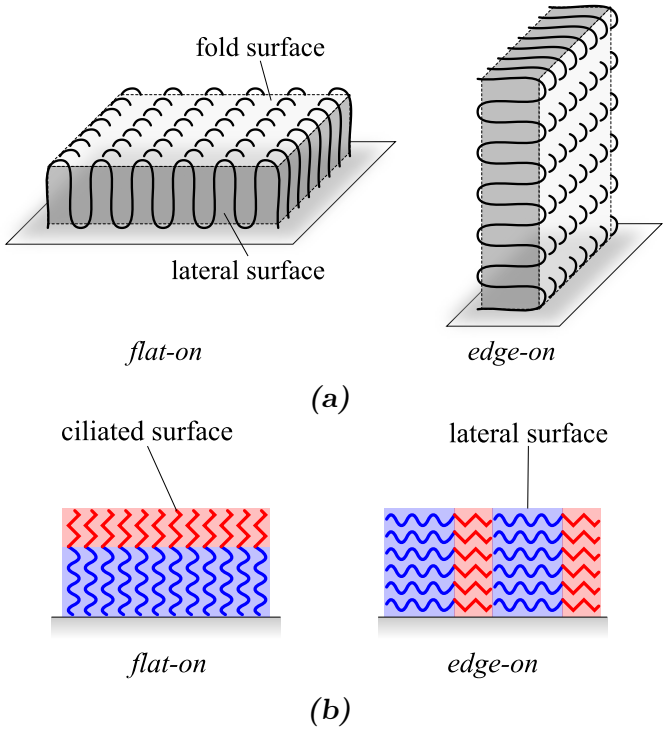


***Fig. 2.4.6.*** a) Possible orientations of lamellar homopolymer crystals on a substrate. In flat-on geometry, the lamellar fold surface contacts the substrate, while in edge-on geometry the lateral crystal surface is exposed to the substrate. b) Possible orientations of a double-crystalline, extended chain diblock copolymer on a substrate. The orientations are analogous to the homopolymer, i.e., flat-on and edge-on.

Similar to oriented homopolymer crystallization, BCPs can also crystallize in flat-on or edge-on orientation, as illustrated in Fig. 2.4.6b. Vertical (edge-on) crystalline lamellae of BCPs have been reported to form under specific crystallization conditions. For example, a polybutadiene-block-polyethylene oxide thin film initially formed a horizontal lamellar morphology in the amorphous state.[40] Kinetic control of polyethylene oxide (PEO) crystallization led to the formation of vertical lamellae (edge-on) at high undercooling. The PEO adapted a folded chain conformation; annealing below $T_{m,PEO}$ resulted in a lamellar thickening process and unfolding of the PEO chains, leading to a change to a horizontal (flat-on) morphology. Other reports showed how vertical lamellae of poly(L-lactic acid)-block-polystyrene could only form when the crystallization temperature of the poly(L-lactic acid) was above the glass transition temperature of the polystyrene block, i.e., the mobility of the chains allowed for reorganization. If the poly(L-lactic

acid) was crystallized below the glass transition temperature of the polystyrene, the poly(L-lactic acid) block crystallized confined by the polystyrene blocks in a horizontal lamellar morphology.[51]

These reports demonstrate how the orientational control of BCPs can be achieved through crystallization. However, in light of the development of high $\chi$, low $N$ materials for nanofabrication, further research is needed to elucidate how short-chain crystallizable block co-oligomers can be utilized for vertical nanopattern formation in the sub-10 nm regime.

# 3. Atomic Force Microscopy

## 3.1. Fundamentals of Atomic Force Microscopy

Atomic Force Microscopy (AFM) is a scanning probe technique that measures the force between a probe and a sample surface.[52] A sharp tip attached to the end of a force-sensing cantilever probe is scanned over the surface, measuring the spatial variations of the interactions between the tip and the surface. It provides a nanometer-scale, two-dimensional mapping of various surface properties, e.g., mechanical, electrical, magnetic, and topographical. The operation conditions of AFM are flexible, accommodating environments from vacuum to air, liquid media, and at reduced or elevated temperatures.[9]

Alongside AFM, many nanoscale imaging techniques have been employed to understand the structure and function of polymer materials, such as electron microscopy (SEM and TEM) and X-ray scattering (SAXS and GISAXS) methods.[52] However, electron microscopy is limited to measurements in a vacuum, requires additional preparation of the samples to enhance contrast, and often leads to irreversible electron-beam induced damage. While grazing incidence X-ray methods (GISAXS/GIWAXS) allow thin film samples to be investigated under *in situ* conditions, they typically require synchrotron radiation. Their reciprocal space information is an average over the entire cross-section of the beam on the thin film area, revealing structural information on the mesoscale. Of these techniques, AFM stands out for its unrivaled capability to study a wide variety of structural and dynamic features nondestructively in real space and time, and under a variety of application-relevant conditions.[52]

The wide variety of AFM imaging modes makes it an attractive tool for polymer characterization.[52] The general work principle, including the cantilever probe, piezoelectric actuators, and feedback system (consisting of a laser and photodiode setup), is depicted in Fig. 3.1.1. In the simplest imaging scheme, the tip stays in contact with the sample (contact mode) while scanning over the sample surface. The scanning is performed by applying a voltage to the x and y piezoelectric actuators. One differentiates between the fast scan axis, where the tip is scanned forwards (trace) and backwards (retrace) along a line, and the slow scan axis, which is the line by line movement. Changes in topography result in a changed tip deflection, which is detected by the laser-photodiode-feedback system. The feedback loop then attempts to keep a set constant cantilever deflection by moving the cantilever via the z piezoelectric actuator.[52] This way, a three-dimensional

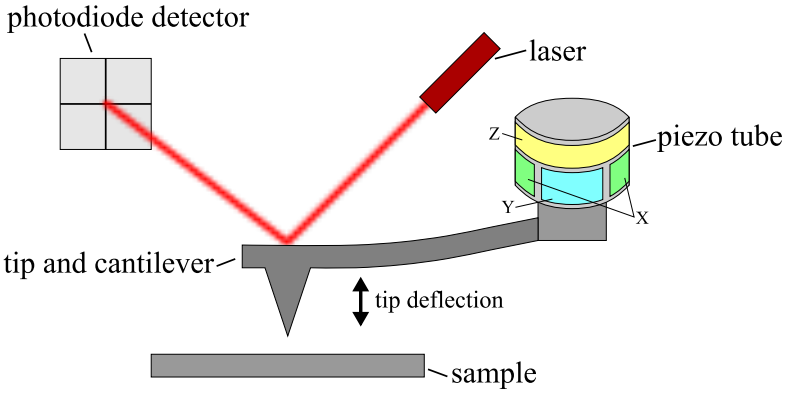


***Fig. 3.1.1.*** Scheme of an AFM. The tip attached to the cantilever is scanned over the sample surface. The scanning movement in X, Y, and Z direction is performed with a piezo tube. The tip deflection caused by tip-sample interactions is detected by measuring the position of a laser (reflected from the backside of the cantilever) on a photodiode detector. The photodiode signal is used for the feedback loop of the system.

topographic image of the sample surface is constructed.

In other imaging modes the cantilever is oscillated near its fundamental resonant frequency, and the amplitude, the resonance frequency, and the phase shift of the oscillation link the dynamics of a vibrating tip to the tip-surface interactions. Any of them could be used as a feedback parameter to track the topography of a surface.[52] The application of an oscillating voltage to the piezoelectric actuator produces its vibration and in turn produces the oscillation of the microcantilever. In the absence of external fields, the dominant forces acting on the tip are van der Waals interactions, short-range repulsive interactions, adhesion and capillary forces.[53]

In frequency modulation AFM (FM-AFM, also known as non-contact AFM) the cantilever is kept oscillating above the sample surface with a set constant amplitude at its current resonance frequency, which shifts due to tip-sample interaction. The feedback system records the change in resonance frequency, amplifies the signal, modifies the amplitude of the new excitation signal to force the system to oscillate at the set amplitude, and shifts the phase of the signal to match the new resonance conditions. This feedback loop keeps the cantilever always vibrating at its current resonance frequency with the same constant amplitude, set at the beginning of the experiment.[53] During the scan, the tip-sample distance is varied in order to achieve a set value for the frequency shift. Thus, the topography in the images represents a map of constant frequency shift over the surface.[53]

In amplitude modulation AFM (AM-AFM, also known as tapping mode AFM) the cantilever is excited at a set fixed frequency, usually near or at the free resonance frequency. The oscillation amplitude is used as a feedback parameter to image the sample topography, while the tip periodically contacts ('taps') the sample surface. In tapping mode the force gradient varies considerably during an oscillation due to the steadily changing tip-sample separation. This introduces non-linear features in the dynamics of the tip motion. Furthermore, dissipative processes such as surface adhesion hysteresis, viscoelasticity or electronic dissipation may also be involved in the tip-surface interaction.[53] When tip-sample separation is decreased, the resonance frequency of the cantilever changes, which also changes the amplitude of the oscillation. Attractive tip-sample forces will shift the resonance frequency to lower values, while repulsive forces will lead to an increased resonance frequency. The feedback system will keep the cantilever vibrating at a set fixed frequency. Caused by the tip-sample separation, the shift between the set frequency and the new resonance frequency changes the amplitude of the oscillation, which is then used to track the sample topography.[53]

In an additional operating mode of AM-AFM, compositional contrast in heterogeneous samples can be obtained by recording the phase lag of the tip relative to the excitation signal, while the feedback system keeps the amplitude at a fixed value. This is referred to as phase imaging. Phase imaging allows to detect variations in material properties such as adhesion, elasticity, and viscoelasticity. It can be used to map compositional or structural variations of the inelastic and elastic properties of samples.[52, 53]

## 3.2. Resolution and Image Artifacts

One source of image artifacts is noise. The noise is originated by the presence of mechanical, electronic, thermal or feedback perturbations. Those perturbations, in particular feedback perturbations, are always present in AFM. Feedback or intrinsic perturbations arise due to the finite time response of the feedback electronics, usually in the $10^{-4}$ s range. In AM-AFM, attractive and repulsive tip-surface interactions and their non-linear character gives rise to the coexistence of stable oscillation states as solutions for the equation of motion of a cantilever-tip-sample ensemble. Proper AFM operation is possible, if the intermediate and initial (unperturbed) oscillation states are similar, otherwise instabilities and image artefacts should appear, as shown in Fig. 3.2.1a.[53]

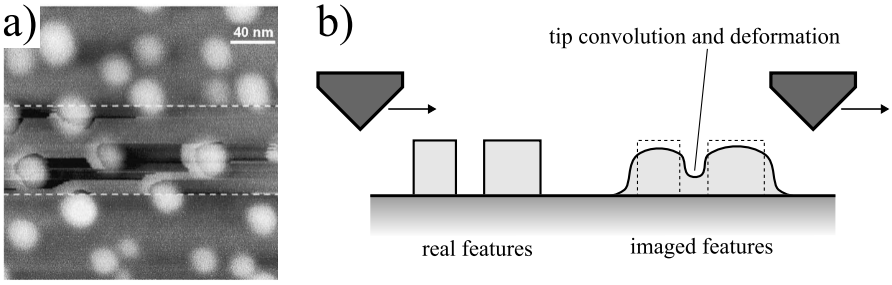


***Fig. 3.2.1.*** a) Effect of switching oscillation states on the AFM height image of an InAs quantum dot sample ($200 \times 200$ nm$^2$). Switching of the oscillation states leads to instabilities and artifacts appear in the image. Adapted with permission from[53] b) Effects the finite tip size has on the lateral resolution in AFM operation. The size of the real features is distorted (broadening) by tip geometry. Under high tapping force, softer samples might additionally show deformation.

An AFM generates three-dimensional images of the sample surface. As a consequence, two different resolutions should be distinguished, lateral and vertical. Vertical resolution is limited by both noise from the detection system and thermal fluctuations of the cantilever. Generally, the thermal noise of the cantilever is the largest source of noise, since damping systems have become so effective that mechanical vibrations represent a negligible perturbation of the cantilever oscillation. For a cantilever with a force constant of 40 N/m, the thermal fluctuations of the cantilever are below 0.01 nm at 295 K.[53] Lateral resolution in tapping mode depends on tip size, tip-surface separation, tip-surface force and the compliance of the sample. As illustrated in Fig. 3.2.1b, the finite tip size is responsible for the broadening effects observed in most AFM images. A damaged tip (e.g., a double tip) will lead to image artifacts in the image. Therefore, the measurements tend to overestimate lateral dimensions of three dimensional objects.[53]

## 3.3. Probing of Mechanical Properties

Polymer materials often exhibit heterogeneities in material characteristics and chemical composition. Especially thin polymer films have striking dynamic properties that differ from their bulk counterparts and, therefore, have practical implications for thin film coatings, lubrication, adhesion, and friction. Advances in AFM make it ideal for studying structural defects and dynamics of highly complex heterogeneous polymer structures.[9] In addition to imaging topography, the AFM tip can be used to measure tip-surface interactions as a function of sample distance.

Measurements of local force variations can be used to link mechanical properties to sample topography.[52] Nanomechanical mapping modes, such as nanoindentation, peak force tapping, and many more are used to generate spatially-resolved quantitative maps of mechanical properties and topography of polymers with nanometer resolution.[9, 54]

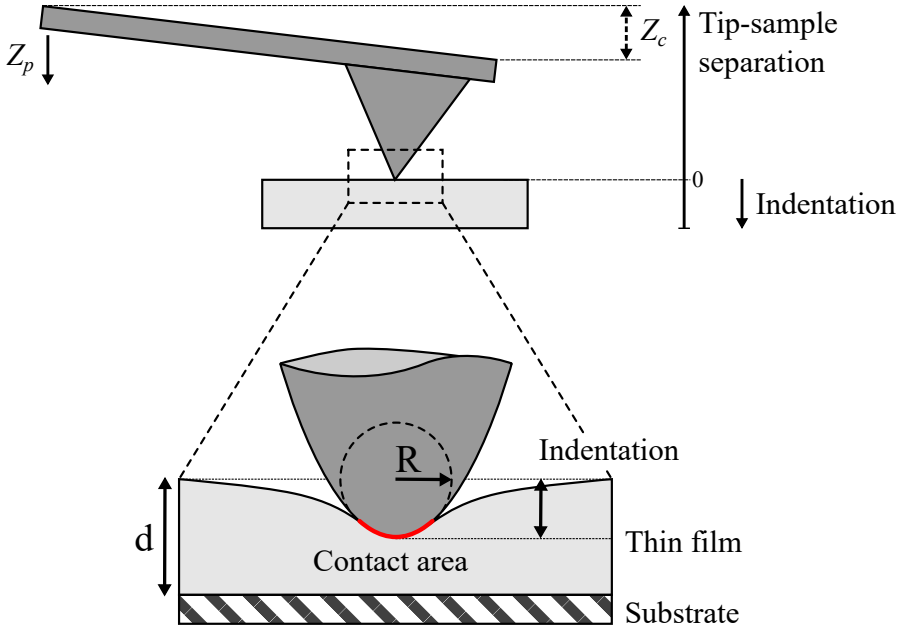


***Fig. 3.3.1.*** (Top) Schematic of the cantilever and tip indenting a thin film sample. The separation between tip and sample is given by the piezo movement $Z_p$ and the deflection of the cantilever $Z_c$ towards or away from the sample, depending whether attractive or repulsive forces dominate the tip-sample interaction. (Bottom) The sample with thickness $d$ deforms upon indentation with the tip. For small indentations, the contact area can be approximated by a sphere with radius $R$ (Hertzian model), whereas other contact theories model the tip, for example, as cones (Sneddon model). The choice of model changes the calculation of the indentation-dependent contact area, and thus the (elastic) force exerted on the cantilever by the sample. Adapted with permission from[54].

A widely used approach is the force-distance curve-based imaging where an AFM tip scans over a specified area of the sample surface, and the corresponding applied force versus tip displacement is determined.[9] Specifically, a cantilever deflection versus position of the piezo normal to the surface is measured. The deflection occurs when the tip interacts with the sample as shown in Fig. 3.3.1. The beam position of the laser reflected from the backside of the cantilever is monitored by the position sensitive photodiode detector depicted in Fig. 3.1.1.

To obtain a force-distance curve, the cantilever deflection and piezo position have to be converted into force and distance by calibrating the spring constant and cantilever sensitivity. The actual tip-sample separation $S$ can be derived from the piezo position $Z_\mathrm{p}$, cantilever deflection $Z_\mathrm{c}$, and indentation depth $\delta$:[55]

$$S = Z_\mathrm{p} + Z_\mathrm{c} + \delta \tag{3.3.1}$$

Using appropriate contact mechanics models, such as the Hertz, Johnson-Kendall-Roberts (JKR), or Derjaguin-Muller-Toropov (DMT) models, the 2D force-distance images can be translated into an areal mapping of the surface mechanical properties, including the elastic modulus, adhesion, dissipation, and stiffness.[9] Each contact mechanics model describes the tip-sample interaction differently. For example, the Hertzian model neglects tip-sample adhesion, whereas the DMT and JKR model consider adhesion forces. An appropriate contact model needs to reflect the expected behavior of the tip-sample interaction. While a hard, weakly adhesive sample would be best fitted with the DMT model, a very soft and adhesive sample is best fitted with the JKR model.

Each data point of the areal map corresponds to a single force-distance curve. A force-curve diagram consists of an extend (approach) and retract cycle as sketched in Fig. 3.3.2. The tip first approaches the sample surface and attractive forces (e.g., adhesion) lead to a bending of the cantilever towards the sample. Upon contact (snap-on point), the cantilever is moved further downwards and the tip indents the sample up to a maximum force setpoint, at which the retract cycle is initiated. The tip is then withdrawn from the sample. However, tip-sample adhesion leads to a hysteresis between extend and retract curve. At a specific withdraw height (snap-off point), the tip looses contact with the surface and the cantilever deflection goes back to zero.

From the extend and retract curves, several elastic properties can be determined. The force at the snap-off point is the tip-sample adhesion $F_\mathrm{Adh}$, and the area between extend and retract curve corresponds to the energy loss (dissipation) of the cantilever due to viscoelastic effects of the sample. The reduced elastic modulus $E^*$ (Young's modulus) is fitted from the marked section of the retract curve in Fig. 3.3.2 with an appropriate contact mechanics model.

The widely used DMT model applies a spherical indenter model (Hertz model) with elastic contact and includes tip-sample adhesion to derive the expression of

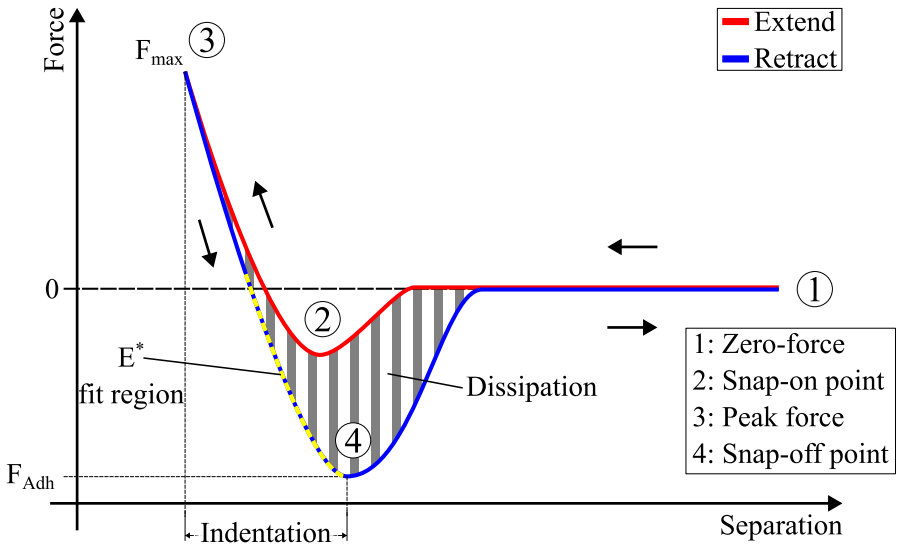


***Fig. 3.3.2.*** Schematic illustration of a complete force-distance curve, consisting of an extend (approach) and retract cycle. The cantilever bends towards the sample and the tip establishes contact with the sample surface when attractive forces dominate, leading to a decrease in force (2). The cantilever bends upwards upon further indentation, up to a maximum indentation force (3), where the tip is retracted. Viscoelastic effects and tip-sample adhesion $F_{\mathrm{Adh}}$ lead to an extend-retract hysteresis (dissipation). The slope of the retract force curve is fitted with a contact mechanics model to obtain the reduced elastic modulus $E^*$. The tip looses contact with the surface at the snap-off point (4) and goes back to zero force (1) when further retracted.

the force $F$:

$$F = \frac{4}{3} E^* \sqrt{R}\, \delta^{1.5} + F_{\mathrm{Adh}} \tag{3.3.2}$$

with the reduced elastic modulus $E^*$, tip radius $R$, indentation $\delta$, and tip-sample adhesion $F_{\mathrm{Adh}}$. The reduced elastic modulus is used to account for tip deformation and is given by the elastic modulus of the sample $E_{\mathrm{s}}$ and the tip $E_{\mathrm{tip}}$:

$$\frac{1}{E^*} = \frac{1 - \nu_{\mathrm{tip}}^2}{E_{\mathrm{tip}}} + \frac{1 - \nu_{\mathrm{s}}^2}{E_{\mathrm{s}}} \tag{3.3.3}$$

with the Poisson's ratio of sample $\nu_{\mathrm{s}}$ and tip $\nu_{\mathrm{tip}}$, respectively. If the elastic modulus of the sample is much smaller than that of the tip, the expression can be simplified to:[54]

$$\frac{1}{E^*} = \frac{1 - \nu_{\mathrm{s}}^2}{E_{\mathrm{s}}} \tag{3.3.4}$$

The $\sqrt{R}$-dependence on the force in Eq. 3.3.2 stems from the contact area of a spherical indenter. However, the tip radius $R$ (and thus contact area between tip and sample) depends strongly on the indentation depth as seen in the bottom part of Fig. 3.3.1. An accurate description of the tip shape is essential for the quantitative determination of elastic properties.[55] Additional difficulties include the exact determination of the point of contact on a soft material, irreversible plastic deformation of the sample caused by a high indentation force, or the effect the laser position on the cantilever has on the deflection sensitivity. Also, the stiffness of the sample needs to be considered when choosing a suitable cantilever for nanoindentation. If the cantilever is too flexible, the tip will not sufficiently indent the sample, and only the cantilever deflection will be detected. Conversely, if the cantilever is too stiff, the force sensitivity will be low, and the sample may be damaged. For thin deformable films the effect of the substrate cannot be neglected. Indentations should be limited to depths much smaller than the total thickness of the sample ($10 - 20$ %) in order to eliminate the influence of the substrate.[55]

In summary, it should be noted that developments in the field of AFM allow for the simultaneous examination of both the topography and the quantitative mechanical properties of polymer interfaces with high measurement speed and spatial resolution. The resulting force curves must be modeled using appropriate contact mechanic models, taking the aforementioned conditions into account, in order to elucidate the elastic properties of polymers. Finally, uncovering and quantifying the structure-property relationship of polymer thin films is a critical

step for the development of novel functional materials.[52]

# 4. Topography and Elastic Properties of Conductive Polymer Thin Films

## 4.1. Tailoring the Properties of Conductive Polymers

Since the 1980s, the investigation of the properties of conductive polymers, such as polypyrrole (PPY), has received considerable attention. As described in Section 2.3., these so-called 'synthetic metals' combine the electrical conductivity of metals with the flexibility of polymers, thereby enabling their application in various fields. As a result, they have been extensively studied as promising novel materials for applications in energy storage, biomedical technology, coatings, and sensors.[4, 5, 27, 29]

Among conductive polymers, PPY is of particular interest, owing to its high conductivity, stability in the oxidised state, and interesting redox properties. In the course of electropolymerization (EP), the final morphology of the PPY film can be directly controlled by fine-tuning the preparation conditions and deposition protocol.[20] With this, film features, such as surface roughness, doping level, conductivity, elasticity, and porosity can be readily modified to suit a wide range of devices.

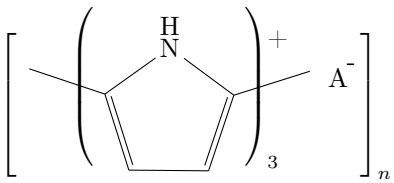


***Fig. 4.1.1.*** Chemical structure of PPY in oxidized form with an anion. Statistically, three pyrrole mer units share a positive charge, which is counterbalanced by a negatively charged anion in the polymer matrix.

For example, PPY microactuators based on bilayered systems require a strong stress-strain response to applied electric potentials for sufficient actuation.[33, 56] As 'artificial muscles', a robust, strong, and fast electro-mechanical response is critical in the design of actuator geometries.[57] The strain, or film swelling is generally caused by incorporation and expulsion of ions in the polymer matrix, including their solvation shell, when the PPY is oxidized and reduced. Larger film swelling can be achieved by using deposition protocols, which, for example, result in a highly porous film, while retaining high conductivity and mechanical stability. On the other hand, PPY-based energy storage devices, such as supercapacitors, should

exhibit low actuation in order to maintain mechanical integrity and prevent film delamination. Furthermore, they require a high redox cycling stability and high pseudocapacitance for reliable energy storage.[58, 59] This can be accomplished by using a potentiodynamic or pulsed deposition protocol, where repeated electrical potential cycling leads to the formation of a dense and smooth film with excellent stability, high pseudocapacity, and low actuation.[59]

Among the remaining key challenges is the need to characterize and quantify the electrical and elastic properties of PPY thin films, particularly in relation to their topography, internal structure, and interfacial effects while under working conditions. Employing a detailed *in situ* electrochemical Atomic Force Microscopy (EC-AFM) approach, the following work investigates the structure–property-correlation between elastic properties and surface morphology in a dense PPY thin film under electrochemical conditions. Given the impact of structural heterogeneity on the elastic modulus in PPY films, our results highlight the importance of smart interface design in the creation of novel electroactive materials.

## 4.2. Mapping the Nanoscale Elastic Property Modulations of Polypyrrole Thin Films in Liquid Electrolyte with EC-AFM

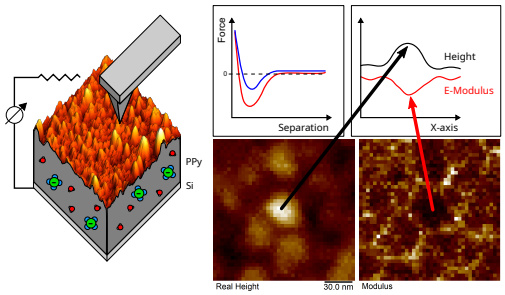


Graphical abstract. Reproduced with permission from[60].

### Bibliographic Information

The following chapter is published in:

A. Meinhardt, P. Lakner, P. Huber, and T. F. Keller, *Nanoscale Adv.*, 2024, **6**, 102 – 110.[60]

The Supporting Information of this chapter is shown in the appendix of this thesis, on page 107.
The data supporting the findings of this study are available from the author upon reasonable request.

### Authors' contributions

I contributed to this work by performing the Atomic Force Microscopy (AFM) experiments, analyzing the data, and writing the manuscript as main author. I also performed the sample preparation with the support of P. Lakner. Some of the experimental work was performed during my master studies, but was expanded upon during my PhD. The manuscript was finalized and corrected with the help of all co-authors.

### Copyright notice

Nanoscale Advances

ROYAL SOCIETY OF CHEMISTRY

PAPER

View Article Online
View Journal | View Issue



Cite this: *Nanoscale Adv.*, 2024, **6**, 102

# Mapping the nanoscale elastic property modulations of polypyrrole thin films in liquid electrolyte with EC-AFM†

Alexander Meinhardt, *[ab] Pirmin Lakner,[ab] Patrick Huber [acd] and Thomas F. Keller *[ab]

Linking structure to mechanical and elastic properties is a major concern for the development of novel electroactive materials. This work reports on the potential-induced changes in thickness and Young modulus of a substrate supported, perchlorate doped polypyrrole thin film (<100 nm) investigated with electrochemical atomic force microscopy (AFM) under *in situ* conditions. This was accomplished by nanomechanical mapping of potentiodynamically electropolymerized polypyrrole film in electrolyte solution with AFM during redox cycling. The polypyrrole film thickness and Young modulus follow the electrical potential nearly linearly, increasing due to solvent and ion influx as the film is oxidized, and decreasing during reduction. Our measurements also confirm the presence of a potential-independent, passive swelling which is accompanied by softening of the film, likely caused by osmotic effects. Additionally, the heterogeneous distribution of the Young modulus can be directly traced to the typical nodular surface topography of polypyrrole, with the top of the nodular area possessing lower modulus, thus highlighting the complex relationship between topography and elastic properties.

Received 7th August 2023
Accepted 21st November 2023

DOI: 10.1039/d3na00611e

rsc.li/nanoscale-advances



## Introduction

Conductive polymers such as polypyrrole (PPy) have received a lot of interest due to their potential in a wide range of applications. Their high electrical conductivity, stability, and mechanical response when subjected to applied electrical potentials make them ideal candidates for applications in microactuators, sensors, supercapacitors, and many more.[1–9] The volume expansion/contraction PPy undergoes during reversible oxidation and reduction is associated with the ion (and/or solvent) diffusion into and out of the polymer matrix.[8,10–12] It is well known that perchlorate doped PPy shows largely anion-dominant ion transport properties and experiences anion influx to the polymer matrix upon oxidation, leading to volume expansion.[2] Since the kinetics of these doping–undoping processes and the electrochemical responses are highly dependent on the electrochemical surface properties, characterizing nanoscale variations in the interfacial properties such as topography, adhesion, and elasticity is an important factor when considering possible influence on interactions with other interfaces when designing applications.[3,12–15] PPy offers the advantage of combining low operating voltages with good biocompatibility while showing electrochemical actuation comparable to, or larger than piezo ceramics, making it an attractive candidate for biomedical actuators. Recently, a study performed on a nanoporous silicon-PPy composite membrane concluded that although the macroscopic behavior of these actuation properties is well understood, there still remain fundamental questions on the influence of the systems' microstructure on its macroscopic properties.[7,8] However, this issue is not exclusive to hybrid systems, but also applies to other sample geometries, *e.g.* thin films.

AFM has emerged as a versatile and powerful tool to not only characterize the surface morphology and topography, but also to simultaneously measure and map the elastic properties of polymer surfaces.[14–23] A cantilever with a sharp tip can reliably sense tip–sample interaction forces in the piconewton regime, enabling the investigation of polymers and soft biological samples under liquid environment conditions.[24,25] Force–distance curves are commonly recorded as the result of probing the sample surface with a cantilever tip by nanoindentation. Analysis of those curves offers an insight into the elastic properties of polymers and soft matter. Utilizing the tip–surface interactions to record a nanometer-scale 2D mapping of the mechanical and topographical properties of the surface provides unique means of linking structure to properties, thus

[a]*Centre for X-ray and Nano Science (CXNS), Deutsches Elektronen-Synchrotron DESY, Hamburg, Germany. E-mail: alexander.meinhardt@desy.de; thomas.keller@desy.de*
[b]*Department of Physics, Hamburg University, Hamburg, Germany*
[c]*Hamburg University of Technology, Institute for Materials and X-Ray Physics, Hamburg, Germany*
[d]*Center for Hybrid Nanostructures CHyN, Hamburg University, Hamburg, Germany*

† Electronic supplementary information (ESI) available: Details of the electrochemical cell used for electropolymerization, the *in situ* AFM setup, cyclic voltammogram and complementary AFM data. See DOI: https://doi.org/10.1039/d3na00611e

opening pathways for the development of more advanced materials.[17]

It is well known that the elastic properties of PPy can be influenced by many factors, such as the type of dopant salt, solvent, synthesis, and many more. Utilizing these factors, Young's moduli ranging from 0.03 GPa up to 1.50 GPa have been achieved.[26] For a perchlorate-doped, freestanding PPy film, a Young's modulus of up to 500 MPa has been recorded by macroscopic tensile strength tests.[27] The film showed a linear relationship between charge, strain, and elastic modulus during redox cycling. As the PPy film was oxidized at higher potentials, it experienced hardening due to solvent and perchlorate induced swelling. While macroscopic tensile tests offer useful insight about the global behavior of the PPy film, they lack information about the influence of the PPy film surface properties on its electrochemical behavior. Mapping the mechanical and topographical properties of PPy thin films *via* nanoindentation with AFM under electrochemical conditions is necessary to unravel the complex relationship between surface structure and properties of conductive PPy thin films.

Therefore, this study aims to illuminate the complex relationship between topography and mechanical properties of perchlorate doped thin PPy films (<100 nm) during redox cycling with *in situ* EC-AFM. Hereby we focus on the potential induced changes in film thickness and elastic modulus determined from fast-recorded nanoindentation curves. We also observe a potential independent change likely caused by osmotic effects.

## Experimental

### Materials and methods

All chemicals were purchased from Sigma-Aldrich. Pyrrole was distilled prior to use. Ultrapure water was taken from a water purification system (18.2 MΩ m). The potentiodynamic electropolymerization and subsequent *in situ* experiments were performed using a potentiostat with a three-electrode setup. All potentials are shown relative to the reference electrode.

### Substrate preparation

The sample substrate consisted of a p-doped (100)-oriented silicon wafer. To remove the native silicon oxide layer on the silicon wafer, the wafer was first immersed in an aqueous solution of 40% ammonium fluoride and 0.05 M ammonium sulfite for five minutes and then rinsed with water and dried under nitrogen flow.

### Polypyrrole electropolymerization

The substrate was fixed in a custom electrochemical cell for electropolymerization of PPy (Fig. S1†). The cell utilized a three-electrode setup containing the substrate as working electrode (WE), a Pt wire as counter electrode (CE), and an Ag/AgCl electrode as reference electrode (RE). The cell was then filled with acetonitrile solution of 0.1 M pyrrole and 0.1 M lithium perchlorate. Potentiodynamic electropolymerization was performed by cycling the potential 200 times between 0.3 V and 1.1 V at a potential scanning rate of 1 V $s^{-1}$. After electropolymerization, the PPy film was carefully rinsed with water and transferred to the AFM.

### AFM (in air, in liquid/EC-AFM, force spectroscopy)

The AFM measurements were performed using a Dimension Icon AFM (Bruker).[28] Small areas of the PPy film were scratched off with tweezers to act as a planar reference during the experiments (Fig. S3 and S7†). Measurements in air were performed using standard tapping cantilevers (RTESPA-300, Bruker). 1 × 1 μm scans were recorded in tapping mode near the substrate with a resolution of 256 × 256 pixels and a scan rate of 0.5 Hz.

For the potential dependent *in situ* experiments, the PPy film was placed in a fluid cell and connected to a three-electrode setup, with the substrate as working electrode and Cu wires fixed above the sample as counter electrode and reference electrode (Fig. S2†). The film was then covered with 0.1 M sodium perchlorate solution (aq.) and given a few minutes to stabilize before the start of the measurements. Silicon nitride cantilevers were employed during the *in situ* measurements (SCANASYST-FLUID+, Bruker) and a splash shield cover was used to minimize electrolyte evaporation. The measurements were performed using the 'Electrochemistry PeakForce Quantitative Nano-Mechanics' (EC-QNM) mode of the Dimension Icon. PeakForce EC-QNM enables the measurement of elastic properties while applying electrical potentials and performing fast force–distance curves. The sample was first imaged with no potential applied by scanning a 1 × 1 μm area near the substrate with a resolution of 512 × 512 pixels at a scan rate of 0.5 Hz.

The PPy film was then investigated at different electrical potentials. Constant potentials ranging from 0.0 V to 0.3 V were applied and the sample was imaged after pausing a few minutes after each potential change to account for non-equilibrium effects. A series of 5 × 5 μm scans with a resolution of 256 × 256 pixels and a scan rate of 0.5 Hz were taken as shown in Fig. S5.† This technique will be referred to as 'static' method below.

Additionally, cyclic voltammetry was performed while imaging the PPy film. A periodic triangular potential between 0.1 V and 0.3 V with a potential scanning rate of 10 mV $s^{-1}$ was applied. During electrochemical cycling the AFM slow scan axis was disabled, which resulted in the AFM tip repeatedly scanning the same line, thus enabling direct tracking of the potential dependent film thickness and elastic modulus evolution. The principle is shown in Fig. S6.† Line profiles of 1 μm length with a resolution of 512 pixels were continuously collected at a scan rate of 1 Hz over the duration of several redox cycles. This method will be referred to as 'dynamic' method below. The film remained stable for several hours within the electrolyte. After excessive potential cycling, it showed signs of partial delamination.

The PPy film was then stored in air for about a year. Subsequently, the sample's elastic properties were investigated with the QNM mode of the Dimension Icon. A standard tapping cantilever was used (RTESPA-300, Bruker) and calibrated beforehand, yielding a spring constant of 22.7 N $m^{-1}$ and

a deflection sensitivity of 83.3 nm $V^{-1}$. A force setpoint of 100 nN was used during the simultaneous mapping of PPy film topography, reduced elastic modulus, and adhesion. A systematically optimized force setpoint was chosen to ensure a sufficient indentation depth while maintaining film integrity as seen in Fig. S8.† For a force setpoint >100 nN, the image contrast got worse, indicating sample or tip damage. The tip radius was determined to be 34 nm after optimization of the force setpoint and was used as an upper limit for the tip radius, while the actual resolution at 100 nN was much better.

## Results

### Electropolymerization of polypyrrole

A thin film of perchlorate doped PPy was deposited *via* potentiodynamic electropolymerization. The used deposition protocol is known to produce dense, adherent films with low porosity and high conductivity.[4,6,29,30] In Fig. 1, the cyclic voltammogram of the PPy electropolymerization shows how the current, and correspondingly the transferred charge originating from oxidization and reduction of the growing film increase each cycle. The increase of the area enclosed by the cyclic voltammogram per cycle indicates continuous film growth. The transferred charge during synthesis is determined to be 171 ± 3 mC by integration of the area enclosed by the cyclic voltammogram. By utilizing standard literature growth rates,[9,31,32] a PPy film thickness of 44.5 ± 2.7 nm is calculated.

### AFM in air & electrolyte

After synthesis, the PPy film was studied in air with AFM tapping mode, revealing the typical cauliflower PPy surface topography made up of globular areas of varying sizes. The film thickness was measured by scanning along the free-scraped substrate area and the PPy film as shown in Fig. 2. Using the free scratched substrate area as baseline, an average PPy film thickness of 48.4 ± 2.1 nm is determined, a value in good agreement with the film thickness calculated from the transferred charge during electropolymerization.

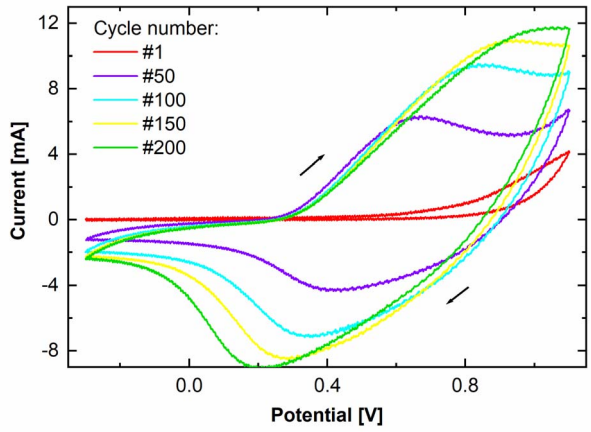


Fig. 1 Cyclic voltammogram of the PPy electrodeposition for 200 cycles. Shown are the first, 50th, 100th, 150th, and 200th cycle.

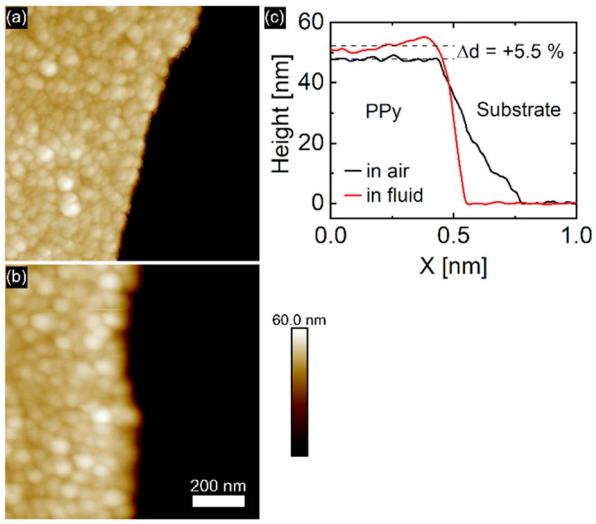


Fig. 2 PPy topography in air (a) and when immersed in perchlorate solution (b) recorded with AFM. (c) Comparison of average PPy height profiles between air and fluid environment, showing a solvent induced swelling of 5.5%.

Solvent induced height changes up to 70% have been reported in the literature.[2,11,26] Recent reports of PPy electropolymerized under similar conditions as ours reported a swelling ratio of 3.7% upon submersion of the film in perchloric acid.[6] In our case, immersion of the PPy film in 0.1 M (aq.) $NaClO_4$ solution was accompanied by an 5.5% increase in film thickness compared to the dry state caused by solvent intake visible in Fig. 2c. The absence of protons in neutral aqueous electrolyte solutions usually leads to a higher swelling capacity, since no protons can partake in charge compensation.[6] While there are many factors that influence the rate of PPy swelling in electrolyte environment, it is generally known that PPy electropolymerized in non-aqueous media and deposited under potential control produces dense and highly conductive PPy films.[6,29,30] Additionally, the use of large, bulky anions (*e.g.* perchlorate, sulfonate) yields PPy films with low roughness and high homogeneity.[33] The PPy film roughness changed from 2.3 nm to 2.8 nm upon immersion of the film in electrolyte.

### EC-QNM AFM (static/dynamic method)

As polymer relaxation, electric transport, and ion and solvent diffusion all take place on different time scales during electrochemical potential cycling of PPy, it is necessary to use a static method, where the film is assumed to be in equilibrium while applying a constant electrical potential during the AFM measurements, as well as a dynamic method, where potential is varied while changes of the PPy topography and elastic properties are recorded as a function of electric potential. This gives access to the different processes involved during the potential cycling of the PPy sample.

With the static method, the PPy film was investigated in perchlorate electrolyte with EC-QNM AFM at defined potential steps ranging from 0.0 V to 0.3 V with enough time (1–2 minutes) given for the film to adjust to the applied potential

before imaging. Image drift shows the same tendency at every potential. All topographic data is accordingly drift-corrected by 1st order plane fitting in $x$- and $y$-axis on the exposed substrate area. Then the average height and elastic modulus of the film are determined at every potential step as shown in Fig. 3. As the PPy is oxidized, the film expands, yielding a swelling ratio of 17% $V^{-1}$.

In order to monitor the topographical and elastic changes of the PPy film at shorter timescales, a setup similar to earlier investigations of PPy is used.[2,11,13] Fast processes taking place at shorter timescales include ion and solvent diffusion into and out of the PPy film for charge compensation upon oxidation and reduction and changes in PPy backbone such as bond length, chain conformation, and interchain interactions, whereas effects such as osmotic expansion caused by osmotic pressure are more pronounced at longer timescales.[6,11,34,35] The 'dynamic' method utilizes cyclic voltammetry and AFM simultaneously. The issue of time-limitation due to the scanning probe working principle of AFM is eliminated by disabling the slow scan axis as illustrated in Fig. S6.† A continuous series of line profiles was recorded while cycling the electrical potential from 0.1 V to 0.3 V with a cycling rate of 10 mV $s^{-1}$. The results shown in Fig. 4a reveal potential induced thickness changes of 0.5–0.6% per cycle (2.5–3.0% $V^{-1}$ swelling ratio). Additionally, a constant potential-independent thickness increase of 0.8% over the duration of the measurement was observed.

### Force curves & elastic modulus

The EC-QNM AFM mode employed during the *in situ* experiments is specifically designed for the nanomechanical determination of elastic properties and the topography of sample surfaces.[20,22] By performing a fast approach–retract cycle of the cantilever at every pixel of the image, the bending of the cantilever caused by indentation probing of the sample surface can be converted into force–distance curves as shown in Fig. 5a. These fast-recorded force curves are then analyzed on-the-fly, achieving high-resolution mapping of sample topography and elastic properties (Fig. 5b–d) of the sample.

Before analysis, a suitable indenter model is chosen. Assuming a spherical indenter for small indentations and tip–sample adhesion, the Derjaguin, Muller, and Toporov (DMT) model was used for the calculation of elastic modulus.[18,19] The formula is given below

$$F = \frac{4}{3}E^*\sqrt{R}\,\delta^{1.5} + F_{\mathrm{adh}}$$

with force $F$, the reduced elastic modulus $E^*$, the tip radius $R$, indentation $\delta$, and the tip–sample adhesion $F_{\mathrm{adh}}$. The model was applied to the retract part of the force–distance curves. The reduced elastic modulus $E^*$ is related to the elastic modulus and Poisson's ratio of both indenter tip and PPy sample as shown below:

$$\frac{1}{E^*} = \frac{1-\nu_{\mathrm{tip}}{}^2}{E_{\mathrm{tip}}} + \frac{1-\nu_{\mathrm{PPy}}{}^2}{E_{\mathrm{PPy}}}$$

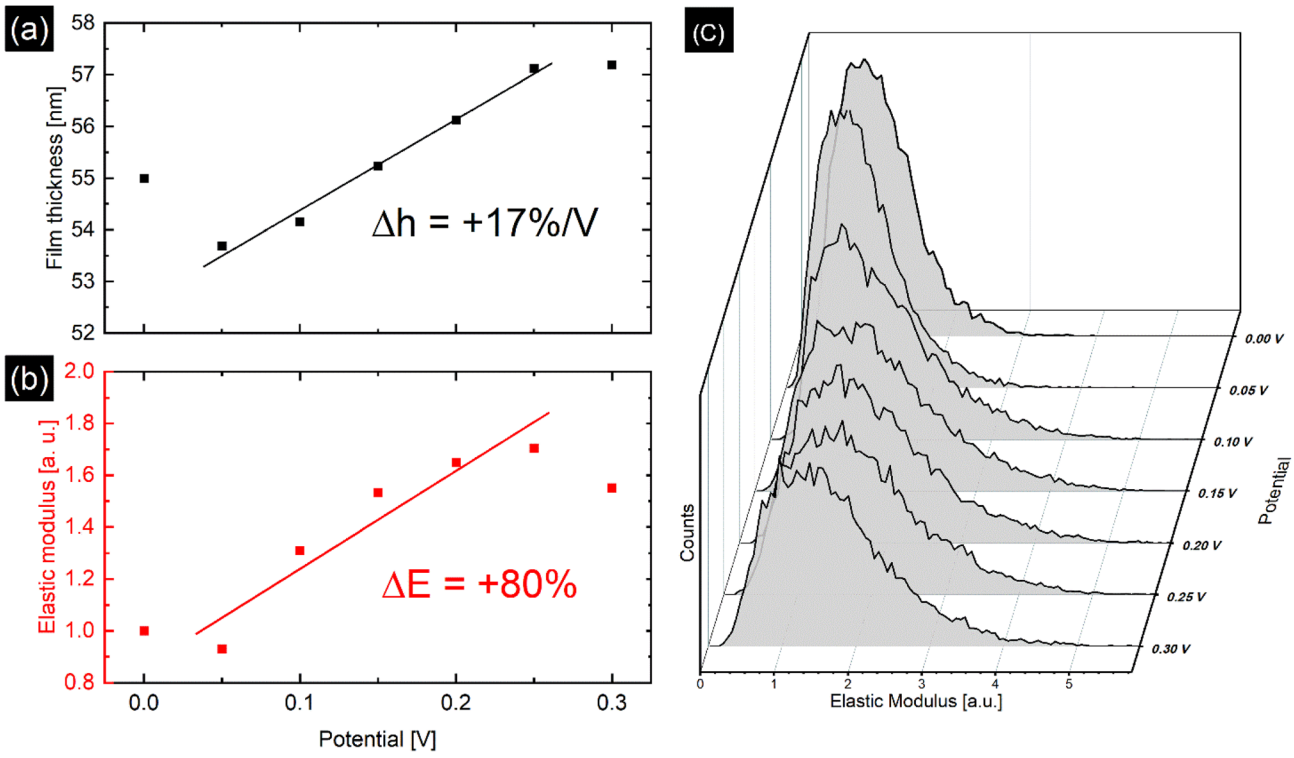


Fig. 3 (a) Potential dependent film thickness measured *via* static method with linear fit, yielding a swelling ratio of 17% $V^{-1}$. (b) Relative changes in Young modulus normalized with respect to the modulus at 0.0 V with linear fit, showing an increase of 80%. The deviation from the linear trend seen at 0 V and 0.3 V is attributed to nonequilibrium effects such as chain relaxation. (c) Distribution of elastic modulus of the PPy area marked in Fig. S5† for every applied potential. The modulus distribution shifts and widens under oxidizing conditions.

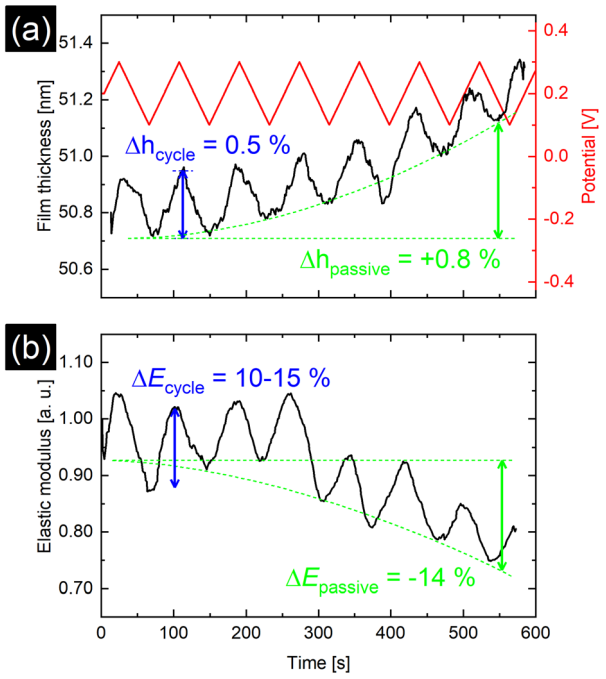


Fig. 4 (a) Dynamic method results for film thickness over time. Periodic triangular potential ranging from 0.1 V to 0.3 V with a potential cycling rate of 10 mV $s^{-1}$ over time is shown in red. (b) Evolution of average reduced elastic modulus over time. Both film thickness and elastic modulus closely follow the applied potential. Additionally, a potential independent swelling, coupled with softening of the PPy film over several redox cycles is visible.

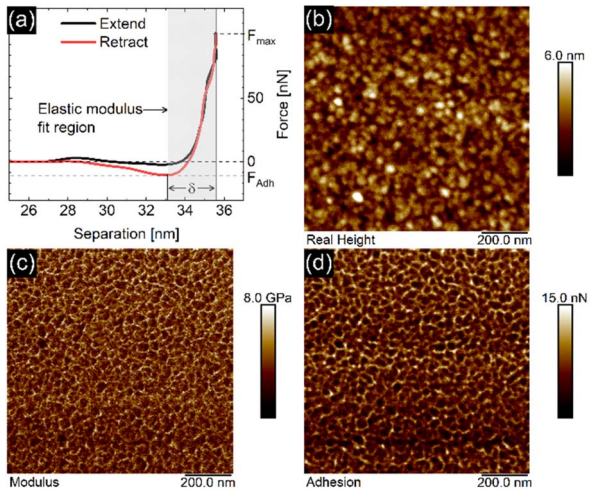


Fig. 5 (a) Force–distance curve recorded on an aged PPy in air with a setpoint of 100 nN peak force, consisting of an extend and retract part. The maximum force setpoint $F_{max}$, the adhesion $F_{adh}$, and indentation $\delta$ are shown. The grey area denotes the fit region used for the indenter model to calculate the elastic modulus. (b) Height, (c) elastic modulus, and (d) adhesion maps calculated from the recorded force curves at every pixel in a 256 × 256 pixel QNM AFM image.

Our results for the *in situ* experiments are normalized with respect to the first data point, since no calibration of the cantilever could be performed in liquid. As such, we report the relative changes in $E^*$.

The PPy film shown in Fig. 5 reveals a heterogeneous distribution of its elastic modulus, with the top nodules of the cauliflower-like topography possessing a lower $E^*$ and lower adhesion than the periphery. This correlation is shown in Fig. 6a and b, where the modulus and adhesion are plotted against the measured height at every pixel of Fig. 5. A clear relationship between modulus and adhesion is visible, suggesting that the protruding top of the nodular cauliflower-like structures is not only softer (lower modulus), but shows also lower adhesion to the tip than the lower valleys of the PPy microstructure. Comparison of selected force curves from both the top of the nodules and the surrounding periphery in Fig. 6c confirm the observed trends from the pixelwise consideration in Fig. 6a and b, and clearly reveals the differences in adhesion and, from the slope of the tip–sample contact area, elastic modulus.

Fig. 3b and c show the time and potential dependent evolution of the average $E^*$ and its distribution during the static method measurement of the polypyrrole area illustrated in

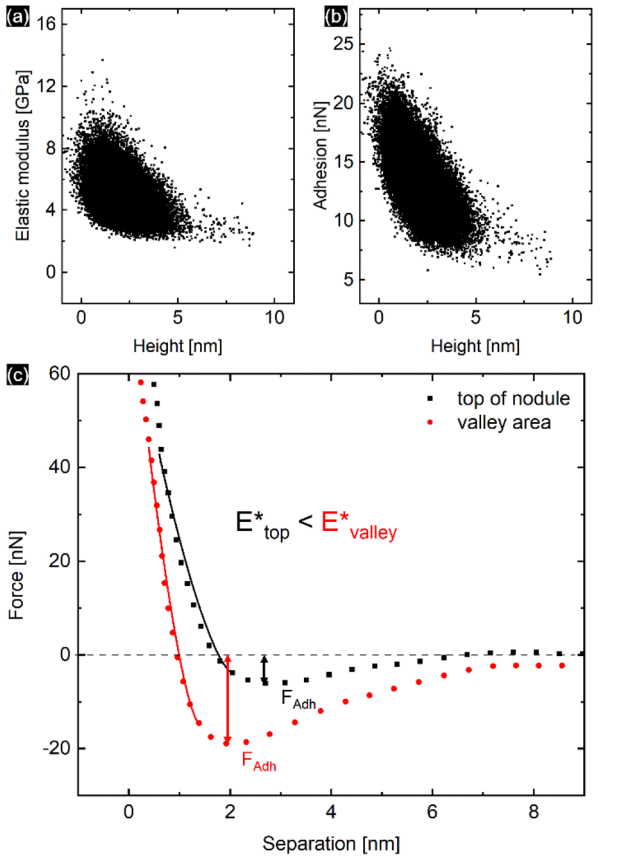


Fig. 6 Elastic modulus (a) and adhesion force (b) taken at every pixel of the elastic property maps shown in Fig. 5 and plotted against the height of the corresponding pixels, showing a clear correlation between the two elastic properties of the aged PPy film. (c) Comparison of the retract parts of two different force curves, one from the top of the nodular areas, and the second one from the surrounding lower periphery. The solid lines represent the DMT indenter model fits for the elastic moduli, while the minimum force is defined as tip–sample adhesion force.

Fig. S5.† Along with a film thickness increase with increasing potential, the average $E^*$ rises up to 80% of its original value, while the distribution of modulus widens. However, with the dynamic method presented in Fig. 4b, potential induced $E^*$ changes of only 15% were observed. Additionally, over the duration of the dynamic experiment a passive, potential-independent softening of the PPy film was observed.

## Discussion

### EC-QNM AFM – height

It is well established that when perchlorate doped PPy is oxidized at higher potentials, ions from the electrolyte move into the polymer matrix for charge compensation.[4,6,13,29,30,36,37] Oxidation of perchlorate-doped PPy films leads to expansion due to influx of perchlorate anions and solvent as reported by the literature and observed in Fig. 3a and 4a.[3,13,27,38] The film thickness in Fig. 3a follows the potential nearly linearly, increasing as the potential increases. This indicates that the ion diffusion during the redox cycling is anion-prevalent. As the PPy backbone is oxidized, negatively charged perchlorate anions diffuse into the polymer matrix, effectively leading to an increase in film thickness. The observed deviation of the linear relationship between potential and PPy thickness at 0.0 V in Fig. 3a could be caused by the film not having reached an equilibrium at the point the measurement was taken. Another possibility could be mixed ionic transport contributing to the film thickness changes at lower potentials, as it has been observed before.[2,6,29] Lakner *et al.* reported a change in PPy film behavior during electrochemical cycling in perchloric acid with XRR. They concluded that in the lower potential regime charge compensation is primarily driven by proton transfer due to anion depletion of the polymer matrix. This likely stems from electrostatic reasons, as well as low perchlorate concentration in the polymer matrix at reducing potentials, leading to an influx of protons, or as in our case, sodium cations for charge compensation.[6]

The extent of swelling depends mostly on the internal PPy structure, which is largely influenced by the synthesis. Additional factors include the pH value and the concentration and type of the electrolyte salt.[4,6,13,29,30,36,37] PPy films synthesized under similar conditions as ours were reported to have a much lower swelling ratio when electrochemically cycled in perchloric acid.[6] It was noted however, that in a neutral aqueous sodium perchlorate solution the swelling capacity of PPy can be significantly higher, since no protons can participate in the charge compensation.[6,30,39,40]

The smaller swelling associated with the dynamic method (2.5–3.0% $V^{-1}$) as compared to the static method (17% $V^{-1}$) can be explained by the much shorter timescale of the measurement. Scanning techniques like AFM are limited by the scanning speed and image resolution during the data acquisition. While intrinsic contributions to the volume expansion, such as changes in polymer backbone bond lengths due to redox switching, happen on a timescale of a few hundred milliseconds for thin films (<100 nm),[9] a substantial part of volume expansion can be attributed to osmotic expansion with diffusion of solvent and ions into and out of the polymer matrix.[35] The diffusion of solvent and ions and the accompanying rearrangement within the polymer take place over a longer timescale, as can be observed by the continuous increase of the film thickness slope in Fig. 4a. This potential-independent swelling has also been observed by others.[6,27,40] It is related to long-term relaxation processes within the polymer network as well as osmotic effects, causing the film to become thicker and less dense per cycle.[6] Compared to the actuation caused directly by the potential, this passive increase is larger than expected and could explain the discrepancies between the results of dynamic and static method, as the longer timescales in the static case lead to PPy being closer to equilibrium during the measurement. These results imply that solvent swelling of the film together with film relaxation might be more pronounced in long-term measurements. It has also been reported that the swelling and actuation of PPy films depend on the potential sweep rate frequency.[26] For higher frequencies, the actuation decreases, which can be accounted to time-limited diffusion of the ions in the electrolyte during redox cycling, although this effect could be less pronounced in thinner PPy films as reported by Higgins *et al.*[13]

From the box-like shape of the cyclic voltammogram in Fig. S4† we conclude that the used potential range was within the capacitive potential window with no faradaic processes taking place at the electrodes. This ensured that no over-oxidation took place, which would have otherwise led to irreversible degradation of the PPy film.[29]

### EC-QNM AFM – $E^*$

QNM AFM is an operating mode for nanoindentation which oscillates the cantilever below its resonant frequency while performing fast force–distance curves on the sample.[20] It minimizes tip wear and tip induced sample damage through force feedback control, making it an ideal tool for investigations of sensitive thin polymer films *in situ*.[41,42]

The force curve shown in Fig. 5a consists of an extend and retract cycle. When the cantilever moves in close proximity to the sample surface, attractive forces between tip and sample lead to a bending of the cantilever towards the sample until the surface is contacted ('contact point'). As the tip indents the sample, the cantilever is increasingly stronger deflected until a maximum force setpoint is reached and the retract cycle begins. Due to tip-sample adhesion, the extend–retract cycle shows a hysteresis, with the point of minimum force being the 'lift-off point' where the cantilever tip 'snaps' off of the sample surface. Many elastic properties of the sample, such as elastic modulus and adhesion can be determined from the measured force curves. For calculation of the elastic modulus with the chosen indenter model the retract part of the force curve is used. A low indentation depth of 2.4 nm as shown in Fig. S8† is necessary to eliminate substrate effects typical for thin substrate-supported polymer films. Due to the difficult nature of cantilever calibration under *in situ* conditions necessary for the determination of absolute values of the polymer films' elastic properties, we resort to presenting relative changes in

modulus for the *in situ* results in Fig. 3 and 4, and absolute values in Fig. 5 and 6 for the measurement in air with calibrated cantilevers.

As seen in Fig. 5, the elastic modulus of the PPy surface in perchlorate electrolyte is largely heterogeneous, with the top of the nodules appearing softer than their periphery. This distribution is likely caused by local structural variations of the film (*e.g.* porosity and density). We suspect that the lower elastic modulus on top of the nodules is related to the film growth mechanism during electropolymerization, leading to a larger porosity in the nodules themselves. Film porosity as well as nodular size can be fine-tuned by choice of synthesis conditions (*e.g.* solvent, ion, pH, *etc.*) and film thickness.[11]

QNM AFM holds a significant advantage over macroscopic tensile tests typically used in earlier *in situ* investigations of PPy.[13,26] Not only does it offer additional information (*e.g.* adhesion, dissipation) about the films' elastic properties, but also achieves microscale resolution which is essential for evaluating the use of PPy systems in future applications.

Oxidation and reduction of the PPy film causes the diffusion of perchlorate anions and solvent into and out of the polymer matrix. Otero *et al.* found a linear relationship between elastic modulus and potential, which were explained by the reduction of the degrees of freedom of the polymer chains due to swelling, *i.e.*, reflecting a reduced conformational entropy.[27] This is reflected by the increase in $E^*$ caused by oxidation of the PPy film at higher potentials seen in Fig. 3b and 4b. Similar to the film thickness, the average $E^*$ shows a substantially larger potential induced increase of nearly 80% in the static method compared to only 15% increase for the dynamic method and is accompanied by widening of the distribution of $E^*$ as shown in Fig. 3c. The larger modulus increase is attributed to the different timescales in the experiments as discussed before, while the widening of the $E^*$ distribution seems to indicate uneven or inhomogeneous swelling. From the literature, relative $E^*$ changes of up to 200% have been observed and explained by solvent swelling, ionic crosslinking, or ion diffusion.[11,36,43,44] Also, the passive decrease of $E^*$ during the dynamic experiment in Fig. 4b indicates an additional long-term relaxation and solvent influx process, leading to an increase in film thickness coupled with softening of the film, which causes the deviation from the linear trend at higher potentials shown in Fig. 3b. The potential induced height and modulus changes in Fig. 4a and b seem unaffected by this, which hints that this passive change is caused by osmotic effects.[6,35]

### Influence of topography on elastic properties

The heterogeneous distribution of elastic modulus and adhesion of the PPy surface shown in Fig. 3c and 5 is apparently linked to the topography of the cauliflower-like surface structure. While the top of the nodular areas appears to have lower elastic modulus and low adhesion, the surrounding lower periphery possesses a comparably higher elastic modulus and adhesion. This is evident by comparing the dependence of determined elastic modulus and adhesion with the recorded height of the film as shown in Fig. 6a and b. It is likely that this effect is a combination of surface topography and internal morphology of the thin film. It has been shown that concave surface geometries can lead to an increased adhesion.[45] Although our produced films possess remarkably low roughness, the contact area of the tip and sample might vary depending on whether the tip contacts the top of the nodules or the lower 'valleys', thus influencing the indenter geometry and enhancing tip–sample adhesion. There also seems to be a linear relationship between adhesion and elastic modulus, although the exact cause is unclear. Adhesion is primarily affected by the surface potentials, van der Waals forces, and capillary effects, while elastic modulus is mainly influenced by the internal morphology. However, surface roughness can lead to a correlation between both elastic properties.[46] Whereas earlier studies did not find a systematic correlation between surface roughness and the elastic modulus of PPy films, our study has in fact revealed the top of the nodular cauliflower-like structures to be softer than the lower surrounding periphery.[26] We assume this difference must stem from the difference in electrosynthesis conditions (*e.g.* potential control function, solvent, dopants) leading to a completely different microstructure. As it is well known, potentiodynamically deposited PPy thin films synthesized in acetonitrile and doped with compact perchlorate anions are in comparison much denser and smoother than their counterparts synthesized under different conditions.[6] Additionally, we speculate that during electrochemical potential cycling the nodular areas facilitate solvent and dopant ion diffusion more than the lower lying surroundings as they are easier accessible for diffusion processes taking place. Repeated cycling, accompanied with the iterative insertion/extraction of solvent and ion molecules might lead to a selective "break-up" and corresponding softening of the top of the nodular areas due to changes in the PPy microstructure.

## Conclusions

In this study, a perchlorate doped thin film of PPy was potentiodynamically synthesized and investigated under *in situ* conditions with EC QNM AFM. The film thickness as well as the Young modulus of the PPy film were monitored as a function of the electric potential over different timescales *via* fast recorded force–distance curves. Film thickness and elastic modulus follow the potential, both increasing/decreasing as the film is oxidized/reduced due to solvent and ion diffusion. Even though our potentiodynamic synthesis protocol typically produces thin PPy films with a nominal low porosity compared to other synthesis protocols, we observed a swelling ratio of up to 17% $V^{-1}$ and changes in elastic modulus of up to 80%, which were accompanied by a significant potential-independent film swelling coupled with a decrease in modulus over the duration of the experiment. This passive creep can be attributed to osmotic expansion. The high resolution 2D maps of PPy topography and elastic properties recorded with QNM AFM enabled a correlative analysis connecting the PPy film topography with local elastic modulus values and adhesion. The comparison revealed that the higher areas of the PPy nodules possess a lower elastic modulus and tip adhesion force then the

surrounding lower periphery, which we assign to the interplay of the internal morphology (*e.g.* porosity) and the convex–concave cauliflower-like surface structure of the PPy. Therefore, EC QNM AFM shows a clear advantage over classic macroscopic tensile tests used for polymers by providing a microscopic view on the link between surface structure and elastic properties. Our findings highlight the versatility of AFM, enabling measurements of sample topography and its microscopic elastic properties under *in situ* conditions, thus opening a pathway to the development of novel soft electronic materials. Connecting topography with elastic properties and understanding their interdependence is a major component for future material development.

## Conflicts of interest

There are no conflicts to declare.

## Acknowledgements

The authors gratefully acknowledge financial support from the German Research Foundation (DFG) within the Collaborative Research Initiative SFB 986 "Tailor-Made Multi-Scale Materials Systems–M3", project number 192346071, sub-project B7. A. Meinhardt and T. F. Keller acknowledge support by the Helmholtz Foundation through the Helmholtz-Lund International Graduate School (HELIOS, HIRS-0018). The technical discussions with Hartmut Stadler, Bruker Nano Surfaces, Karlsruhe, Germany are gratefully acknowledged.

## Notes and references

1 J. G. Ibanez, M. E. Rincón, S. Gutierrez-Granados, M. Chahma, O. A. Jaramillo-Quintero and B. A. Frontana-Uribe, *Chem. Rev.*, 2018, **118**, 4731–4816.
2 M. Pyo and C.-H. Kwak, *Synth. Met.*, 2005, **150**, 133–137.
3 T. Silk, Q. Hong, J. Tamm and R. G. Compton, *Synth. Met.*, 1998, **93**, 59–64.
4 G. Sabouraud, S. Sadki and N. Brodie, *Chem. Soc. Rev.*, 2000, **29**, 283–293.
5 R. Adhkari, B. Lamsal, T. R. Bhandari, S. P. Khatiwada and G. H. Michler, in *Conjugated Polymers for Next-Generation Applications*, ed. V. Kumar, K. Sharma, R. Sehgal and S. Kalia, Woodhead Publishing, UK, 2022, vol. 1, ch. 4, pp. 113–146.
6 P. H. Lakner, M. Brinker, C. Seitz, L. Jacobse, V. Vonk, M. Lippmann, S. Volkov, P. Huber and T. F. Keller, *Langmuir*, 2020, **36**, 13448–13456.
7 M. Brinker, M. Thelen, M. May, D. Rings, T. Krekeler, P. Lakner, T. F. Keller, F. Bertram, N. Huber and P. Huber, *Phys. Rev. Mater.*, 2022, **6**, 116002.
8 M. Brinker, G. Dittrich, C. Richert, P. Lakner, T. Krekeler, T. F. Keller, N. Huber and P. Huber, *Sci. Adv.*, 2020, **6**, 1–9.
9 B. Roschning and J. Weissmüller, *Electrochim. Acta*, 2019, **318**, 504–512.
10 M. R. Gandhi, P. Murray, G. M. Spinks and G. G. Wallace, *Synth. Met.*, 1995, **73**, 247–256.
11 E. Smela and N. Gadegaard, *J. Phys. Chem. B*, 2001, **105**, 9395–9405.
12 L. T. T. Kim, C. Gabrielli, A. Pailleret and H. Perrot, *Electrochim. Acta*, 2011, **56**, 3516–3525.
13 M. J. Higgins, S. T. McGovern and G. G. Wallace, *Langmuir*, 2009, **25**, 3627–3633.
14 S. Vlassov, S. Oras, M. Antsov, I. Sosnin, B. Polyakov, A. Shutka, M. Y. Krauchanka and L. M. Dorogin, *Rev. Adv. Mater. Sci.*, 2018, **56**, 62–78.
15 P. Knittel, M. J. Higgins and C. Kranz, *Nanoscale*, 2014, **6**, 2255.
16 J. J. Roa, G. Oncins, J. Diaz, F. Sanz and M. Segarra, *Recent Pat. Nanotechnol.*, 2011, **5**, 27–36.
17 D. Wang and T. P. Russell, *Macromolecules*, 2018, **51**, 3–24.
18 H.-J. Butt, B. Cappella and M. Kappl, *Surf. Sci. Rep.*, 2005, **59**, 1–152.
19 B. Cappella and G. Dietler, *Surf. Sci. Rep.*, 1999, **34**, 1–104.
20 T. J. Young, M. A. Monclus, T. L. Burnett, W. R. Broughton, S. L. Ogin and P. A. Smith, *Meas. Sci. Technol.*, 2011, **22**(12), 125703.
21 D. Passeri, A. Alippi, A. Bettucci, M. Rossi, E. Tamburri and M. L. Terranova, *Synth. Met.*, 2011, **161**, 7–12.
22 M. E. Dokukin and I. Sokolov, *Langmuir*, 2012, **28**, 16060–16071.
23 J. Kámán, R. Huszánk and A. Bonyár, *Micron*, 2019, **125**, 102717.
24 L. Sirghi, *Microsc. Sci. Technol. Appl. Educ.*, 2010, **4**, 433–440.
25 K. Łępicka, M. Majewska, R. Nowakowski, W. Kutner and P. Pieta, *Electrochim. Acta*, 2019, **297**, 94–100.
26 A. Gelmi, M. J. Higgins and G. G. Wallace, *Biomaterials*, 2010, **31**, 1974–1983.
27 T. F. Otero, J. J. López Cascales and G. Vázquez Arenas, *Mater. Sci. Eng., C*, 2007, **27**, 18–22.
28 A. Stierle, T. F. Keller, H. Noei, V. Vonk and R. Roehlsberger, *J Large Scale Res. facil. JLSRF*, 2016, **2**, A76.
29 T. V Vernitskaya and O. N. Efimov, *Russ. Chem. Rev.*, 1997, **66**, 443–457.
30 C. Beebee, E. B. Watkins, R. M. Sapstead, V. C. Ferreira, K. S. Ryder, E. L. Smith and A. R. Hillman, *Electrochim. Acta*, 2019, **295**, 978–988.
31 A. Diaz, *J. Electroanal. Chem.*, 1981, **129**, 115–132.
32 S. J. Hahn, W. E. Stanchina, W. J. Gajda and P. Vogelhut, *J. Electron. Mater.*, 1986, **15**, 145–149.
33 U. Paramo-García, J. G. Ibanez and N. Batina, *Int. J. Electrochem. Sci.*, 2013, **8**, 2656–2669.
34 E. Smela, *Adv. Mater.*, 2003, **15**, 481–494.
35 L. Bay, T. Jacobsen, S. Skaarup and K. West, *J. Phys. Chem. B*, 2001, **105**, 8492–8497.
36 R. Z. Pytel, E. L. Thomas and I. W. Hunter, *Polymer*, 2008, **49**, 2008–2013.
37 H. S. Nalwa, *Handbook of Organic Conductive Molecules and Polymers, Conductive Polymers: Synthesis and Electrical Properties*, John Wiley & Sons, 1997.
38 M. F. Suárez and R. G. Compton, *J. Electroanal. Chem.*, 1999, **462**, 211–221.
39 J.-H. Hwang and M. Pyo, *Synth. Met.*, 2007, **157**, 155–159.

40 K. Kaneto, Y. Sonoda and W. Takashima, *Jpn. J. Appl. Phys.*, 2000, **39**, 5918–5922.
41 E. Smirnova, A. Ankudinov, I. Chepurnaya, A. Timonov and M. Karushev, *Inorganics*, 2023, **11**, 1–11.
42 S. Jafarzadeh, P. M. Claesson, P.-E. Sundell, J. Pan and E. Thormann, *ACS Appl. Mater. Interfaces*, 2014, **6**, 19168–19175.
43 W. Zheng, P. G. Whitten and G. M. Spinks, *Multifunct. Mater.*, 2018, **1**, 014002.
44 G. M. Spinks, L. Liu, G. G. Wallace and D. Zhou, *Adv. Funct. Mater.*, 2002, **12**, 437–440.
45 J. F. Waters, H. J. Gao and P. R. Guduru, *J. Adhes.*, 2011, **87**, 194–213.
46 A. G. Peressadko, N. Hosoda and B. N. J. Persson, *Phys. Rev. Lett.*, 2005, **95**, 124301.

## 4.3. Summary

As outlined, the intricate structure–property relationship of polymers leads to their use across various technological fields. Among them, conductive polymers combine highly tunable conductivity with extraordinary mechanical properties, which leads to novel applications in energy storage, biomedicine, flexible electronics, sensors, and more.[4, 5, 27, 29] We demonstrated how the nanoscale surface topography of a PPY thin film is closely correlated to its elastic properties. The film's roughness gives rise to a heterogeneous lateral modulation of the elastic modulus on the film surface. Optimizing and characterizing the interfacial properties of conductive polymer thin films are fundamental steps in designing innovative applications. Especially in the design of hybrid and composite materials, interface engineering is used to enhance the functionality and performance of devices.[58]

# 5. Block Copolymer Crystallization in Thin Films for Nanopattern Self-Assembly

## 5.1. Enhanced Segregation Strength via BCP Crystallization

The functionality of devices can be further improved through nanostructuring, which provides additional control over their physical properties.[61] A promising route for bottom-up nanopatterning is the self-assembly of block copolymer (BCP) thin films. The ability of BCP thin films to microphase separate into various nanostructures can be utilized for the fabrication of novel functional materials in the sub-10 nm regime, such as nanolithographic templates, nanowires, nanoarrays, optoelectronics, and more.[62, 63] However, sufficient incompatibility between the constituent copolymer blocks, a high $\chi$, is required for self-assembly. As described in Section 2.4. by the Flory-Huggins theory, enthalpic and entropic factors contribute to the free energy of the system. Given that the dimensions of the microphase separated BCPs are related to the length $N$ of the blocks, the fabrication of sub-10 nm surface nanostructures necessitates the development of high-$\chi$, low-$N$ BCPs.[13] Additionally, a major concern in BCP-based nanopatterning is the improvement of order, orientation, and defect mitigation by investigating the processing and annealing conditions in thin films.[63]

Crystallization presents a promising way to introduce high and long-range order to surface nanopatterns of BCPs. The driving forces in crystallization, which are significantly stronger than typical forces in the microphase-separation of amorphous BCPs, influence the microphase morphology and lead to an increase in the effective interaction parameter $\chi_{eff}$.[37] Therefore, the crystallization of a short-chain poly(ethylene)-*block*-poly(ethylene oxide) (PE-*b*-PEO) thin film is explored. We elucidate the influence extended-chain BCP crystallization has on the formation of vertical surface morphologies to develop a pathway towards the fabrication of nanostructures in the sub-10 nm range.

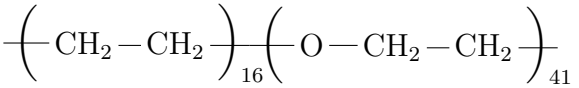

***Fig. 5.1.1.*** Formula of the used PE-*b*-PEO with 16 polyethylene (PE) and 41 polyethylene oxide (PEO) units.

It is well established that the sequential crystallization of linear, low molec-

ular weight PE-*b*-PEO results in the formation of a double-crystalline lamellar morphology of extended-chain crystals. In bulk, the polyethylene (PE) block crystallizes unconfined by the amorphous polyethylene oxide (PEO) block, while the PEO crystallization is confined in between the crystalline PE lamellae.[47] In the double-crystalline lamellae, the PE chains are tilted $\sim 22^{\circ}$ from the lamellar normal, while the PEO chains are parallel to the lamellar normal. This is explained by the different crystal structures (PE orthorhombic, PEO monoclinic), in which both copolymer blocks crystallize.[47, 64] For asymmetric PE-*b*-PEO block lengths, various microphase transitions from the double-crystalline state, to the single-crystalline state, and amorphous state have been detected. The microphases transition between lamellae, gyroid, and cylinders as a result of thermally-activated chain motion.[65] The different mesophases lead to varying degrees of topological confinement and interactive crystallization, therefore affecting the final micro- and nanostructures in bulk PE-*b*-PEO.[66]

Similar to the bulk crystallization, thin films of PE-*b*-PEO have been reported to form extended-chain morphologies.[64] First, drop-cast thin films of asymmetric PE-*b*-PEO formed discrete terraces of extended, standing chains. Upon thermal annealing on neutral substrates, the chains reoriented to become parallel to the surface, and extended-chain vertical lamellae appear.[64] However, due to the influence of interfaces on the orientation of the microdomains in thin films, vertical lamellae could only form on neutral substrates. It is commonly known that non-preferential, neutrally functionalized substrates allow the formation of vertical morphologies, because they possess a low interfacial energy with both copolymer blocks.[6]

Investigating the properties of double-crystalline BCP thin films is especially relevant for the design of nanopatterned arrays for alternative lithographic methods. As described earlier (Section 2.4.1.), interactions at interfaces determine the wetting and orientation of the nanodomains in thin films. Additionally, the interactions at interfaces also affect the crystallization kinetics and orientation of the crystal domains. Crystallization in PE-*b*-PEO thin films could offer an innovative approach for the fabrication of nanopattern in the sub-10 nm range, but the mechanism behind the formation of extended-chain, vertical crystal lamellae remains unclear. Furthermore, there is a need to control the orientation and defect density of the vertical lamellae macroscopically via directed self-assembly (DSA) methods for future applications.[63]

The following paper reports on a detailed *in situ* Atomic Force Microscopy (AFM) study of the extended-chain vertical lamellae formation in PE-*b*-PEO thin

films. Complemented with an extensive thermodynamic description of the system, we describe the underlying mechanisms leading to the vertical lamellae formation. Our results offer a comprehensive insight in the PE-*b*-PEO thin film dynamics and offer a novel approach for the crystallization-controlled fabrication of stable nanopatterned arrays.

## 5.2. A Pathway Toward Sub-10 nm Surface Nanostructures Utilizing Block Copolymer Crystallization Control

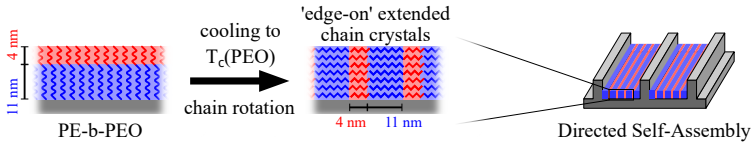


Graphical abstract. Reproduced with permission from[67].

### Bibliographic Information

The following chapter is published in:

A. Meinhardt, P. Qi, C. David, I. Maximov, and T. F. Keller, *Adv. Mater. Interfaces*, 2025, **12**, 6, 2400661.[67]

The Supporting Information of this chapter is shown in the appendix of this thesis, on page 113.

The data that support the findings of this study are openly available (CC-BY 4.0) in [Zenodo] at `https://doi.org/10.5281/zenodo.14202742`

### Authors' contributions

I contributed to this work by performing the sample preparation, AFM experiments, analyzing the data, and writing the manuscript as main author. The nanotemplates for DSA were fabricated by P. Qi, C. David, I. Maximov, and myself. The manuscript was finalized and corrected with the help of all co-authors.

### Copyright notice

RESEARCH ARTICLE

ADVANCED MATERIALS INTERFACES Open Access

www.advmatinterfaces.de

# A Pathway Toward Sub-10 nm Surface Nanostructures Utilizing Block Copolymer Crystallization Control

*Alexander Meinhardt,* Peng Qi, Christian David, Ivan Maximov, and Thomas F. Keller**

**It is elucidated how crystallization can be used to create lateral surface nanostructures in a size regime toward sub-10 nm using molecular self-assembly of short chain crystallizable block copolymers (BCP) and assist in overcoming the high-$\chi$ barrier for microphase separation. In this work, an amphiphilic double-crystalline polyethylene-b-polyethylene oxide (PE-b-PEO) block co-oligomer is used. A crystallization mechanism of the short-chain BCP in combination with neutral wetting of the functionalized substrate surface that permits to form edge-on, extended chain crystal lamellae with enhanced thermodynamic stability. In situ atomic force microscopy (AFM) analysis along with surface energy considerations suggest that upon cooling from the polymer melt, the PE-b-PEO first forms a segregated horizontal lamellar morphology. AFM analysis indicates that the PEO crystallization triggers a morphological transition involving a rotation of the forming extended chain crystals in edge-on orientation. Exposing their crystal side facets to the top surface permits to minimize their interfacial energy and form vertical nanostructures. Moreover, the edge-on lamellae can be macroscopically aligned by directed self-assembly (DSA), one necessity for various nanotechnological applications. It is believed that the observed mechanism to form stable edge-on lamellae can be transferred to other crystallizable short chain BCPs, providing potential pathways for sub-10 nm nanotechnology.**

## 1. Introduction

Molecular self-assembly of block copolymers (BCP) is today used to create structured nanopatterns on thin films exploiting the so called microphase separation arising from the incompatibility between different covalently connected polymer blocks.[1–3] For linear BCPs the resulting morphologies depend on the block incompatibility characterized by the Flory-Huggins interaction parameter $\chi$ and the block lengths.[2,4] In thin films, the film thickness in conjunction with the interfacial energy minimization at the free surface and the substrate interface determine the morphology and govern the wetting behavior, nanopattern orientation, and defect density.[1,5–7] For increasingly smaller microphase separated domains constituting of short BCP chains with length $N$, the driving force for microphase separation ($\chi \times N$) becomes less efficient. To create a sub-10 nm pattern for next-generation lithography therefore requires the use of strongly segregating, so called high $\chi$, low $N$ block copolymers.[1,5,6,8–10]

Arising from the statistical nature of BCP self-assembly perpendicular domains often form in thin BCP films lacking any long-range order, which is undesirable for nanofabrication. In this context, polymer crystallization, which is itself a molecular self-assembly process that creates ordered and selective structures through regular arrangement of polymer chains, can offer attractive means of creating patterned nanostructures with long-range order.[11] Crystallization could provide a complementary, high driving force to assemble nanopattern with ideally increased pattern fidelity. As a nucleation and growth process, the polymer crystal orientation is initially defined by the nuclei, and provided it is not rotating, the forming crystal continues to grow along its growths directions. Existing microphase separated morphologies, interfacial effects, and wetting and dewetting phenomena jointly guide the crystallization with their individual impact.[11]

Indeed, more complex phenomena are involved in crystalline BCP self-assembly compared to amorphous BCPs, and generally, the final morphology depends on the competition between microphase separation and crystallization.[4] The various processes during interactive crystallization can lead to a

A. Meinhardt, T. F. Keller
Centre for X-ray and Nano Science CXNS
Deutsches Elektronen-Synchrotron DESY
22607 Hamburg, Germany
E-mail: alexander.meinhardt@desy.de; thomas.keller@desy.de
A. Meinhardt, T. F. Keller
Department of Physics
University of Hamburg
22607 Hamburg, Germany
P. Qi, C. David
Paul Scherrer Institut
Villigen PSI 5232, Switzerland
I. Maximov
NanoLund and Solid State Physics
Lund University
Lund SE-221 00 Lund, Sweden

The ORCID identification number(s) for the author(s) of this article can be found under https://doi.org/10.1002/admi.202400661



**DOI: 10.1002/admi.202400661**

complex thermodynamic pathway, resulting in different final morphologies.[3,4,8,12–19]

Extended chain crystals represent a subset of polymer crystals in which the chains in the crystal assume a highly stretched conformation (e.g., *all-trans*). Since short-chain oligomers prefer an extended conformation over coil conformation due to the largely reduced conformational entropy and crystallize as extended chain crystals, they are of particular interest for BCP based nanofabrication, offering precise control over pattern size. Furthermore, directed self-assembly (DSA) introduces topographical or chemical patterns that can be utilized, similarly like electrical fields, magnetic fields, or shear forces, to direct the self-assembly of the BCP, align the nanopatterns on a macroscopic scale, and reduce the number of defects.[9,10,20–23]

It is well known that surface-sensitive techniques like atomic force microscopy (AFM) are ideally suited to follow the processes during crystallization in thin films of crystallizable BCPs.[5,11,24–26] The interfacial energy of the BCP with the substrate and atmosphere interface can significantly alter the crystallization kinetics by either hindering or enhancing crystal nucleation and has a strong influence on the polymer crystal orientation and resulting nanopattern, thus offering an additional approach to BCP based nanostructure design.[4,8,13,16,27–32] Therefore, further investigations of crystalline BCP thin film systems are necessary to elucidate the role of crystallization on the nanopattern formation. In this context, a short-chain, double crystalline polyethylene-block-polyethylene oxide (PE-b-PEO) block co-oligomer is an attractive model system which combines amphiphilic properties with biocompatibility, and which forms extended chain crystals, while its homopolymers analogs are widely used.

Moreover, Cao et al. discovered that such a PE-b-PEO in the bulk exhibit more than a single order-to-disorder transition, and passes several stages of morphological transitions upon cooling ranging from a cylindrical phase to gyroid, and finally lamellar morphology at room temperature. They claimed that the morphological transitions were linked to the thermally activated motion of stretched and flexible PE chain segments constrained in geometric confinement rather than being correlated to the PE or PEO crystallization.[33] Sun et al. have found that both PE and PEO blocks of PE-b-PEO co-oligomers in the fully crystalline state form extended chain crystals with PE chains tilted 22° from the lamellar normal and PEO chains parallel to the lamellar normal. In bulk, an interdigitated, single-crystalline layer morphology was observed for both blocks, and the confined PEO crystallization was investigated.[34] Zhang et al. investigated double-crystalline PE-b-PEO BCP bulk-like thick films and found that the topological confinement of the mesophase defined initially by the PE crystallization significantly affected the subsequent PEO crystallization kinetics, although the PEO crystallization then transformed the mesophase into a crystalline lamellar morphology (confined vs breakout crystallization).[15]

While these experiments largely reflect the morphological behavior in the bulk, Schulze et al. observed the formation of vertical lamellae on the top surface of very thin PE-b-PEO films (few $L_0$ thick, $L_0$ being the BCP natural pitch) on chemically modified substrates. After drop-casting, the PE-b-PEO initially formed thin films of extended, vertically oriented chains. Depending on the substrate modification, thermal annealing induced a rotation of the extended chains to surface horizontal, leading to the formation of defined, vertical lamellar nanostructures while maintaining the initial film thickness.[3]

Here, we exploit in situ AFM during thermal annealing of a PE-b-PEO thin film to closely monitor the evolution of surface topography during the formation of vertical lamellar nanostructures. Careful tuning of temperature allows to follow film growth, microphase separation, and crystallization under quasi-stationary conditions. We also demonstrate the ability of PE-b-PEO block co-oligomers to form long range ordered surface nanostructures by using topographic guiding patterns for DSA, a prerequisite for potential applications in nanofabrication. Our results highlight the advantage short-chain extended crystal BCPs have over non-crystalline BCPs, which may offer a novel approach for potential application of BCPs in the fabrication of functional nanodevices.

## 2. Results and Discussion

### 2.1. Morphology During Thermal Annealing

The PE-b-PEO thin film was prepared by drop casting from ethanol solution on a methyl 3-mercaptopropionate (M3M) functionalized, gold coated Si substrate and thermally annealed for 5 min at 120 °C under constant nitrogen flow on the AFM heating stage and cooled with a rate of 2 °C $min^{-1}$ to 25 °C to create a well-defined, reproducible starting morphology of vertical lamellar nanostructures. Subsequently, the in situ AFM experiments were performed under nitrogen atmosphere.

The film after thermal annealing and during the AFM in situ heating experiments is shown in **Figure 1**. In the AFM phase image of the annealed film shown in Figure 1A we observe vertical nanostructures consisting of vertical lamellae with a 'fingerprint'-like orientation and a lamellar size $L_0$ of ≈14.6 nm. The general features of the film shown in the large overview AFM height image in Figure 1B always reappear after thermal re-annealing and are divided into several distinct morphologies: islands with vertical lamellae on the outer and sandwich morphologies in the center region, branched dendrites covering the remaining free substrate surface, and large isolated solidified droplets. The distinct morphologies likely form due to variations in polymer concentrations leading to a locally different thickness, and in turn varying conformations and/or crystallization pathways of PE-b-PEO chains on the sample and will be discussed below.

Figure 1C–K shows selected AFM topographic and phase images recorded during the cooling of the PE-b-PEO film from 120 °to 25 °at 10 °C temperature intervals. Starting at 80 °C, the formation of discrete, topographically flat layers was observed. The planar layers continued to grow laterally as temperature was decreased and additional discrete layers appeared on top of the existing layers. The thickness of each discrete layer shown in **Figure 2** (14.5 ± 0.9 nm) is quantized in integers or half-integers of the calculated extended fully crystalline PE-b-PEO chain length $d_{ext}$ = 15.2 nm (calculation shown in the Supporting Information), indicating that the PE-b-PEO chains are oriented vertical with respect to the substrate surface. Further discrete layers grow on top of existing ones as temperature is slowly decreased. The lateral growth progression is apparent from the bright contrast in the AFM phase image in Figure 1F, where one can clearly distinguish between the equilibrated center of the discrete layer and the

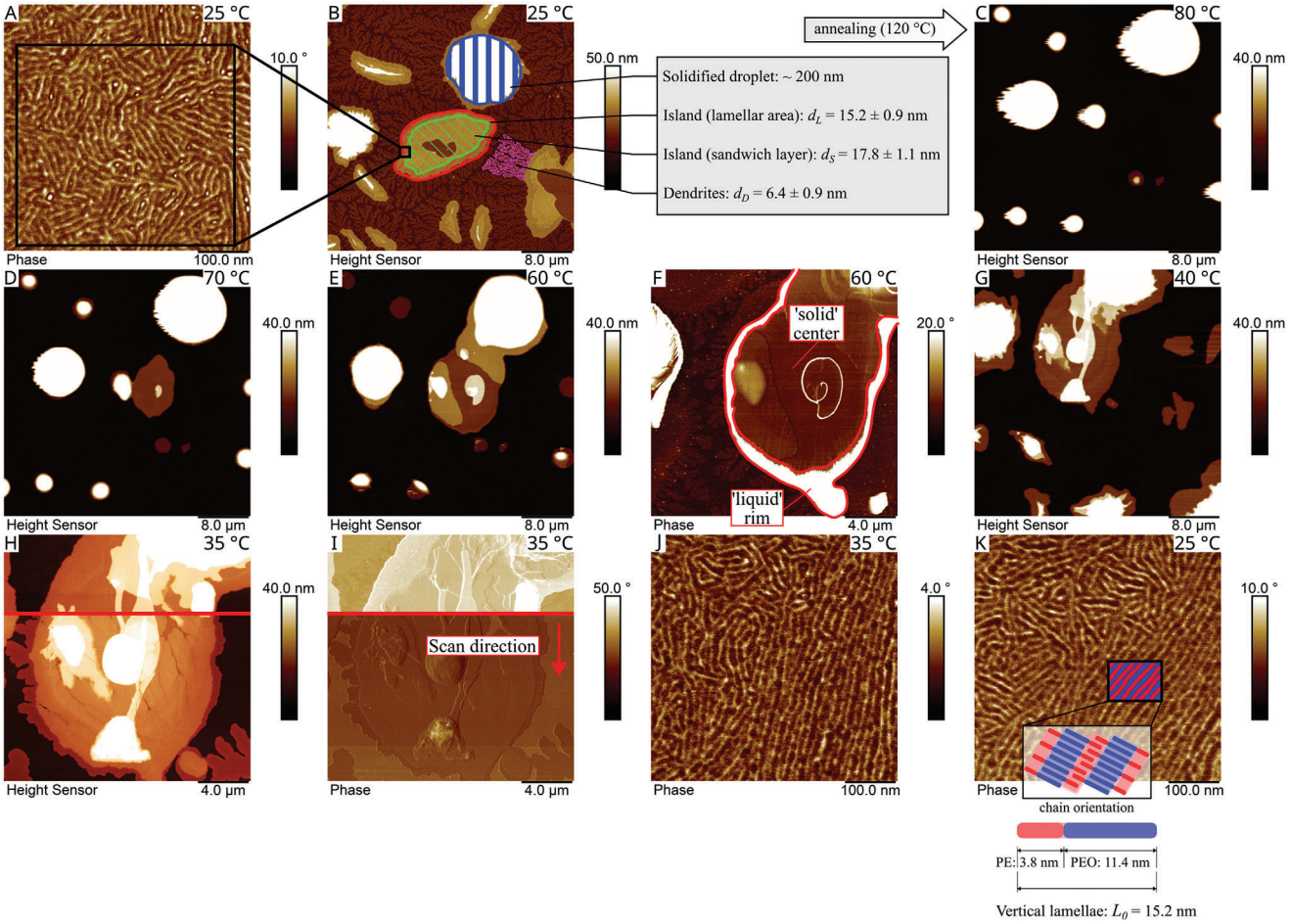


**Figure 1.** In situ AFM series of the annealed PE-b-PEO thin film. A) High-resolution AFM phase image of the vertical lamellar nanopattern after initial annealing. B) Overview AFM height image showing the sample morphology after initial thermal annealing on the AFM heating stage (heated at 120 °C for 5 min, then cooled with a rate of 2 °C $min^{-1}$ to 25 °C under nitrogen atmosphere). Each distinct feature can be associated with a discrete thickness. The vertical lamellae in (A) are found exclusively on the 15.2 ± 0.9 nm thick area of the island labeled "lamellar area'. Re-annealing at 120 °C leads to dewetting. The temperature was then stepwise reduced while the sample was continuously imaged. Topographically flat layers appeared starting at 80 °C C), and continued to grow laterally as temperature was decreased D-E,G). F) The lateral growth can be visualized in the AFM phase image, with the lateral growth front possessing a 'brighter' contrast. H–J) A fast (1–2 s) sudden transition at 35 °C yields the vertical lamellar nanopattern and various morphologies (dendrites, etc.). K) No reorganization of the lamellae is observed upon reaching 25 °C. The orientation of the PE-b-PEO chains within the lamellae is schematically shown in the inset, together with a sketch of the PE and PEO calculated extended chain block lengths.

"softer" rim of the layer. We assume that lateral growth consumes surrounding BCP chains in the substrate wetting layer and the droplets (see, e.g., Figure S3, Supporting Information). This explains how higher order 'full layers' ($n \bullet d_{ext}$) are often observed on islands near larger droplets.

At 35 °C a sudden transition occurs during the AFM scan. The phase contrast in Figure 1I significantly changes over two scanning lines, corresponding to a timeframe of seconds. While this transition does not change the specific film thicknesses as apparent from Figure 2, new non-integer layers are formed. In the height image in Figure 1H, cracks with 3–4 nm depth appear on the island with the discrete layers, and fingerlike dendrites with a thickness of 7.7 ± 2.7 nm spread from the island outward across the substrate. The high-resolution phase image recorded on an island after the transition (Figure 1J) reveals the formation of vertical lamellae. The mean width $L_0$ of the lamellae is determined to be 15.9 ± 2.4 nm at 35 °C, which corresponds to the calculated extended chain length $d_{ext}$ within the experimental error, and is also the same as the discrete layer thickness. The formed morphologies remain stable upon reaching room temperature, as seen for the vertical lamellae in Figure 1K, and do not experience any significant change in width ($L_0$ = 15.9 ± 1.0 nm).

As reported by Schulze et al. the as-cast, unannealed PE-b-PEO film forms discrete terraces of standing extended PE-b-PEO chains.[3] Since it is necessary to delete the thermal history of the sample for our in situ studies, the high chain mobility of the short chain BCP at elevated temperatures results in the formation of the larger droplets observed in Figure 1 and Figure S2 (Supporting Information). However, the dewetting is only partially irreversible. When cooling the system back to room temperature rewetting is observed, with new layers of standing extended chains forming. Compared to Zhang et al.'s cylindrical nanostructures which showed an improved parallel alignment along a growing dewetting front during continuous annealing, our

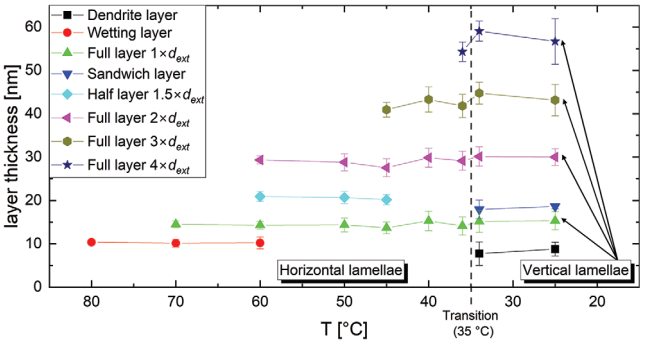


**Figure 2.** Temperature dependent film thickness of the discrete layers recorded during the in situ AFM series shown in Figure 1. With decreasing temperature, additional layers form on top of existing layers. Most of the layers' thicknesses agree with the calculated extended chain length, indicating standing PE-b-PEO chains (horizontal lamellar morphology). The transition at 35 °C observed in Figure 1 H triggers the reorientation of the horizontal lamellae to vertical lamellae while retaining the original film thickness of the full layers. Note that the vertical lamellae only appear on the full layers with thickness $n \bullet d_{ext}$, with $n$ being a discrete integer number.

PE-b-PEO standing chain layers first grow laterally at a sufficiently low temperature above 35 °C, consuming PE-b-PEO chains from the surrounding droplets and wetting layer.[35] A transition at 35 °C then triggers the vertical lamellae formation on layers with the extended chain thickness. Flow fields at the edge of the layers might locally enhance the lamellar ordering, but the dynamics cannot be resolved with our in situ AFM setup. We speculate that other morphologies (e.g., dendrites) may form depending on the crystallization kinetics, which will be discussed later.

### 2.2. Influence of Interfacial Energies

The orientation of domains in block copolymer thin films is highly dependent on the interfacial energies between the copolymer blocks and the substrate and the top surface, respectively.[1,5,36–38] The discrete layer thickness $L_0$ corresponding to $d_{ext}$ measured in Figure 2 indicates that the PE-b-PEO chains at higher temperatures are oriented vertical with respect to the substrate and are fully extended, which is confirmed by the featureless topography of the layers. Therefore, they form a microphase separated horizontal lamellar morphology that is stabilized over the temperature regime from 80 to 35 °C. Contrary, in the bulk, for similar asymmetric BCPs in the same temperature region, various morphologies have been reported.[15,34,39–41] For example, Bates et al. and Weiyu et al. independently observed several phase transitions in asymmetric bulk PE-b-PEO between lamellae, gyroid, cylinder, and spherical structures with temperature.[39,40] As temperature was increased, the lamellae transformed first into a gyroid and cylinder structure, which transformed into a spherical morphology at higher temperatures before disordering. The transitions were closely linked to the melting of the crystalline phases of the PEO and PE blocks.

The key difference from the bulk to the here analyzed, few $L_0$ thin films is that interfacial effects of the substrate and nitrogen atmosphere interface dominate the microphase evolution.[5] For the few $L_0$ thin PE-b-PEO BCP films, symmetric, asymmetric, and neutral wetting is distinguished depending on the wetting affinities of both copolymer blocks with the substrate.[3,37] Symmetric and asymmetric wetting both facilitate the formation of a horizontal lamellar morphology, while neutral wetting with a similar interfacial energy difference of both copolymer blocks to the substrate can induce the formation of vertical lamellae.[1,5,36,42] The M3M-functionalized silicon surface has been reported as 'neutral' substrate for PE-b-PEO before, since the water contact angle (76.5 ± 0.9°) lies between that of PE (100–110°) and PEO (0–10°).[3] It is known that the as-cast PE-b-PEO thin film on a M3M surface will assume a discrete thickness corresponding to the standing extended PE-b-PEO chain, where PE or PEO block may be oriented up or down. Lateral segregation of the standing extended PE-b-PEO chains takes place during drop-casting and leads to local domains with the PE and PEO chain end up and down, respectively, and their domain size is limited by the substrate affinity dependent chain mobility. The formation of perpendicular morphologies during thermal annealing ex situ was associated with a thermal barrier for the rotation of the PE-b-PEO chains.[3] Interestingly, we did not observe the formation of a perpendicular morphology in situ upon cooling down from 120 to 35 °C. Instead, the forming PE-b-PEO islands in Figure 1C–G at T = 80 to 35 °C assume a horizontal morphology consisting of standing extended chains, typical for asymmetrical wetting, and the perpendicular morphology only forms at a temperature as low as 35 °C.

In order to explain the asymmetric wetting at elevated temperatures, the interfacial energies between the M3M surface and both copolymer blocks have to be considered. The M3M surface energy can be calculated from contact angle measurements of M3M with, e.g., water and hexadecane using the OWRK method, yielding a surface energy of 34.4 mJ $m^{-2}$.[43] The details can be inferred from the (Figure S1 and Table S4, Supporting Information). While the M3M substrate surface energy is mostly temperature independent, the PE and PEO blocks both undergo melting and crystallization in the investigated temperature range.[34,39,44] In the melt state, the surface tensions of PE and PEO are mostly dependent on their mass density.[45] By using the Parachor introduced by Sudgen and reported temperature dependent molar volumes of PE and PEO homopolymer analogues (Table S1, Supporting Information), the surface tensions of the PE and PEO blocks in melt state can be estimated.[45–47] As our calculations in the SI show, the surface energies of PE and PEO change significantly upon crystallization ($\Delta\gamma$ between 10–15 mJ $m^{-2}$ for PE and PEO). Note that an extended chain lamellar crystal features two distinct surface facets with different surface energies, which can be extracted from reports of extended chain crystals of PE and PEO homopolymers.[25,48–51] The surface facets consist of the lateral crystal surface $\gamma_L$, and the chain-end or ciliated surface $\gamma'$. The surface energies and interfacial energies calculated with the Owens-Wendt formula in the Supporting Information are illustrated in **Figure 3**.[1,52]

The interfacial energy of the PEO block at the chain-end surface with the M3M surface at a temperature above the PEO crystallization (T > 35 °C) shown in Figure 3B is clearly lower than the M3M – PE interfacial energy and thus, the PEO favors exposure to the M3M surface. Consequently, the PE block wets the nitrogen interface, as it is the copolymer block with lower

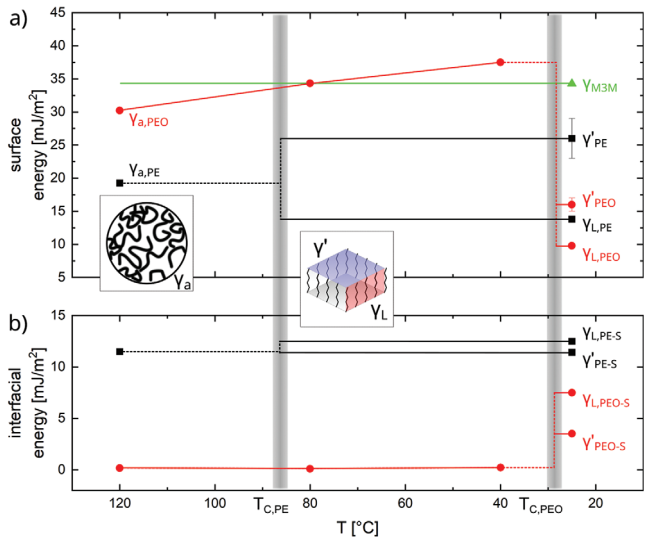


**Figure 3.** a) Schematic representation of the temperature dependent surface energy evolution of the PE (black), PEO (red), and M3M (green). Upon reaching the PE and PEO crystallization temperatures, the anisotropy of the forming extended chain polymer crystal leads to a distinction between the lower lateral crystal surface energy $\gamma_L$ and the higher 'cilia'.surface energy $\gamma'$. b) Interfacial energy between PE/PEO blocks including their different crystal surfaces and the M3M calculated using the Owens-Wendt formula. A higher interfacial energy indicates a less favorable interaction of the corresponding co-oligomer block with the M3M.

surface energy as seen in Figure 3A, and overall, leads to asymmetric wetting conditions and the horizontal lamellar morphology in the temperature range from 80 to 40 °C. However, this horizontal lamellar morphology is obviously disrupted at 35 °C as evident from the AFM images in Figure 1H,I. At T = 35 °C, PEO starts to crystallize, and simultaneously, vertical lamellae appear, see, e.g., Figure 1J.

### 2.3. Effect of Thin Film Crystallization

As described earlier and shown in Figure 1I, a morphological transition occurs at 35 °C. The vertical lamellae visible in Figure 1A appear on the outer area of the islands, e.g., in the region marked in red in Figure 1B, and also on all elevated layers which exhibit a thickness corresponding to $d_{ext}$, indicated as full layers in Figure 2. AFM height images of the vertical lamellae on the elevated layers correspond to Figure 1A and are therefore omitted here. Note that the full layers preserve their film thickness during the transition.

Earlier studies based on ex situ AFM concluded that the lamellae formation mechanism was associated with a thermal barrier for the PE-b-PEO chains and that the standing chains in the as-cast film rotated to form vertical lamellae at elevated temperatures.[3] Since both PE and PEO block may crystallize independently, we can distinguish between three different thermodynamic regimes: the disordered amorphous state (PE amorphous, PEO amorphous), the single-crystalline state (PE crystallized, PEO amorphous), and the double-crystalline state (PE crystallized, PEO crystallized).[34,39] The stark phase contrast change in Figure 1I and the simultaneous appearance of vertical lamellae clearly suggests that the formation of the vertical lamellar nanostructure is directly correlated to the PEO crystallization at 35 °C, rather than a thermally activated chain motion.

Copolymer blocks in BCP thin films can crystallize either flat-on (chains vertical to substrate) or edge-on (chains parallel to substrate), forming crystal lamellae of different orientations.[53] Obviously, the PE-b-PEO chains are oriented vertical in the temperature range from 80 to 40 °C and form a microphase separated lamellar morphology with vertical chains that is driven by the interfacial energy induced preferential exposure of PEO to the M3M surface as outlined above. However, at the transition where PEO starts to crystallize, the chains apparently rotate and form edge-on crystal lamellae by overwriting the microphase separated horizontal morphology despite the existing confinement imposed by the opposite copolymer block, referred to as breakout crystallization.[4,8,19]

The observed breakout crystallization requires that the confinement of the PEO by the crystalline PE block is weak, which seems reasonable to assume, since the PE block (16 ethylene units) is significantly shorter than the PEO block (41 ethylene oxide units). This has been demonstrated for different crystallizable systems, such as PS-b-PLLA, where by switching the crystallization temperature above or below the glass transition of the PS block, the PLLA could either crystallize as edge-on lamellae via breakout crystallization or stay confined in a horizontal geometry.[54]

The PEO crystallization in bulk PE-b-PEO has been reported to change the existing mesostructure from PE single-crystalline lamellae, cylinders, or gyroid to double-crystalline lamellae.[15,34,39,40] Simulations have demonstrated how surface-polymer chain affinity in thin films promotes a surface-assisted nucleation of oriented crystal lamellae.[27,55] While a high affinity between a chain and the surface lead to a reduced chain mobility, a decreased crystallization rate, and in turn, predominantly flat-on crystal lamellae, a low chain affinity with a surface conversely allowed for the formation of predominant edge-on crystals.

The M3M interfacial energy for the PEO block in Figure 3B indeed weakens upon crystallization, which enhances chain mobility and assists in the initial primary PEO nucleation. More importantly, the lateral crystal surface energies of the PE and PEO block, see Figure 3A, possess the lowest surface energy and will be preferably exposed to the nitrogen interface. Since primary PEO nucleation is restricted to the microphase separated horizontal lamellae and may be initiated anywhere in the PEO block, we conclude that the high chain mobility and the surface energy minimization during the proceeding PEO crystallization causes the chains to flip and form vertical lamellae of extended, double-crystalline PE-b-PEO chains. The nucleation may start as flat-on crystallization, but the forming lateral crystal surfaces will reorient the chains and overwrite the horizontal lamellar morphology in order to minimize the free surface energy.

### 2.4. Crystallization-Dependent Morphologies

The film shown in the overview AFM height image (Figure 1B) can be divided into three distinct morphologies. Besides the vertical lamellae (shown in red) located near the edge of the islands, a slightly thicker top layer, here referred to as "sandwich" layer

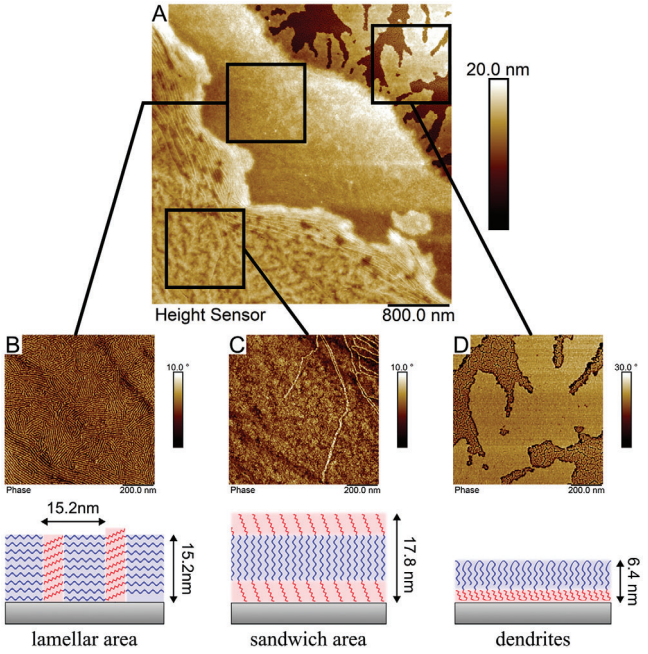


**Figure 4.** Overview of the final PE-b-PEO thin film morphologies at room temperature after annealing. A) Overview AFM height image and phase images with vertical lamellae region B), sandwich layer region C), and dendrite region D). Each layer has a different thickness stemming from the BCP chain orientation and stacking. The vertical lamellae consist of edge-on, extended chain crystal lamellae (B), while the sandwich (C) and dendrite (D) layers likely consist of flat-on folded-chain crystals.

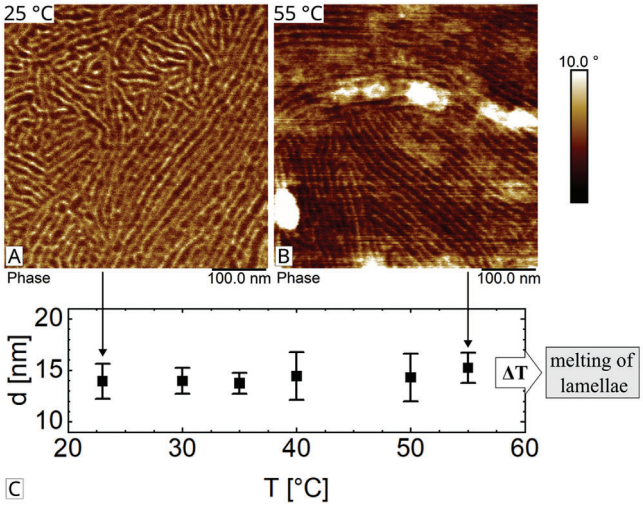


**Figure 5.** A) AFM phase image of the vertical lamellae at 25 °C and B) at 55 °C. C) Graph of the lamellar width with temperature, demonstrating the thermal stability of the vertical nanopattern up to its melting temperature above 55 °C. Above 55 °C, the lamellar pattern is lost due to melting, thus impeding small-scale, high-resolution AFM imaging.

(shown in green) is in the center of the islands. Finger-like dendrite structures extend from the edge of the islands outward and cover large parts of the bare substrate area (shown in purple). A comparison of the different morphologies, including their location on the thin film, and high-resolution AFM phase images is given in **Figure 4**.

The sandwich layer is featureless and has cracks reaching 3–4 nm down and a thickness of $d_S = 17.8 \pm 1.1$ nm, which is larger than the calculated fully extended chain length ($d_{ext} = 15.2$ nm). The featureless phase image in Figure 4C shows a lack of vertical nanostructures. The additional layer appears first at 35 °C and developed during PEO crystallization. Contrary to the outer region of the island, where the PEO crystallization creates vertical lamellae (Figure 4B) as described in section 2.3, the absence of surface features and the higher thickness indicate that in the central region the PEO crystallization proceeds in a different way. The confinement in the center of the island must be stronger than near the edge of the island and therefore inhibit chain rotation upon PEO crystallization. The sandwich layer probably consists of stacked folded chain crystal morphologies of flat-on oriented crystal lamellae. However, the origin and driving force to create such a chain arrangement is first of all not evident.

For semicrystalline PS-b-PCL and PS-b-PLLA thin films the crystallization was reported to initialize at the edge of islands and the formed crystallites grew inward, producing single edge-on crystals at the edge and on the adsorbed monolayer, which branched and coarsened during crystallization.[8,56] This resulted in the co-existence of multiple morphologies in the thin film.[8] For crystallizable BCPs, the chain stretching due to deformation during hole/island formation will initiate crystallization primarily at the boundaries of the holes or islands.[8]

It is reasonable to assume that the PEO crystallization in the PE-b-PEO thin film is also initiated at the edge of the island due to high chain mobility at the edge and then crystallizes inward.

However, in the center of the island the ability of the chains to rotate upon crystallization is hindered as a consequence of the lateral growth mechanism of the discrete layers above $T_{c,PEO}$ as highlighted in Figure 1F. The difference in phase contrast might indicate different chain mobilities, with BCP chains in the outer area of the island possessing higher mobility, although all chains in the island are confined to the horizontal lamellar morphology before PEO crystallization. Therefore, chain mobility in the horizontal lamellae during PEO crystallization plays a vital role in allowing chain rotation to form vertical lamellae.

The finger-like dendrite structures covering large parts of the bare substrate area in Figure 1B (marked in purple) are topographically featureless and form simultaneously with the sandwich and vertical lamellar morphology at 35 °C as seen in Figure 1H. The PE-b-PEO chains in the dendrites are probably oriented vertically, with the chains forming folded-chain flat-on crystals, since their discrete thickness of 6.4 ± 0.9 nm is smaller than the extended chain length (Figure 4D). They are not perfectly planar, as shown in the (Figure S4, Supporting Information), indicating that the PE-b-PEO chains in the dendrites undergo limited morphological changes during formation similar to relaxations found in thin films of crystalline PEO monolayers, leading to partial chain unfolding.[57] Their lateral structure is typical for surface diffusion-controlled growth, starting from the edges of the islands and growing outward. Chains in the wetting layer on the M3M surface will diffuse toward the forming growth front, where they will attach themselves to the crystal, thus changing their planar

arrangement toward a more vertical arrangement.[25,57] The depletion of chains in the wetting layer will then lead to the finger-like growth.

For low molecular weight PEO fractions with lengths as short as ≈6 nm, once-folded chain crystals were reported to crystallize at high undercoolings by Godovsky et al., while at small undercoolings the short-chain PEO oligomers preferably formed extended chain crystals.[50]

Although short-chain block co-oligomers prefer an extended conformation, they may form a folded-chain crystal instead of an extended chain crystal at sufficiently high undercoolings. High undercooling can also be understood as fast crystallization, limiting chain reorganization, or in this case, chain unfolding. As observed by the fast topographical transition in Figure 1H over 1–2 lines (corresponding to a timeframe of 1–2 s), the PEO crystallization proceeds very quickly, therefore promoting the formation of dendrites on the bare substrate area as folded-chain flat-on crystals.

Summarizing, our results suggests that the PE-b-PEO chains in both sandwich and dendrite morphology are vertically oriented with respect to the M3M surface and consist of folded chain crystals. They and the vertical lamellae form simultaneously upon PEO crystallization via different crystallization pathways, depending on the mobility of the chains and their orientation in the wetting layer or in the single-crystalline horizontal lamellae.

Since short-chain co-oligomers favor an extended conformation, we hypothesize that the extended chain lamellae are more stable than the arrangement in the sandwich and dendrite layers. We therefore investigated the melting of the vertical lamellae and the melting of the sandwich and dendrite morphologies, see, e.g., **Figures 5** and S2 (Supporting Information), respectively. As the temperature increased, the dendrite and sandwich structures began to exhibit some lateral segregation at 45 °C, as illustrated in the AFM height image in Figure S2E (Supporting Information). Further increase of the temperature to 50 °C as shown in Figure S2F (Supporting Information) lead to complete melting of the dendrites, and the sandwich layer thickness decreased to the extended chain length and formed a topographically flat surface in the center of the island. On the other hand, the vertical lamellae in Figure 5 remained stable and disappeared only above 55 °C, the melting temperature of the PEO block.[3] This proves that the folded-chain sandwich and dendrite morphologies are as expected less thermally stable than the fully extended chain crystals of the vertical lamellae.

Folded-chain crystals are known to be less thermodynamically favored than their extended chain counterpart. Reiter et al. used kinetic control of the PEO crystallization in a PB-b-PEO BCP to study the folding and unfolding of chains at different crystallization temperatures.[11] The folded-chain crystal lamellae formed under kinetic control at high undercoolings transformed into their thermodynamic stable extended-chain lamellar state by thermal annealing below $T_{m,PEO}$. With this transition, the orientation of the lamellae changed from vertical to horizontal. Compared to kinetically crystallized vertical nanostructures our results highlight the thermodynamic stability of vertical lamellae of extended, short-chain PE-b-PEO crystals and clearly demonstrates the advantageous stability and homogenous feature size this BCP systems has over other crystallizable BCP.

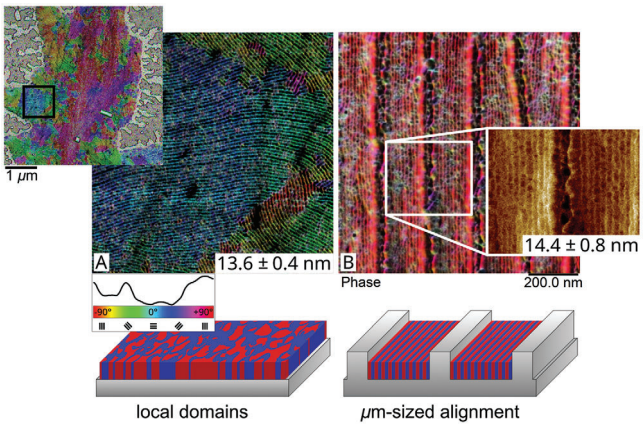


**Figure 6.** AFM phase images of lamellar nanostructures of PE-b-PEO on planar (no DSA) and structured (with DSA) substrates. A) Vertical nanopattern on planar substrate, showing local alignment. The color scale refers to the orientation of the domains (a schematic graph of the orientation distribution is shown above the color scale, showing preferential alignment for specific directions on the island), the top left shows a 5 × 5 µm overview. B) Aligned BCP along DSA trench pattern (150 nm trench width) with inset, demonstrating the macroscopic, long-range alignment, here over several µm. The images clearly show how the alignment is improved over the whole image compared to the case without DSA. The DSA has no influence on the width $L_0$ of the vertical lamellae.

### 2.5. Directed Self-Assembly

The macroscopic alignment of the lamellar nanopattern using trench pattern was investigated. **Figure 6B** depicts the PE-b-PEO lamellae aligned along the trench direction of a 150 nm wide and 50 nm deep periodic trench pattern. The polymer processing to create the nanostructured thin PE-b-PEO film was kept the same as for the plane, chemically modified Si surfaces. In order to compare the effect of the DSA on the nanolamellae orientation, Figure 6A depicts AFM phase images of PE-b-PEO lamellae recorded on unstructured planar substrates. The colormap in Figure 6 indicates the orientation of the lamellae which was determined with OrientationJ, a plugin for ImageJ image processing software.[58] The lamellar thickness $L_0$ remained the same independent of the DSA.

BCP thin film self-assembly on a planar substrate inevitably leads to the formation of local domains of different lateral-oriented nanopatterns with numerous defect structures, thus limiting their use in applications.[20] In order to be used in nanotechnology, the BCP nanopattern self-assembly must be guided into the desired long-range order, orientation, and morphology.[21] Different approaches for DSA include utilizing external fields (shear, electrical), chemically patterned substrates (chemoepitaxy), or topographic guiding patterns (graphoepitaxy).[20,21,30,59–61]

Here we show that our double-crystalline PE-b-PEO BCP can be macroscopically aligned as a first required step toward nanofabrication. Our electron beam lithography-fabricated (EBL), hydrogen silsesquioxane-based (HSQ) trench patterns were uniformly functionalized with M3M, providing neutral wetting affinity for the BCP at the bottom and sides of the trenches. As shown in Figure 6B, the vertical lamellae align along the

direction of the trench length, forming an ordered array of vertical nanostructures over a range of several µm. In comparison, the vertical lamellae on the unstructured substrate in Figure 6A show local alignment of varying degree in small domains. Several bridge-like features observed in Figure 6 are likely the result of singular defects and branching of the vertical lamellae. They may be caused by incomplete breakout crystallization during formation of the vertical lamellae, indicating lower local crystallinity. We speculate that the defect density could be reduced by decreasing the trench height of the guiding lines. Likely, the bridge-like features are also partially induced by AFM tip-related issues from the challenging imaging inside the trenches.

Although improved local domain order with lamellae highly oriented along the direction of the edge of the film could be observed, the vertical lamellae on the unstructured substrate have a heterogeneous morphology, making them undesirable for nanofabrication. The local alignment on the unstructured substrate stems from a dewetting process at the three-phase contact line between air, substrate, and BCP film.[11] A flow field provided by diffusion of the BCP chains can locally order the BCP nanostructures.[35] However, BCP-based applications require macroscopic alignment of the vertical lamellae and direct control over their orientation.

To our knowledge, this is the first report that demonstrates the macroscopic alignment of a double-crystalline PE-b-PEO BCP with graphoepitaxy based DSA. Further studies are necessary to elucidate how the PE-b-PEO pattern of macroscopically aligned vertical lamellae can be subsequently processed.

Typical processing steps include the selective (metal)-ion infiltration of a copolymer block (e.g., sequential infiltration synthesis), followed by a pattern transfer step through etching.[62,63] Ghoshal et al. have demonstrated the processability of a polystyrene-b-polyethylene oxide BCP. By selective metal ion infiltration of the PEO block and subsequent processing, large scale silicon and iron oxide nanowire arrays were produced by an etch step, utilizing the infiltrated BCP as a mask.[2,63,64] In principle, this methodology could be employed using PE-b-PEO as an promising BCP candidate for nanofabrication.

## 3. Conclusion

We have investigated the formation of vertical surface nanostructures and the role of crystallization in thin films of a short chain, double-crystalline PE-b-PEO block copolymer. At elevated temperatures, the PE-b-PEO forms thin films of horizontal lamellae with PE at the nitrogen interface and PEO wetting the M3M substrate interface due to interfacial effects. Upon PEO crystallization, the BCP transforms from horizontal to vertical lamellae by chain rotation. The chain rotation is the result of surface energy minimization promoting the exposure of the lateral crystal surface to the nitrogen interface, leading to edge-on growth of crystal lamellae. The vertical lamellae were shown to be thermodynamically more stable compared to other morphologies found in the film. The other morphologies formed in regions with lower chain mobility, which mainly lead to flat-on crystallization of folded chains. The thermodynamic stability of the vertical nanopattern due to the extended chain conformation, together with the exact lamellar thickness corresponding to the extended chain length, offers a clear advantage over vertical nanopattern produced via non-crystalline BCPs or via kinetically controlled crystallization (with, e.g., folded chain crystals).

Additionally, the domain structures of the vertical nanopattern were shown to locally align along the dewetting borders of the film, likely due to internal stress fields and preferential nucleation at the three-phase-contact line. Trench guiding patterns could align the lamellar domains macroscopically, demonstrating the feasibility of short-chain PE-b-PEO based surface structures and providing a first step toward future fabrication of functional nanodevices.

## 4. Experimental Section

*Materials*: Polyethylene-block-poly(ethylene oxide) with a nominal average molar mass of 2250 g $mol^{-1}$ and 80 wt.% PEO was purchased from VWR International. Methyl 3-mercaptopropionate (M3M, 98% purity) was purchased from Thermo Fischer Scientific. Ethanol (absolute) was purchased from Sigma-Aldrich and acetone was purchased from VWR International. The block lengths and theoretical extended total chain length were calculated using the molar mass and PEO weight percentage as shown in the Supporting Information. Estimation of the Flory–Huggins interaction parameter $\chi$ via Hildebrand solubility parameters $\delta_H$ is also shown in the Supporting Information.

*Substrate Preparation*: A silicon wafer was cut in 1 × 1 $cm^2$ pieces and sonicated in acetone, ethanol, and ultrapure water, then dried with compressed nitrogen. A 5 nm gold film was deposited on the substrate via sputter coating. The substrate was then rinsed with ethanol, dried with compressed nitrogen, and subsequently cleaned in argon plasma for 5 min. For surface modification with self-assembled monolayers, the substrate was immersed in a 5 mM solution of methyl 3-mercaptopropionate in ethanol for 2 h and afterward rinsed with ethanol, dried with compressed nitrogen, and stored in vacuum at 80 °C for 1 h. The same surface modification was also applied to the guiding patterns fabricated by electron beam lithography for directed self-assembly described below.

*DSA Pattern Fabrication via Electron Beam Lithography (EBL)*: Trench patterns suitable for guiding the self-assembly of the PE-b-PEO were fabricated via EBL at Paul Scherrer Institute (PSI), Switzerland. A silicon chip (1 × 1 $cm^2$) was cleaned in $O_2$ plasma for 60 s. After pre-baking at 125 °C, the chip was spin-coated with hydrogen silsesquioxane (HSQ) resist (2% XR1541, Dow Corning) at 3000 rpm with 1000 rpm $s^{-1}$ acceleration for 60 s. EBL was performed with a Vistec EBPG 5000+ using a 100 kV electron beam, 1 nA beam current, and 300 µm aperture. The exposure dose was varied from 9000 to 14500 µC $cm^{-2}$. After exposure, the patterns were developed in a 1:3 solution of Microposit 351 and water for 60 s. The pattern was then sputter coated with 10 nm Au. The total height of the trench pattern was ≈50–70 nm, with a line thickness of ≈30–50 nm, and varying trench sizes (50, 100, 150 nm). The trench patterns were written in separated 100 × 100 µm sized squares for each dose and trench size.

*Thin Film Preparation*: Thin films of PE-b-PEO block copolymer were prepared by drop casting a 0.1 wt.% PE-b-PEO solution in ethanol on the M3M modified substrates. To induce the formation of perpendicular nanostructures, the BCP films were thermally annealed with the heating stage of the AFM in dry nitrogen atmosphere by heating at 120 °C for 5 min and subsequently cooling to room temperature at a constant rate of 2 °C $min^{-1}$.

*In situ AFM Investigation*: The annealed films were investigated with a Dimension Icon AFM (Bruker) with an integrated heating stage.[65] For the in situ measurements, RTESP-150 cantilever (Bruker) without a reflective coating was used to avoid bimetallic bending effects during heating, and the cantilever was kept at the same temperature as the sample on the heating stage. The sample was placed on a heating stage and was continuously imaged while the temperature was slowly changed. When necessary, the cantilever tip was withdrawn and the laser was realigned due to the heat induced bending. The sample was imaged under constant $N_2$ flow

(30 ccm $min^{-1}$). The tip heater was switched in automatic mode. For the in situ study, the film was slowly heated in 5 °C steps until 120 °C was reached, and the AFM image was recorded every 10 °C steps after the image stabilized. The same procedure was applied when cooling the sample down to room temperature. For high resolution scan sizes (< 5 × 5 µm) at elevated temperature, the AFM tip induced the formation of larger agglomerates on the BCP film.

For the analysis of the layer thickness, the AFM height images were processed by masking the island regions and subsequent plane fitting or flattening of the blank substrate area. The thickness of each layer was determined by the height distribution in the height images and confirmed with individual line profiles.

## Supporting Information

Supporting Information is available from the Wiley Online Library or from the author.

## Acknowledgements

The authors thank Arti Dangwal Pandey and Bojan Bosnjak, DESY, for supporting the EBL preparation of the DSA templates and Arno Jeromin, DESY, for support in microscopy. The work has received support from the EU H2020 framework program for research and innovation under grant no. 101007417 Nano-science Foundries and Fine Analysis (NFFA-Europe-Pilot). A. Meinhardt, T. F. Keller acknowledge support by the Helmholtz Foundation through the Helmholtz-Lund International Graduate School (HELIOS, HIRS-0018). I. Maximov acknowledges financial support by NanoLund.

Open access funding enabled and organized by Projekt DEAL.

## Conflict of Interest

The authors declare no conflict of interest.

## Data Availability Statement

The data that support the findings of this study are openly available in [Zenodo] at [https://doi.org/10.5281/zenodo.14202741], reference number [14202741].

## Keywords

crystallization, diblock copolymer, directed self-assembly, extended chain, in situ AFM, vertical nanostructure

Received: August 9, 2024
Revised: January 27, 2025
Published online:

[1] K. Brassat, J. K. N. Lindner, *Adv. Mater. Interfaces.* **2020**, *7*, 1901565.
[2] C. Sinturel, F. S. Bates, M. A. Hillmyer, *ACS Macro Lett.* **2015**, *4*, 1044.
[3] R. Schulze, M. M. L. Arras, G. Li Destri, M. Gottschaldt, J. Bossert, U. S. Schubert, G. Marletta, K. D. Jandt, T. F. Keller, *Macromolecules* **2012**, *45*, 4740.
[4] C. De Rosa, R. Di Girolamo, A. Malafronte, M. Scoti, G. Talarico, F. Auriemma, O. Ruiz de Ballesteros, *Polymer* **2020**, *196*, 122423.
[5] M. J. Fasolka, A. M. Mayes, *Annu. Rev. Mater. Res.* **2001**, *31*, 323.
[6] C. M. Bates, M. J. Maher, D. W. Janes, C. J. Ellison, C. G. Willson, *Macromolecules* **2014**, *47*, 2.
[7] J. N. Murphy, K. D. Harris, J. M. Buriak, *PLoS One* **2015**, *10*, e0133088.
[8] W. N. He, J. T. Xu, *Prog. Polym. Sci.* **2012**, *37*, 1350.
[9] R. Ma, X. Zhang, D. Sutherland, V. Bochenkov, S. Deng, *Int. J. Extrem. Manuf.* **2024**, *6*, 062004.
[10] Y. H. Chung, J. K. Oh, *Biosensors* **2024**, *14*, 542.
[11] G. Reiter, G. Castelein, P. Hoerner, G. Riess, A. Blumen, J. U. Sommer, *Phys. Rev. Lett.* **1999**, *83*, 3844.
[12] E. Matxinandiarena, A. Múgica, M. Zubitur, V. Ladelta, G. Zapsas, D. Cavallo, N. Hadjichristidis, A. J. Müller, *Polymers* **2021**, *13*, 3133.
[13] O. Dolynchuk, T. Thurn-Albrecht, *Macromol. Chem. Phys.* **2023**, *224*, 2200455.
[14] A. Cicolella, F. De Stefano, M. Scoti, G. Talarico, J. M. Eagan, G. W. Coates, R. Di Girolamo, C. De Rosa, *Macromolecules* **2024**, *57*, 2230.
[15] X. Zhang, R. Schulze, P. Zhang, C. Lüdecke, X. Zhang, Z. Su, K. D. Jandt, *Polymer* **2014**, *55*, 1893.
[16] S. Nakagawa, H. Marubayashi, S. Nojima, *Eur. Polym. J.* **2015**, *70*, 262.
[17] L. Sangroniz, B. Wang, Y. Su, G. Liu, D. Cavallo, D. Wang, A. J. Müller, *Prog. Polym. Sci.* **2021**, *115*, 101376.
[18] R. M. Michell, A. J. Müller, *Prog. Polym. Sci.* **2016**, *54–55*, 183.
[19] W. Xu, Y. Zheng, P. Pan, *J. Polym. Sci.* **2022**, *60*, 2136.
[20] M. Luo, T. H. Epps, *Macromolecules* **2013**, *46*, 7567.
[21] C. Pinto-Gómez, F. Pérez-Murano, J. Bausells, L. G. Villanueva, M. Fernández-Regúlez, *Polymers* **2020**, *12*, 2432.
[22] S. B. Darling, *Prog. Polym. Sci.* **2007**, *32*, 1152.
[23] D. Lu, V. A. Bobrin, *Biomacromolecules* **2024**, *25*, 7058.
[24] C. M. Papadakis, C. Darko, Z. Di, K. Troll, E. Metwalli, A. Timmann, G. Reiter, S. Förster, *Eur. Phys. J. E.* **2011**, *34*, 7.
[25] G. Reiter, G. Castelein, P. Hoerner, G. Riess, J. U. Sommer, G. Floudas, *Eur. Phys. J. E.* **2000**, *2*, 319.
[26] G. Reiter, G. Castelein, J. U. Sommer, *Macromol. Symp.* **2002**, *183*, 173.
[27] Y. Ming, T. Hao, Z. Zhou, S. Zhang, Y. Nie, *Cryst. Growth Des.* **2023**, *23*, 7653.
[28] D. Lin, H. Wei, J. Wei, J. Xu, C. Zhang, X. Wang, *Macromolecules* **2024**, *57*, 2801.
[29] R. V. Castillo, A. J. Müller, *Prog. Polym. Sci.* **2009**, *34*, 516.
[30] C. De Rosa, R. Di Girolamo, A. Cicolella, G. Talarico, M. Scoti, *Polymers* **2021**, *13*, 2589.
[31] H. Schmalz, V. Abetz, *Polymers.* **2022**, *14*, 696.
[32] L. Chu, W. J. B. Grouve, M. van Drongelen, E. G. de Vries, R. Akkerman, M. B. de Rooij, *Adv. Mater. Interfaces.* **2021**, *8*, 2001894.
[33] W. Cao, K. Tashiro, H. Masunaga, S. Sasaki, M. Takata, *J. Phys. Chem. B* **2009**, *113*, 8495.
[34] L. Sun, Y. Liu, L. Zhu, B. S. Hsiao, C. A. Avila-Orta, *Polymer* **2004**, *45*, 8181.
[35] H. Zhang, B. Wang, G. Wang, C. Shen, J. Chen, G. Reiter, B. Zhang, *Macromolecules* **2020**, *53*, 9631.
[36] L. Li, X. Jia, Q. Dong, J. Zhou, W. Li, *Macromolecules* **2023**, *56*, 5932.
[37] M. J. Fasolka, P. Banerjee, A. M. Mayes, G. Pickett, A. C. Balazs, *Macromolecules* **2000**, *33*, 5702.
[38] X. Chevalier, G. Pound-Lana, C. G. Correia, S. Cavalaglio, B. Cabannes-Boué, F. Restagno, G. Miquelard-Garnier, S. Roland, C. Navarro, G. Fleury, M. Zelsmann, *Nanotechnology* **2023**, *34*, 175602.
[39] M. A. Hillmyer, F. S. Bates, *Macromol. Symp.* **1997**, *117*, 121.
[40] C. Weiyu, K. Tashiro, M. Hanesaka, S. Takeda, H. Masunaga, S. Sasaki, M. Takata, *J. Phys. Conf. Ser.* **2009**, *184*, 012003.
[41] R. V. Castillo, M. L. Arnal, A. J. Müller, I. W. Hamley, V. Castelletto, H. Schmalz, V. Abetz, *Macromolecules* **2008**, *41*, 879.
[42] J. N. L. Albert, T. H. Epps, *Mater. Today* **2010**, *13*, 24.
[43] C. D. Bain, E. B. Troughton, Y. T. Tao, J. Evall, G. M. Whitesides, R. G. Nuzzo, *J. Am. Chem. Soc.* **1989**, *111*, 321.

[44] J. P. Yang, Q. Liao, J. J. Zhou, X. Jiang, X. H. Wang, Y. Zhang, S. D. Jiang, S. K. Yan, L. Li, *Macromolecules* **2011**, *44*, 3511.
[45] D. W. Van Krevelen, K. Te Nijenhuis, *Properties of Polymers*, 4th ed., Elsevier, Amsterdam **2009**.
[46] S. Sugden, *J. Chem. Soc., Trans.* **1924**, *125*, 1177.
[47] G. T. Dee, T. Ougizawa, D. J. Walsh, *Polymer.* **1992**, *33*, 3462.
[48] J. D. Hoffman, *Polymer* **1991**, *32*, 2828.
[49] J. D. Hoffman, R. L. Miller, *Polymer* **1997**, *38*, 3151.
[50] Y. K. Godovsky, G. L. Slonimsky, N. M. Garbar, *J. Polym. Sci. Part C Polym. Symp.* **1972**, *38*, 1.
[51] P. C. Hiemenz, T. P. Lodge, *Polymer Chemistry*, 2nd ed., CRC Press, Boca Raton, FL **2007**.
[52] D. K. Owens, R. C. Wendt, *J. Appl. Polym. Sci.* **1969**, *13*, 1741.
[53] W. Hu, D. Frenkel, *Faraday Discuss.* **2005**, *128*, 253.
[54] J. Fu, Y. Wei, L. Xue, B. Luan, C. Pan, B. Li, Y. Han, *Polymer.* **2009**, *50*, 1588.
[55] Y. Ma, W. Hu, G. Reiter, *Macromolecules* **2006**, *39*, 5159.
[56] F. Zhang, Y. Chen, H. Huang, Z. Hu, T. He, *Langmuir* **2003**, *19*, 5563.
[57] G. Reiter, J. U. Sommer, *J. Chem. Phys.* **2000**, *112*, 4376.
[58] Z. Püspöki, M. Storath, D. Sage, M. Unser, In *Focus Bio-Image Informatics*, (Eds.: W. H. De Vos, S. Munck, J.-P. Timmermans), Springer International Publishing, Cham **2016**, pp. 69.
[59] P. W. Majewski, K. G. Yager, *J. Phys. Condens. Matter* **2016**, *28*, 403002.
[60] J. Zhang, X. Yu, P. Yang, J. Peng, C. Luo, W. Huang, Y. Han, *Macromol. Rapid Commun.* **2010**, *31*, 591.
[61] C. Park, J. Yoon, E. L. Thomas, *Polymer* **2003**, *44*, 6725.
[62] L. Wilson, International Technology Roadmap for Semiconductors (ITRS), *Semiconductor Industry Association* **2013**, 1.
[63] A. Löfstrand, A. Vorobiev, M. Mumtaz, R. Borsali, I. Maximov, *Polymers* **2022**, *14*, 654.
[64] T. Ghoshal, C. Ntaras, J. O'Connell, M. T. Shaw, J. D. Holmes, A. Avgeropoulos, M. A. Morris, *Nanoscale* **2016**, *8*, 2177.
[65] A. Stierle, T. F. Keller, H. Noei, V. Vonk, R. Roehlsberger, *J. large-scale Res. Facil. JLSRF* **2016**, *2*, A76.

## 5.3. Addendum to Discussion

### 5.3.1. Surface Energies and Crystal Orientations of PE-b-PEO thin film

In thin films of double-crystalline, extended-chain BCPs, the orientation of the double-crystalline lamellae on the substrate can be either flat-on or edge-on. Here, we do not consider the possible chain tilt that some copolymer chains in lamellar crystals may have, but instead focus only on the orientation of the entire double-crystalline lamellae. Due to the two asymmetric interfaces (free interface and substrate interface, see Tab. 5.3.1), the total surface energy will differ for each orientation. Thermodynamically, the orientation with lower total surface energy will be preferred.

***Tab. 5.3.1:*** Lateral $\sigma^l$ and cilia crystal surface energies $\sigma'$ of the extended chain PE and PEO blocks, as well as the interfacial energies with the methyl-3-mercaptopropionate (M3M)-functionalized substrate at room temperature. Reproduced from[67].

| | PE [mJ/m$^2$] | PEO [mJ/m$^2$] |
|---|---|---|
| $\sigma^l$ | 13.8 | 9.8 |
| $\sigma'$ | 26.0 | 16.0 |
| $\sigma^l_{Block-M3M}$ | 12.5 | 7.5 |
| $\sigma'_{Block-M3M}$ | 11.4 | 3.5 |

In flat-on orientation, the PE would be exposed to the air, while the PEO wets the substrate. This yields for the total surface energy of PE-*b*-PEO normalized to the area $A$ of the thin film:

$$\frac{\sigma_{tot,flat-on}}{A} = \sigma'_{PE} + \sigma'_{PEO-M3M} = 29.5 \text{ mJ/m}^2 \tag{5.3.1}$$

In edge-on orientation, which corresponds to the vertical lamellae, both the PEs and PEO block are exposed to the air and substrate interface. The exposed surface area of each block is given by the relative lengths of the extended chains (0.25 for PE and 0.75 for PEO) in edge-on orientation. This yields for the area-normalized total surface energy:

$$\frac{\sigma_{tot,edge-on}}{A} = 0.25(\sigma^l_{PE} + \sigma^l_{PE-M3M}) + 0.75(\sigma^l_{PEO} + \sigma^l_{PEO-M3M}) = 19.55 \text{ mJ/m}^2 \tag{5.3.2}$$

Direct comparison of the surface energies in flat-on and edge-on orientation of extended, double-crystalline PE-*b*-PEO proves that the vertical/edge-on lamellae formation is a direct result of the minimization of surface energies. The surface energy drives the reorientation from horizontal lamellae to vertical lamellae during break-out crystallization.

### 5.3.2. Thermodynamics: Crystallization or Microphase Separation

From the AFM results it is apparent that the PEO crystallization causes the formation of the vertical lamellae. However, the crystallization has to overcome the microphase separation. The initially formed, microphase separated horizontal lamellae form due to asymmetric wetting conditions at the substrate and free interface. In a strongly segregated BCP, the PEO crystallization would proceed mostly confined to the horizontal PEO microdomains, whereas crystallization in weakly segregated BCPs could overwrite the microphase separated morphology.[43]

For highly crystalline PEO, the enthalpy of melting $\Delta H_m = 8.6$ kJ/mol and entropy of melting $\Delta S_m = 25.1$ J/K mol is known.[1] The enthalpy and entropy of crystallization describe the reverse process. Therefore, with Eq. 2.2.1, the Gibbs free energy of PEO crystallization at 35 °C is calculated as:

$$\Delta G_c = \Delta H_c - T\Delta S_c = -869 \text{ J/mol} \tag{5.3.3}$$

In a thermodynamic sense, extended chain crystals are the most thermodynamic stable crystal state, where each polymer chain is densely packed in the crystal lattice, thus maximizing intermolecular forces. In effect, the entropy is minimal, since only a single extended chain conformation exists. Since the enthalpy and entropy are given for a regular, highly crystalline PEO homopolymer, not for a short-chain PEO extended chain crystal, it is reasonable to assume that the Gibbs free energy of crystallization is higher than the one calculated above.

The Gibbs free energy of mixing in Eq. 2.4.10 can be used to quantify the strength of microphase separation at the point of PEO crystallization. With the polymerization degrees of the PE and PEO blocks $r_{PE} = 16$, $r_{PEO} = 41$, the volume fractions $\phi_{PE} = 0.25$, $\phi_{PE} = 0.75$, and Flory-Huggins interaction parameter $\chi = 0.125$ calculated from the solubility parameters for 35 °C, the Gibbs free energy of mixing is calculated as:

$$\Delta G_{mix} = NkT(\frac{\phi_1}{r_1}\ln\phi_1 + \frac{\phi_2}{r_2}\ln\phi_2 + \chi\phi_1\phi_2) = -8.9 \text{ J/mol} \tag{5.3.4}$$

The negative $\Delta G_{mix}$ is surprising, since it basically implies favorable mixing conditions for the PE-*b*-PEO, which is not observed experimentally at 35 °C. However, it has been noted by Miquelard-Garnier et al. that the calculation of $\chi$ via solubility parameters can yield significant deviations compared to experimental measurements.[68] The simple mean-field lattice model of Flory and Huggins does not account for the complex behavior of polymer blends and block copolymers, and the values for molar volumes, solubility parameters, etc. used during the calculation of $\chi$ may give rise to large uncertainties up to a factor of ten.[68]

On the other hand, the calculation of $\chi$ provides an estimate for our observations. The last term in the above equation describes the enthalpy of mixing. Based on the different chemical moieties of PE and PEO, $\chi$ should probably be larger than calculated, leading to a higher (positive) enthalpic driving force for demixing. This in turn could yield a positive $\Delta G_{mix}$, implying segregation. However, the first two terms in the equation contribute to the entropy of mixing of a binary polymer blend or BCP. Generally, entropy describes the disorder of a system. For long chain BCPs, the mixing entropy scales inversely with the degree of polymerization $r$, i.e. block length. The low entropy of long chain BCPs favors demixing, while short chain BCPs have a higher (negative) entropic contribution to the Gibbs free energy of mixing. This exemplifies the issue of low $N$ BCPs, where the increased entropic tendency for mixing needs to be compensated with a higher enthalpic penalty for mixing (high $\chi$).

Despite the weak driving force for demixing, microphase separated horizontal lamellar morphologies have been observed by us in PE-*b*-PEO thin films at temperatures up to 80 °C (see, e.g., Section 5.2.). The interfacial energies in the thin film morphology and the PE block crystallization might additionally stabilize the morphology before PEO crystallization.

Comparing the Gibbs free energy of crystallization and mixing, it becomes clear that the PEO crystallization is the thermodynamic stronger driving force. Therefore, the breakout crystallization dominates the morphology upon PEO crystallization, leading to the formation of vertical lamellae. The kinetics of crystallization, however, will determine if other, less stable crystalline morphologies will form (e.g., sandwich and dendrite morphologies).

### 5.3.3. PEO Crystallization Dynamics with FastScan AFM

**Experimental.** A PE-*b*-PEO thin film sample was thermally annealed on the AFM heating stage under dry nitrogen atmosphere by heating to 120 °C for 5 min.

Then the temperature was reduced to 38 °C and the sample was imaged with AFM in tapping mode at a fast scan rate (cantilever: Fastscan-C, Bruker). Scan parameters, such as amplitude setpoint, drive amplitude, and gains had to be adjusted. A scan rate of 10 Hz offered a good compromise between topographical resolution and noise. The temperature was reduced with a rate of 1 °C/h until the PEO crystallization was observed at 31 °C, while the sample was continuously scanned (52 s per image).

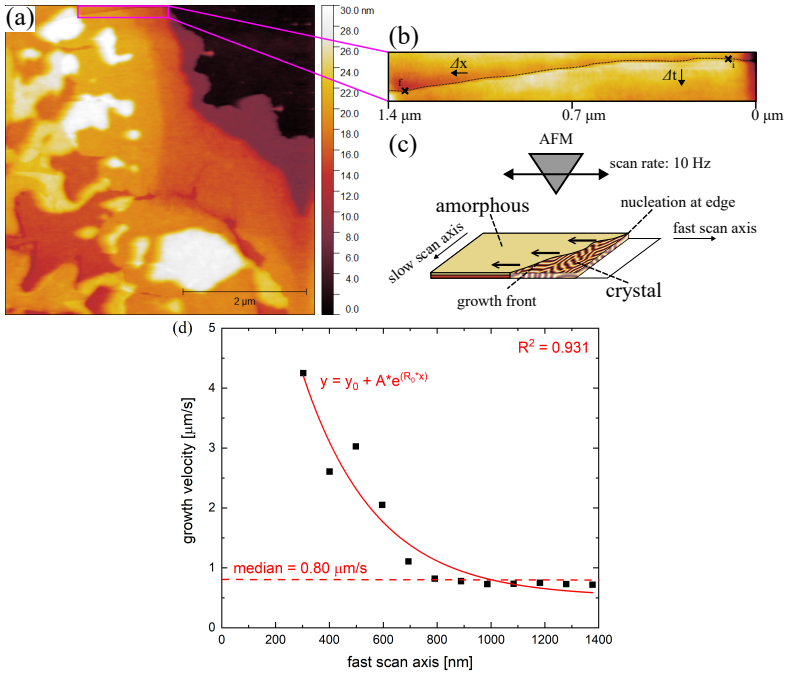


***Fig. 5.3.1.*** Illustration of the FastScan AFM measurements. (a) AFM height image (5 × 5 $\mu$m) of PE-*b*-PEO thin film at 31 °C. The market line in the inset (b) is the indicator for the position of the crystal growth front. (c) Schematic illustration of the sample and AFM tip. The crystallization front originates at the edge of the island area and proceeds inwards, while it transforms the horizontal, microphase-separated lamellar morphology into an edge-on, vertical crystal lamellar morphology. (d) Change of velocity of the crystallization as the growth front propagates through the island.

**Results and Discussion.** The AFM height image (5 × 5 $\mu$m) in Fig. 5.3.1 shows the change in topography during PEO crystallization at 31 °C. A small height change in the marked area in (a) and the inset in (b) can be observed, corresponding to the crystallization growth front. The breakout crystallization caused by the crystallization of PEO starts at the edge of the island structure and

proceeds inwards. In parallel, dendrites expand at the edge of the island structure and grow across the substrate. The process on the island area is schematically illustrated in (c). The AFM tip scans the surface at high scanning speeds, therefore overtaking the growth front. The crystallization velocity during the growth is shown in Fig. 5.3.1d. From the evolution of the growth front over time, and covered distance, the crystal growth velocity can be determined. The position of the growth front was determined from the fast scan axis, while the time was calculated from the number of passed lines along the slow scan axis. The crystallization proceeds fast in the beginning ($11.1 \pm 3.0$ $\mu$m/s) and then falls off to a constant value ($0.5 \pm 0.2$ $\mu$m/s) as it further grows into the island structure.

The decrease in velocity indicates a structural inhomogeneity of the film, limiting the rate, or changing the mechanism of PEO crystallization. The inhomogeneity could be related to the different morphologies that were observed in Section 5.2. on annealed PE-*b*-PEO thin films. Comparing vertical lamellae and sandwich morphologies, we argued that the thin film crystallization proceeds differently in the outer (lamellae) and inner (sandwich) parts of the island structure. In the central area of the island the chains were assumed to be less mobile, which leads to PEO crystallization under stronger confinement. It is reasonable to assume that the hindered chain mobility in the inner area prohibits breakout crystallization, effectively enforcing a different kinetic pathway for PEO crystallization in the inner area compared to the vertical lamellae in the outer area.

Additionally, the fast AFM measurements demonstrate that the dendritic growth on the substrate area is slow in comparison to crystallization in the island-shaped film. Although the following AFM scans which included the dendrite area were recorded $6 - 7$ min after the crystallization was completed, a lower limit for the dendrite growth velocity of $0.7 \pm 0.6$ nm/s can be determined. The slow crystallization growth confirms the diffusion-controlled crystallization mechanism of the dendrites in the thin thin wetting layer covering the substrate. The flat adsorbed chains in the wetting layer have to diffuse to the crystal growth front of the dendrites, where they raise up and form flat-on, folded chain crystals. While crystallization is responsible for improving chain order and achieving denser packing, the dendrite structures are not thermodynamic stable, unlike the vertical crystal lamellae, but instead kinetically induced.[37, 69]

The results are consistent with literature reports on the crystal growth velocity of single-crystalline BCP. Thin monolayers of polystyrene-b-polyethylene oxide films showed crystal growth rates from 0.001 to 1 $\mu$m/s, while exhibiting a finger-

like dendrite morphology.[70] Similarly, the growth velocity of breakout crystallization in films of microphase separated polybutadiene-block-poly$\epsilon$-caprolactone was determined to be 1.3 nm/s by Zhang et al.[71] In both examples the crystallization was observed to be diffusion controlled. For the dendrites of PE-*b*-PEO, this is also the case, as chains from the wetting layer on the substrate diffuse to the crystallization front of the dendrites. However, the breakout crystallization mechanism described in the PE-*b*-PEO islands proceeds not via diffusion, but by rotation of the chains to form vertical crystal lamellae. Consequently, this explains the high crystallization growth velocity.

## 5.4. Summary

In this section, a promising pathway for the formation of vertical surface nanostructures via crystallization control has been described. The chain lengths of the PE-*b*-PEO copolymer are in a size regime where conformational enthalpy prevails over entropy, and therefore, the thermodynamically favorable 'all-trans' conformation (extended chain) is adopted by the chains. Although crystallization is typically described as a kinetic process, the extended-chain crystallization of PE-*b*-PEO leads to a thermodynamically controlled morphology of double-crystalline, extended-chain lamellae. The interfacial energies during crystallization of the PEO block cause a 'breakout' of the originally microphase separated horizontal thin film, which results in the formation of vertical crystal lamellae. The pitch of the vertical surface nanostructures corresponds to the extended-chain lengths of the sub-10 nm copolymer blocks, thus offering a novel approach for the fabrication of defined, regular soft nanopatterns.

# 6. Solvent Vapor Annealing of Crystallizable Block Copolymer Thin Films

## 6.1. Introduction to Solvent Vapor Annealing

Heat treatment and annealing above $T_g$ (or $T_c$) of a block copolymer (BCP) is in most cases necessary to enable sufficient mobility for the morphology to rearrange into the phase-separated, equilibrium nanostructure and annihilate topological defects.[72, 73] However, this is accompanied by strong dewetting in the poly(ethylene)-*block*-poly(ethylene oxide) (PE-*b*-PEO) thin film, which is only in part reversible. Maintaining film homogeneity during annealing is a fundamental requirement for enabling bottom-up nanomanufacturing with PE-*b*-PEO, prior to implementing further processing or pattern transfer techniques (e.g., selective infiltration synthesis, selective etching, etc.).[74]

solvent vapor annealing (SVA) is used to anneal BCP thin films by exposing them to vapors of solvents at temperatures well below those typically used in thermal annealing (TA).[73] The solvent vapor swells the film, therefore promoting chain mobility and reorganization. Furthermore, the vapor influences the surface energy at the free surface of the film and with the substrate. For asymmetric wetting conditions in BCP thin films, selective solvents are needed to overcome the free surface preference for the lower surface tension block to produce well-ordered vertical nanostructures.[36] Additionally, solvent dissolved in the BCP effects the interaction between blocks ($\chi_{eff}$) and changes the volume fractions.[36]

For a neutral solvent, the effective interaction parameter $\chi_{eff}$ decreases proportional to the solvent intake:

$$\chi_{eff} \sim \chi(1 - \phi_s) \tag{6.1.1}$$

where $\phi_s$ is the solvent volume fraction and $\chi$ the interaction parameter between the copolymer blocks without solvent.[75] A neutral solvent swells both blocks equally, resulting in a downwards trajectory in the BCP phase diagram shown in Fig. 6.1.1. A change in $\chi_{eff}$ can lead to a morphological phase transition during swelling. For strong solvent intake, order-disorder transitions can be observed. The swelling of the film can be controlled by changing the relative saturation of the solvent vapor using temperature.[76]

In principle, the thermodynamic process is described by the Gibbs free energy of mixing (Eq. 2.4.1). For weakly polar polymer-solvent systems, regular solution

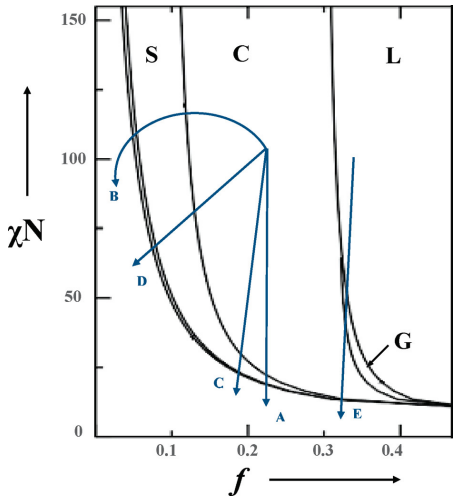


***Fig. 6.1.1.*** Schematic phase diagram showing the effect of swelling on a BCP in different solvent vapors. The trajectories/arrows represent swelling in different nonselective and selective solvents. Reproduced with permission from[77].

theory describes the thermodynamic equilibrium between solvent in the gas phase and in the polymer mixture.[75] The relationship between solvent vapor pressure and Flory–Huggins law is given by:

$$\ln\left(\frac{p}{p_{sat}}\right) = \chi_{ps}\phi_p^2 + \left(1 - \frac{V_{m,s}}{V_{m,p}}\right)\phi_p + \ln(1-\phi_p) \tag{6.1.2}$$

where $p/p_{sat}$ is the degree of saturation of solvent vapor pressure, $\phi_p$ is the polymer volume fraction, $V_{m,p}$ and $V_{m,s}$ are the molar volumes of the polymer and solvent, respectively, and $\chi_{ps}$ is the Flory-Huggins interaction parameter between the polymer and solvent.[75] The equilibrium vapor pressure $p_{sat}$ can be calculated from the empirical Antoine equation (Eq. 6.2.1), while the partial pressure of the solvent $p$ can be estimated from the ideal gas law $p = nRT/V$.[76]

The volume fraction in a film can be determined by the swelling ratio (SR = $d/d_0$) of the one-dimensional film swelling. Additionally, for typical polymer-solvent systems $V_{m,p} \gg V_{m,s}$.[75] This yields:

$$\ln\left(\frac{p}{p_{sat}}\right) = \chi_{ps}\left(\frac{d_0}{d}\right)^2 + \frac{d_0}{d} + \ln\left(1 - \frac{d_0}{d}\right) \tag{6.1.3}$$

Note that $\chi_{ps}$ changes with concentration of solvent in the polymer. Therefore, this relationship is linear only over a limited concentration range.[75] Monitoring and measuring the solvent vapor incorporation in the BCP film is critical for

understanding the phenomena involved in SVA.

While a neutral solvent swells both copolymer blocks equally, a selective solvent preferentially swells only one block. As a consequence, $\chi_{eff}$ might be increased, leading to stronger segregation of the blocks, and a diagonal trajectory in the phase diagram in Fig. 6.1.1, while enhancing chain mobility of the corresponding copolymer block. Furthermore, selective solvent swelling can improve structural parameters of the BCP film (e.g., line-edge roughness) relevant for BCP patterning applications.[75]

Another critical aspect is that SVA ordering and morphologies are strongly dependent on kinetic aspects, such as swelling rate, solvent removal rate, and sample history.[72, 73] Especially the solvent removal rate affects the film morphology, since the evaporating solvent introduces a concentration gradient in the film. The concentration of the BCP (equivalent to $\phi_p$) changes as a function of film depth and time, resulting in an upward trajectory in the phase diagram in Fig. 6.1.1 and consequently, microphase separation. The nucleation of the microphase is initiated at the free interface, where the solvent concentration is lowest, and the microphase grows into the film, following the solvent concentration gradient. The gradient acts as an ordering field and influences the relaxation of the BCP chains upon microphase separation. At high solvent removal rates, the concentration gradient is large and less reorganization of the BCP chains is possible. In contrast, low removal rates result in small gradients, and the BCP chains can adapt a thermodynamic stable morphology.[73] This has direct consequences for the ordering of, e.g., cylinder forming BCP, where the cylinders change orientation from vertical to horizontal when the solvent removal rate is varied from fast to slow.[72, 78]

### 6.1.1. Selective SVA and Crystallization

In combination with a crystallizable BCP system, understanding the effect of selective solvent SVA is not trivial.

For example, single-crystalline polystyrene-*block*-polyethylene oxide films exposed to cyclohexane were demonstrated to transition through several morphologies during SVA.[79] The initial flat-on single-crystal sandwich morphology, with polyethylene oxide (PEO) covered by polystyrene, was disrupted by the strong selective swelling of the polystyrene block. The strong swelling facilitated the formation of a dotted, microphase separated morphology. However, over long exposure times, the mobility of the PEO chains was increased by the solvent, leading to enhanced recrystallization as single crystals.[79] These reports demonstrate that

selective solvent vapor exposure may strongly effect the crystalline morphology and that solvent-swollen BCPs are dynamic systems.

With regard to our short-chain, double-crystalline PE-*b*-PEO system, (selective) swelling might enhance the ordering dynamics, thus reducing annealing time and temperature during SVA. This, in turn, could help retain film homogeneity during SVA, which is an important aspect for applications. Under high ethanol exposure, the selectivity of PEO and ethanol could, in theory, transform the PEO block into a mobile amorphous phase. The enhanced chain mobility would facilitate reorientation into a horizontal lamellar morphology, similar to the horizontal lamellae of the single-crystalline state (polyethylene (PE) crystalline, PEO amorphous) observed during TA. Alternatively, new microphase separated phases, which are inaccessible by pure TA in the PE-*b*-PEO thin film, could become attainable (e.g., cylinder, gyroid), given that the PE-*b*-PEO volume fractions are highly asymmetric. Over longer timescales, the ethanol could dissolve the PE block, leading to a disorder transition in the $\chi$ phase diagram, since ethanol is also used as solvent for the dissolution of PE-*b*-PEO during thin-film preparation.

## 6.2. Experimental SVA Section

### 6.2.1. Experimental Setup

The *in situ* Atomic Force Microscopy (AFM) setup with heating stage described in Section 5.2. was modified for imaging under solvent vapor atmosphere during SVA. The experimental setup, including a flow-through solvent reservoir and the AFM, is depicted in Fig. 6.2.1. A constant nitrogen stream flows through the unheated solvent reservoir, and the sample on the AFM heating stage is exposed to a regular flow of solvent-saturated atmosphere. The temperature of the sample is regulated and the sample topography during SVA is tracked *in situ* with AFM.

Thin films of PE-*b*-PEO on surface-modified (methyl-3-mercaptopropionate (M3M)) substrates were prepared as described in detail in the experimental part of Section 5.2.

The samples (I-VI) used during the SVA experiments are shown in Tab. 6.2.1. Pre-annealed refers to the standard thermal annealing procedure performed on the AFM heating stage at 120 °C under constant nitrogen flow. The gas flow of the ethanol-nitrogen mixture during all SVA experiments was between $20 - 30$ ccm/min. The samples were imaged in AFM tapping mode with a RTESP-150 type cantilever (Bruker).

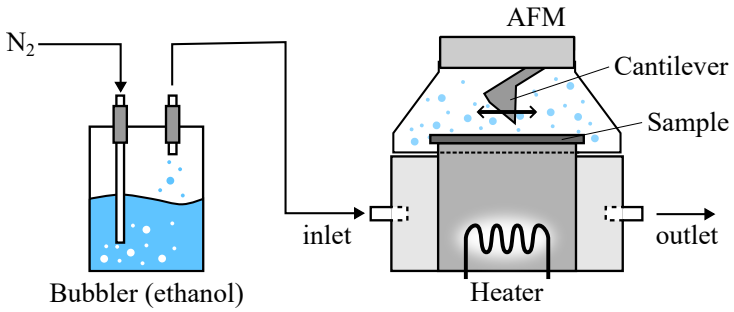


***Fig. 6.2.1.*** Sketch of the experimental SVA setup with bubbler and AFM. A nitrogen stream flows through the solvent reservoir (ethanol) and the sample is exposed to a continuous flow of ethanol saturated atmosphere. The sample is heated on the heating stage and the AFM tip is used to image the sample topography during SVA.

***Tab. 6.2.1:*** SVA samples overview.

| Sample | Initial condition | $T_{max}$ [°C] | Solvent |
|---|---|---|---|
| I | pre-annealed | 60 | ethanol |
| II | pre-annealed | 70 | ethanol |
| III | as-cast | 60 | ethanol |
| IV | as-cast | 70 | ethanol |
| V | as-cast | 70 | none ($N_2$) |
| VI | as-cast | 120 | ethanol |

Although controlling solvent evaporation is not possible in our 'constant-flow' setup, it would be of interest to investigate the effect the solvent removal rate has on the ordering, orientation, and crystallization of a solvent-swollen film.[80]

The experimental details for each sample[1] are given below:

I. The pre-annealed sample was stepwise heated under saturated solvent vapor and imaged with AFM. At each temperature step, a stable AFM image was recorded after waiting $5 - 10$ min. After reaching 60 °C, the temperature was stepwise reduced until room temperature.

I.a The sample was then thermally re-annealed by holding the sample at 120 °C for 5 min, followed by controlled cooling to room temperature with a rate of 2 °C/min. Subsequently, the re-annealed sample was heated to 60 °C under solvent vapor (heating rate: 2 °C/min) and held for 5 min before reducing

[1]The data supporting the findings of this study are available from the author upon reasonable request

the temperature (cooling rate: 1 °C/min) to 35 °C. The sample was then continuously imaged with AFM for 20 h at the same temperature.

I.b After 20 h at 35 °C, the temperature was slowly reduced until the contrast in the phase image changed at 31 °C (cooling rate: 1 °C/h).

II. The pre-annealed sample was heated to 70 °C under solvent vapor, and held at constant temperature for 1 h, before the temperature was stepwise reduced to room temperature while recording the sample topography with AFM.

III. The as-cast sample was stepwise heated to 60 °C under solvent vapor, and held at constant temperature for 1 h, before the temperature was stepwise reduced to room temperature while recording the sample topography with AFM.

IV. The as-cast sample was stepwise heated to 70 °C under solvent vapor, and held at constant temperature for 1 h, before the temperature was stepwise reduced to room temperature while recording the sample topography with AFM.

V. The as-cast sample was stepwise heated to 70 °C under nitrogen atmosphere, and held at constant temperature for 1 h, before the temperature was stepwise reduced to room temperature while recording the sample topography with AFM.

VI. The as-cast sample was heated to 120 °C under solvent vapor, and held at constant temperature for 5 min, before the temperature was reduced to room temperature (cooling rate: 2 °C/min). The sample topography was recorded afterwards with AFM.

### 6.2.2. Equilibrium Vapor Pressure

The equilibrium vapor pressure (or saturated vapor pressure) of ethanol in the SVA setup can be predicted from the semi-empirical Antoine-equation:[73, 76]

$$\log(p_{sat}) = A - \frac{B}{T + C} \tag{6.2.1}$$

with the saturated vapor pressure $p_{sat}$ in mmHg and temperature $T$ in °C. With the empirical parameters $A = 8.11576$, $B = 1595.76$, and $C = 226.5$ given by Kretschmer et al.[81], the saturated ethanol vapor pressure at 25 °C is 0.07865 bar.

Since only the sample is heated, ethanol condensation from the vapor on the sample or in the sealed SVA chamber is circumvented, although the ethanol vapor pressure could in theory be increased by heating the solvent reservoir.[75]

### 6.2.3. Solvent-Polymer Interaction Parameter and Surface Energy

The $\chi$ parameter of the PE and PEO copolymer blocks with the used ethanol solvent during SVA can be estimated from their Hildebrand solubility parameters, as described in the SI-Section 8..3. The formula is given below:

$$\chi_{12} \cong \frac{\sqrt{V_{m,1}V_{m,2}}}{RT}(\delta_1 - \delta_2)^2 \tag{6.2.2}$$

with molar volumes $V_{m,i}$ and solubility parameters $\delta_i$. The molar volumes and solubility parameters, as well as the calculated $\chi$'s for the copolymer blocks with ethanol are given in Tab. 6.2.2.

***Tab. 6.2.2:*** Values for molar volumes and solubility parameters of PE, PEO, and ethanol. Taken from[82]. The $\chi$ parameter were calculated from Eq. 6.2.2 for each copolymer block with ethanol. For comparison, the $\chi$ parameter of PEO with water is shown as well.

| | $V_m$ [cm$^3$/mol] | $\delta$ [MPa$^{0.5}$] | $\chi_{PE,PEO-EtOH}$ |
|---|---|---|---|
| PE | 29.787 | 19.2 | 0.825 |
| PEO | 39.111 | 23.8 | 0.111 |
| Ethanol | 58.390 | 26.2 | |
| $\chi_{PEO-H_2O}$ | | | $0.45 - 0.48$[79] |

The ethanol molecules will dissolve to a degree into the PE-*b*-PEO during SVA. There, the solvent will interact with the copolymer blocks and enhance the mobility of the chains. In the case of ethanol, the interaction with the PEO block will be stronger than with the PE block, as implied by the calculated $\chi$ parameter in Tab. 6.2.2, therefore swelling the BCP selectively. The degree of swelling is typically used to determine the solvent concentration in the BCP. Swelling and dissolution of lamellar PEO crystals of long-chain block copolymers in favorable solvents (i.e., water) have been reported before.[79, 83] However, the short-chain PE-*b*-PEO typically adopts an extended-chain conformation. As a result, there should be no significant swelling along the chain axis.

The change in surface energies of the copolymer blocks due to ethanol incorporation cannot be quantified, since the surface tension of a mixture is not a simple

function of pure component properties, but rather a complex function of the identities and concentrations in the mixture at its bulk and surface.[84] We can attempt to quantitatively describe the effect ethanol should have on the surface energies of the PE-*b*-PEO. Ethanol possesses a surface tension of 23.2 mJ/m$^2$ at 20 °C (8.7 % polarity).[85, 86] In the unheated vapor surrounding the heated sample, the low partial pressure of ethanol ($\approx$ 0.08 bar) would barely contribute to the surface tension of the ethanol-nitrogen vapor, thus having little effect on the free film surface.

The sample itself is heated up to 70 °C during SVA. However, tabulated surface tension values of ethanol (19.82 mJ/m$^2$) were only found up to 50 °C. Therefore, the following calculations are restricted to values at 50 °C. The interfacial energy of substrate and ethanol is calculated via the Owens, Wendt, Rabel and Kälble (OWRK) method (Eq. 2.4.11) described in Section 8.3. We receive an interfacial energy between pure ethanol and M3M-substrate of 4.55 mJ/m$^2$ at 50 °C. Earlier (Section 5.2.), an interfacial energy for pure PEO and M3M-functionalized substrate of 0.19 mJ/m$^2$ at 50 °C was calculated. Note that the interfacial energy of an ethanol-swollen PEO block will likely be in between these values. Nevertheless, the interfacial energy of the PE block with M3M-substrate (11.4 – 12.5 mJ/m$^2$) is by a factor two larger than that of ethanol with M3M, so a change in substrate wetting affinities is not expected under ethanol exposure.

## 6.3. Results and Discussion

**Ex Situ Nanoscale Morphology.** Fig. 6.3.1a-f depicts high resolution AFM phase images recorded at room temperature after the SVA (or TA) of the samples I-VI.[2] For comparison, the vertical lamellar morphology after regular TA at 120 °C is shown in (g). There are significant differences in the topography depending on the SVA parameters. The pre-annealed sample I in (a) consists mainly of standing cylinders after SVA at 60 °C. The standing cylinders form no lateral hexagonal lattice. In contrast, the as-cast sample III in (b) SVA-treated at 60 °C possesses no lateral surface nanostructures and appears mostly flat. A SVA temperature of 70 °C in (c) results in a vertical lamellar morphology for pre-annealed sample II, while the as-cast sample IV in (d) shows a mixed morphology of flat areas, vertical lamellae, and standing cylinders. Performing TA at 70 °C without saturated ethanol vapor results in the laterally rough segregated morphology found in (e) on the as-cast sample V. Raising the temperature during SVA to 120 °C as shown

[2]The Supporting Information of this chapter is shown in the appendix of this thesis, on page 125

in (f) for sample VI, which is the same target temperature as for the regular TA, results in a vertical lamellar morphology which is indistinguishable from a sample annealed via regular TA (g). The shown vertical lamellae in (f) and (g) exhibit exceptional lateral order along dewetting lines. The pitch or period of the vertical nanostructures is shown for each morphology in (h). The error bars in this context serve as a visualization for the lateral heterogeneity of the nanopattern pitch, which explains the large error bars for the irregular morphology of sample V in (e). All other pitches possess similar dimensions, which demonstrates the high driving force of the PE-*b*-PEO to form regular vertical nanopattern with defined sizes. This can be contributed to the extended-chain crystallization of the short-chain BCP described in Section 5.2.

**Effect of Ethanol Exposure.** The differences between solvent vapor exposure in Fig. 6.3.1d and exposure to nitrogen without ethanol in Fig. 6.3.1e under the same annealing conditions also demonstrates the effect the ethanol vapor has on the formation of the vertical lamellae. During SVA, the solvent diffuses into the BCP, where it enhances the mobility of the chains by reducing $\chi_{eff}$. Usually, this is in most BCP systems accompanied by high film swelling. However, the PE-*b*-PEO chains are mostly in an extended conformation, so a swelling is neither expected, nor observed, which makes it difficult to quantify the volume of solvent in the film. Nevertheless, we believe that the mobility of particularly short-chain BCPs can be enhanced even by small traces of solvent.

**Effect of Initial Sample Morphology.** The stark differences between the pre-annealed (a,c) and as-cast (b,d) morphologies in Fig. 6.3.1 indicates that the SVA at 60 °C and 70 °C is not sufficient to completely erase the sample's thermal (or crystalline) history. Although the ethanol should result in a lower $\chi_{eff}$, oriented nuclei of the vertical lamellae could remain during the SVA of the pre-annealed samples, which assist in the re-crystallization into vertical surface nanostructures. In contrast, the as-cast samples consisting of standing chains do not possess these oriented nuclei. As a consequence, the as-cast samples have a higher energetic and kinetic barrier for the PEO crystallization and the formation of vertical nanostructures, so they require higher temperatures for SVA. This becomes apparent by comparing the as-cast samples after SVA at 60 °C (b) and 70 °C (d), respectively. The 60 °C SVA treatment results in a flat morphology, while the 70 °C SVA treatment shows a mixed morphology of flat areas, vertical lamellae, and standing

cylinders. We conclude that not only the solvent vapor, but also the temperature has a significant effect on the mobility of the chains.

The lower mobility of the chains at lower SVA temperature also explains the difference between the standing cylinder morphology (a) after SVA at 60 °C and the vertical lamellae (c) after SVA at 70 °C of the pre-annealed samples. The ordering of cylinder-forming BCP is usually improved through various annealing procedures.[72] In literature, bulk PE-*b*-PEO samples with asymmetric chain lengths have been observed to form cylindrical mesophases between $80 - 90$ °C as the result of thermally activated motion of the short crystalline PE block transforming from the orthorhombic to pseudo-hexagonal lattice.[66, 87, 88] Different mesophases significantly affected the PEO crystallization kinetics due to topological confinement.[66] However, subsequent PEO crystallization in bulk PE-*b*-PEO always disrupted these mesophases and resulted in a double-crystalline lamellar morphology. The small regions with vertical lamellae in (a) imply that the standing cylinder morphology is not a stable crystalline microstructure like the vertical lamellae, but instead a kinetically 'frozen' morphology due to the lower mobility of the chains at lower SVA temperatures.

**Pre-Annealed In Situ Morphology During SVA.** A detailed *in situ* AFM study in Fig. 6.3.2 illuminates the effect temperature has on the sample topography during SVA. Large $10 \times 10$ $\mu$m AFM height images are used to track the evolution of the bottom layer, which has the extended chain thickness, with temperature. The full *in situ* AFM image series is shown in Section 8.3. The morphology of the pre-annealed sample I while reducing temperature during SVA is shown in Fig. 6.3.2a-c. While heating to 60 °C the bottom $L_1$ layer (not shown, see SI) splits into three distinct layers (A,B,C). The BCP redistributes laterally and the layers (A,B,C) shrink when temperature is reduced to 40 °C, before rising up and merging back into $L_1$, as depicted in Fig. 6.3.2j. In contrast, the pre-annealed sample II (d-f) shows less variation in the $L_1$ layer thickness when SVA is performed at 70 °C. Instead, it remains near the extended chain thickness of the regularly TA ($N_2$, 120 °C) sample (g-i). Despite the differences, all samples form a similar $\mu$m-scale morphology of discrete layers with extended chain thickness surrounded by finger-like dendrites, reminiscent from TA.

Notable are the high dynamics of sample I during SVA, despite employing the lowest annealing $T_{max}$ of all three depicted samples. The lateral spreading and vertical shrinkage of layer C indicates the formation of a wetting layer of PE-*b*-PEO

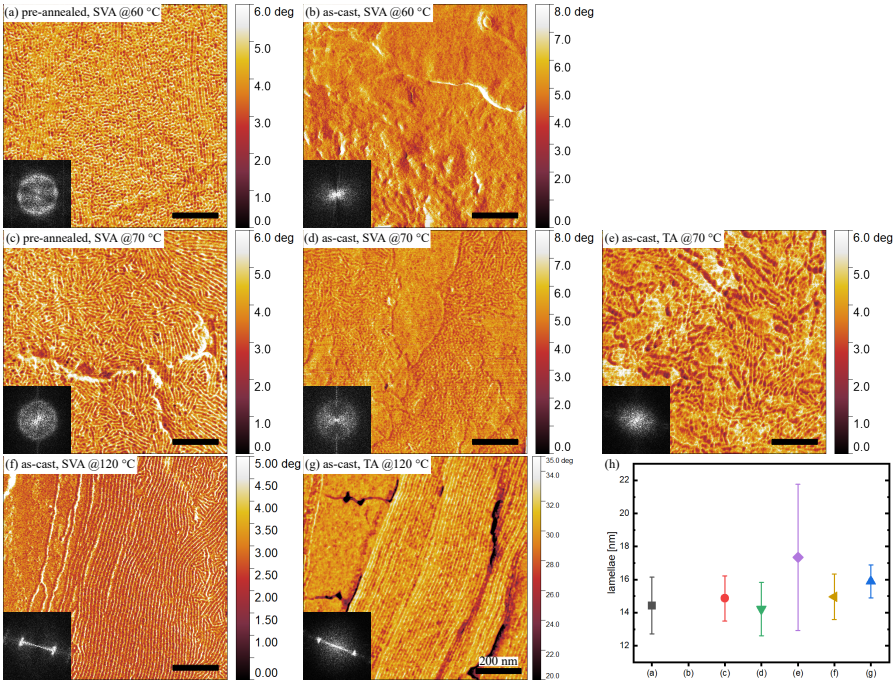


***Fig. 6.3.1.*** High-resolution *ex situ* AFM phase images ($1 \times 1$ $\mu$m) of PE-*b*-PEO thin film samples annealed under ethanol vapor or thermally annealed under different conditions. The 2d-FFT is shown in the bottom left of each image. (a) SVA of a pre-annealed sample (I) at T = 60 °C results in a morphology of standing cylinders with no hexagonal superlattice. (b) SVA of the as-cast sample (III) at the same temperature shows no vertical morphologies. (c) Performing SVA on a pre-annealed sample (II) at T = 70 °C leads to a vertical lamellar morphology, while using an as-cast sample (IV) results in a mixed morphology of vertical lamellae, standing cylinders, and flat areas (d). (e) Without ethanol vapor, the sample (V) forms a rough, laterally segregated morphology which is highly heterogeneous. The sample (VI) which was SVA (f) and the TA sample (g) at 120 °C have a nearly identical morphology. (h) Pitch of the vertical nanostructures measured for all samples. The error bars exemplify the lateral heterogeneity of the lamellar diameter.

on the substrate area, while layer A and B dewett and agglomerate around larger droplets. It is known that the dewetting mechanism is a function of the solvent volume fraction in the BCP film. At a low solvent volume fraction, dewetting of films proceeds via nucleation and growth, since low solvent content results in slow chain dynamics. On the other hand, a high solvent volume fraction can destabilise a film due to swelling and high chain mobility, leading to spinodal dewetting.[89] Since we observe no swelling during the timescale of the experiment, the solvent fraction in the film cannot be determined, although Fig. 6.3.1d-e demonstrate that the ethanol effects the mobility of the chains. Therefore, we estimate that a low volume fraction of solvent is present in the BCP, although primarily in the PEO phase due to ethanol selectivity. Additionally, it has been reported that during the early annealing stages, both microphase separation and dewetting compete. At lower temperatures, instead of interface-stabilized microphase separation, dewetting is reported to be the dominating process.[90] For the SVA at 60 °C in Fig. 6.3.2b-c there appears to be a transition when the dewetting process is reversed, and an interface-dominated, microphase separated morphology reappears. As a consequence, the separated A, B, and C layers combine into a single $L_1$ layer of standing extended chains. In comparison, the $L_1$ thickness of the 70 °C SVA sample in Fig. 6.3.2d-f remains far more stable. We assume that the dewetting dynamics might be simply faster at 70 °C than at 60 °C. Consequently, the morphology in Fig. 6.3.2d-f reflects an interface-stabilized equilibrium structure of standing extended chains. The low SVA temperature in Fig. 6.3.2a-c leads to a slower or delayed dewetting mechanism then at higher temperatures, which enables the observation of the dewetting/wetting dynamics.

**Morphology-Dependent Swelling Under Isothermal Conditions.** If the chain dynamics and dewetting process at 60 °C SVA temperature are slow, when does the sample reach a stable equilibrium state? After SVA on a pre-annealed sample (Ia) at 60 °C and subsequent cooling to 35 °C, the evolution of the film thickness and morphology was investigated over 20 h. In Fig. 6.3.3 the results are shown. The $5 \times 5$ $\mu$m AFM height images in (a-c) show that, except for a small area with tip induced agglomeration, the sample morphology consisting of discrete layers remains stable for the duration of the measurement. However, the individual thickness of each layer shifts over time, as illustrated in (d-f). While the lower layers shift towards higher thickness, the upper layers shrink slightly. The thickness changes could stem from internal, or external redistribution of chains

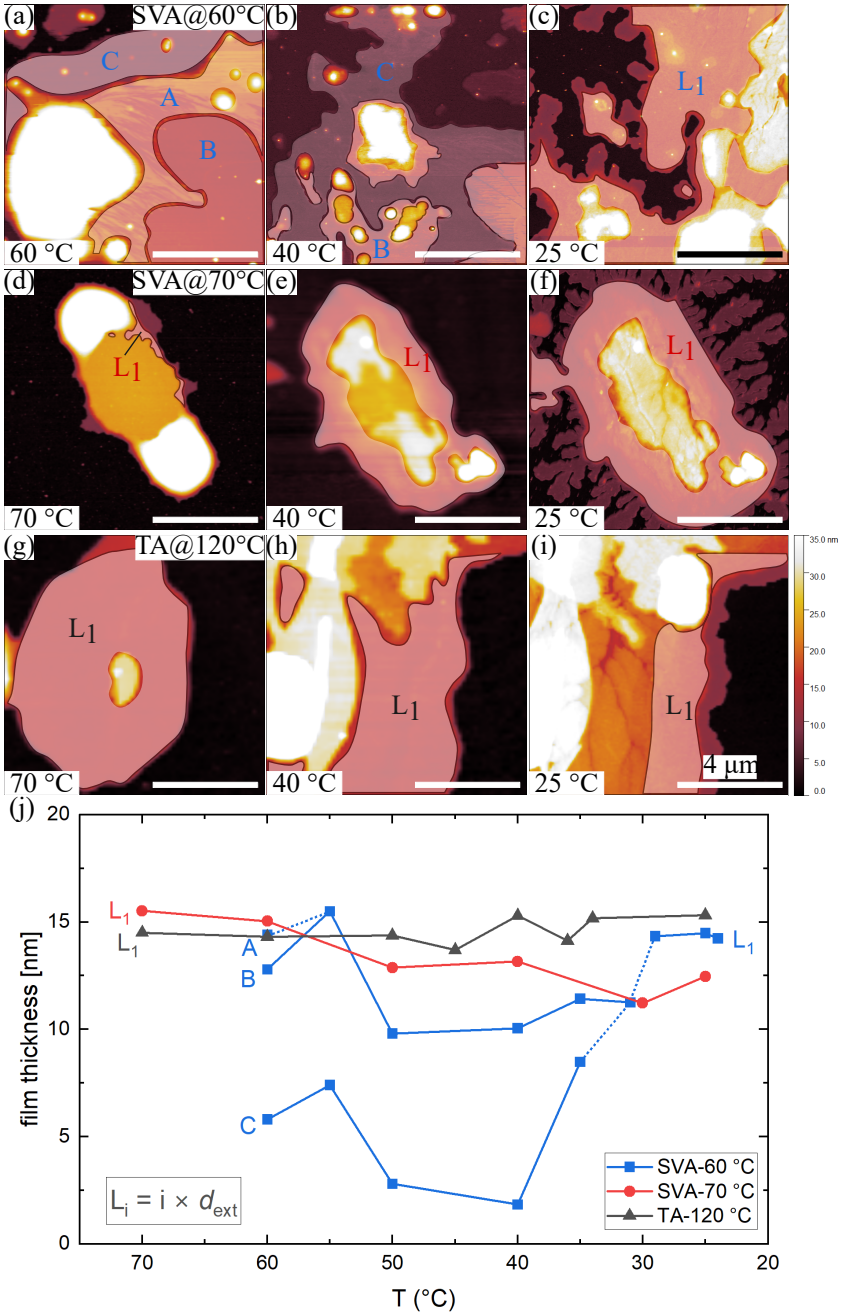


***Fig. 6.3.2.*** AFM height images (10 × 10 $\mu$m) of pre-annealed PE-*b*-PEO thin films during SVA and TA as a function of temperature. The tracked film layers are marked for better visibility (original images are shown in SI. 8.3). (a-c) SVA at 60 °C (I) leads to a strong lateral mobility of the BCP and the initial film layer with $L_1 = 1 \times d_{\text{ext}}$ splits into three layers (A,B,C). Cooling to 40 °C and then to 25 °C shows a reversible wetting/dewetting behavior. (d-f) In comparison, the layer thickness during SVA at 70 °C (II) remains stable, similar to the TA sample (e-i). (j) Thickness of the selected layer(s) of the film tracked over the temperature during the cooling process.

between layers or chain reorientation over time. The high resolution phase image in (g) recorded after 4 h shows featureless, flat areas and areas with bundles of vertical lamellae. The flat areas correspond to the $L'_{1-4}$ layers, while the vertical lamellae are found on the $L_{1-4}$ layers. The difference in morphology between the $L'$ and $L$ layers explains how there is a thickness difference of around 4.2 nm between the $L'_1$ and $L_1$ layer. In comparison, the other $L'$ and $L$ layers are similar in thickness.

Majumder et al. have described a self-induced nucleation mechanism which forms correlated stacks of flat-on crystal lamellae.[91] Similarly, the crystalline PE block in PE-*b*-PEO could mediate the formation of stacks of horizontal lamellae in $L'_{1-4}$ at 35 °C. Therefore, we assume that the PE-*b*-PEO chains in the $L'_i$ layers are standing vertically, whereas the $L_i$ chains are oriented horizontally. A transition in chain orientation over time, e.g. from vertical to horizontal standing chains is not observed. In fact, the $L'_{1,2}$ layers also change thickness over time, so the thickness increase is unlikely to be related solely to reorientation or tilting of the PE-*b*-PEO chains. Since the thickness increase is restricted to the two bottom layers, it indicates that the chain dynamics are enhanced near the heated substrate, possibly due to thermal gradients. The thermal gradient would result in larger mobility near or on the substrate, thus explaining the strong thickness increase of the bottom layers, whereas the other layers experience no increase. It is reasonable to assume that the standing chains in $L'_{1,2}$ are initially in a non-equilibrium due to the slow kinetics at low SVA temperatures. Assisted by the ethanol, the chains slowly unfold during the 20 h SVA, which increases the layers' thickness, up to the extended-chain length. Chain unfolding is disregarded for the horizontally lying chains forming the vertical lamellae in $L_{1-4}$, as the pitch of the lateral nanostructures remains stable over time. Instead, the thickness increase of layer $L_1$ is assumed to result from a combination of swelling from ethanol incorporation and vertical growth of the layer by surrounding chains slowly diffusing towards $L_1$.

**AFM Phase Shift During PEO Crystallization.** We compared the PEO crystallization between a TA sample (at 120 °C) and a SVA sample (at 60 °C). High-resolution AFM phase images during isothermal PEO crystallization are shown in Fig. 6.3.4. For each sample, the temperature after reaching the maximum annealing temperature was reduced to 40 °C, which is above the temperature, at which the vertical lamellae are usually observed. Then, the temperature was reduced by 1 °C/h while AFM images were recorded. Images (a-c) show subsequently

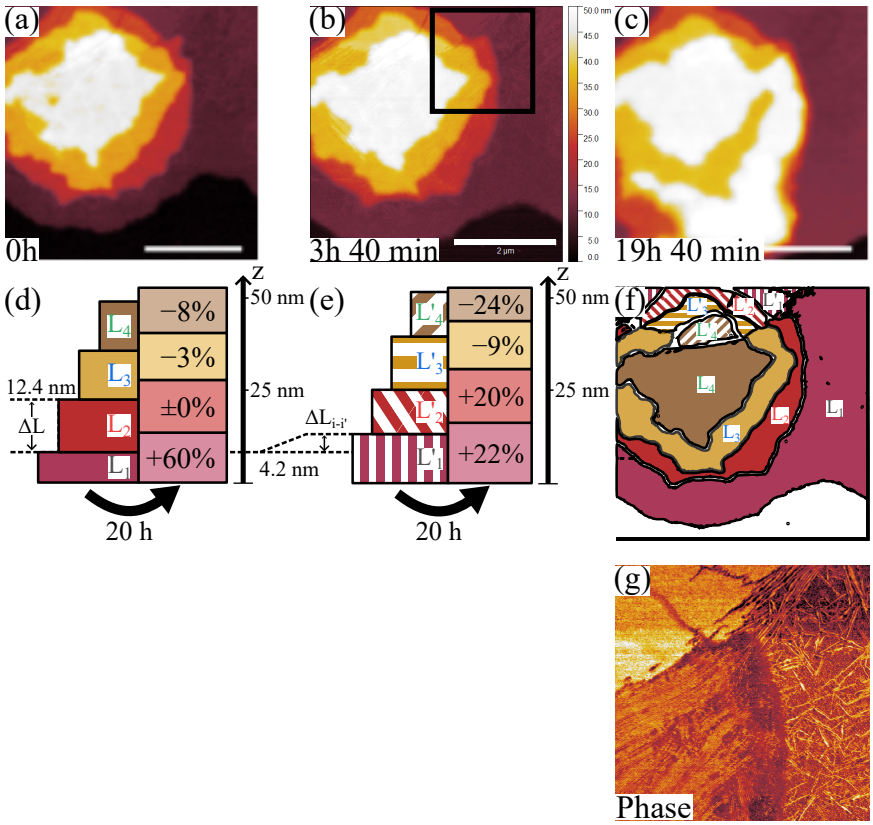


***Fig. 6.3.3.*** Change in thickness of individual film layers during SVA. The pre-annealed sample (Ia) was exposed to ethanol vapor at 60 °C, then cooled and held at 35 °C for 20 h. The morphology did not shift significantly, except for some AFM tip induced agglomeration (bottom part of (c)), as seen in the 5 × 5 $\mu$m AFM height images (a-c). (d-f) However, the thickness of the individual layers shifted over time. The bottom layers ($L_1$, $L_1^{'}$, $L_2^{'}$) showed an increase, while the top layers ($L_{3,4}$ and $L_{3,4}^{'}$) shrank. (g) A high-resolution 2 × 2 $\mu$m AFM phase image of the marked square area in (b) shows how the constant 4.2 nm offset in thickness between the L and L$^{'}$ layers in (d) and (e) correlates with topography.

recorded AFM phase images of the TA sample at 36 °C. The contrast change, coinciding with the appearance of the vertical lamellae, is seen in (b). For the SVA sample, the images in (d-f) show that the contrast change occurs at 31 °C. The vertical lamellae however, are observed before, at 35 °C (refer to Fig. 6.3.3h). It is reasonable to assume that, when solvent vapor annealing pre-annealed samples at 60 °C, not all double-crystalline, vertical lamellae completely dissolve. Oriented nuclei, or a mesomorphic layer of preoriented chains (i.e., 'melt memory') might persist, thus assisting re-crystallization as vertical lamellae.[83, 92, 93] It is interesting to note that the AFM phase contrast change is observed in both samples. The cause of the contrast change in TA (a-c) is the rotation of the chains during breakout crystallization, transforming the morphology from horizontal to vertical lamellae. In contrast, in SVA (d-f) the chains don't rotate, since the vertical lamellae already exist. The transition occurs at a larger undercooling than for the TA sample. However, earlier examples (e.g., see Section 5.3.3.) have shown a similar transition temperature for TA and SVA. Therefore, there is no direct evidence that the ethanol has an effect on PEO crystallization at the used partial pressure. Typically, a phase shift is attributed to a change in sample stiffness. We speculate that at a sufficient undercooling remaining ethanol is expelled from the crystal structure of (primarily) PEO, in order for the chains to achieve denser packing.

**As-Cast In Situ Morphology During SVA.** The comparison of the morphologies between the as-cast samples while cooling down after SVA demonstrates the effect temperature has on the ability of the PE-*b*-PEO to form vertical surface nanostructures. High-resolution AFM phase images of sample III and IV are shown in Fig. 6.3.5. The complete series of images is given in the SI-Section 8.3. At a SVA temperature of 60 °C, the phase image (a) of the as-cast sample III depicts a morphology of dark, isolated solid domains surrounded by a bright molten matrix. The same is observed for the as-cast sample IV in (e) at 70 °C. Reducing the temperature to 40 °C in (b) and (f) results in both samples in an inversion of phase contrast, with the solid domains now appearing bright, and the soft matrix appearing dark. The phase contrast inversion is caused by a transition from the hard tapping regime, where the phase shift is dominated by tip-sample contact area changes, which are greater on the soft matrix, to the moderate tapping regime, where the phase shift is proportional to the elastic modulus.[94] Furthermore, the solid, featureless domains grow laterally, at the expense of the soft matrix. The striking difference is that in the soft matrix in (f) a standing cylindrical mesostruc-

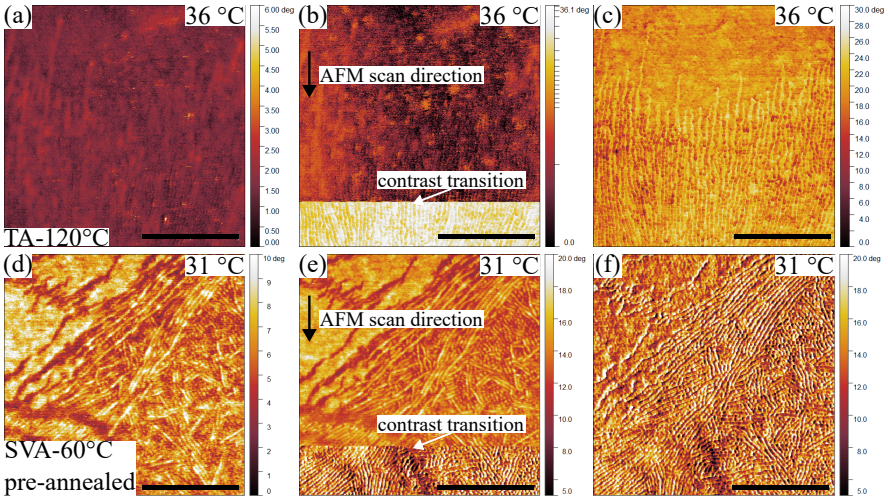


***Fig. 6.3.4.*** AFM phase images ($1 \times 1$ $\mu$m) during isothermal crystallization of the PEO block in PE-b-PEO during TA and SVA. The samples were continuously imaged with AFM (downward scan direction). (a-c) After TA at 120 °C, the temperature was reduced to 37 °C and then further reduced with a rate of 1 °C/h. The stark contrast transition associated with the PEO crystallization occurred at 36 °C, after which the vertical lamellae were observed. (d-f) After SVA of a pre-annealed sample at 60 °C (Ib) the sample temperature was reduced to 35 °C and then further reduced with a rate of 1 °C/h. A wide variety of morphologies, consisting of vertical lamellae, standing cylinders, and flat areas could be observed at 35 °C (image not shown). The phase contrast changed at 31 °C (e) and did not disturb the already formed vertical nanostructures.

ture is observed, whereas the soft matrix in (b) remains featureless. Additionally, upon reaching 30 °C, the phase image (g) of sample IV shows the phase contrast transition, after which a mixed morphology of flat, featureless areas, standing cylinders, and vertical lamellae is observed in (h). In comparison, the morphology of sample III in (c) and (d) remains featureless and flat as the isolated, flat solid domains simply coalesce.

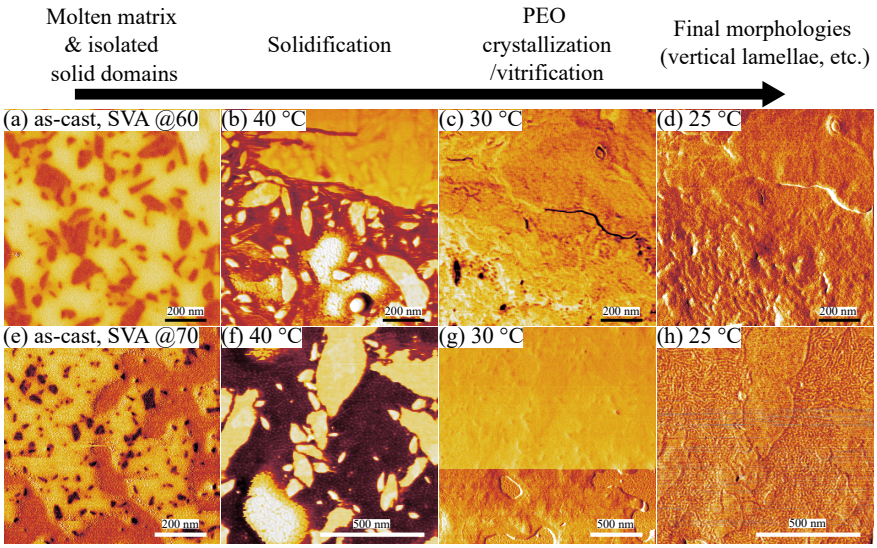


***Fig. 6.3.5.*** High-resolution AFM phase images ($1 \times 1$ $\mu$m) of as-cast PE-*b*-PEO thin films during SVA at different temperatures. (a) Heating of an as-cast sample (III) to 60 °C during SVA leads to the formation of isolated solid domains (dark) embedded in a soft/molten matrix (bright). (b-d) Stepwise reducing the temperature to 25 °C results in an inversion of the phase contrast and the lateral growth of the solid domains at the expense of the molten area. From 40 °C to 30 °C the sample surface solidifies completely and no vertical nanostructures form. (e-h) The as-cast sample (IV) heated to 70 °C during SVA shows a similar morphology of isolated solid domains and soft matrix at elevated temperatures. However, standing cylindrical mesostructures form in the soft matrix at 40 °C (f), and the phase contrast transition indicative of the PEO crystallization is seen at 30 °C in (g) ($2 \times 2$ $\mu$m). (h) After the PEO crystallization the sample topography is made up of vertical lamellae, standing cylinders, and flat areas.

The differences between the results of the as-cast samples can be simply understood by an energetic barrier, which has to be overcome to dissolve the as-cast lateral segregated morphology in order to allow sufficient chain rearrangement. In the case of TA, this is achieved by heating to 120 °C, where the crystal 'history' of the sample is completely erased.[47] Under the given experimental SVA conditions

at 60 − 70 °C, the exposure to ethanol vapor can only partly assist in the crystal melting, and isolated solid domains remain during SVA. However, despite the similarities, the PE-*b*-PEO chains in the soft matrix during SVA at 70 °C partly overcome this energetic barrier, which allows for greater rearrangement of the PE-*b*-PEO chains in the soft matrix. It was noted in Section 5.2. that the mobility of the chains during the *in situ* study determines their ability to form vertical surface nanopattern. Without sufficient mobility for breakout crystallization, the as-cast morphology will remain mostly static.

Furthermore, it could be that overcoming the energetic barrier for breakout crystallization encompasses a multi-step process. It has been suggested in literature, that crystallization is predated by the formation of a mesomorphic preordered layer due to disentanglement of chains prior to crystallization.[92] Similarly, the melting of the crystallites could first produce a preordered mesomorphic layer of chains in close vicinity to the crystal. In a crystalline BCP thin film, the mesomorphic layer during melting might be stabilized due to microphase separation and interfacial effects. Although technically 'non-crystalline', the mobility of the chains in the preordered layer will be restricted. Higher annealing temperatures during SVA, for example 70 °C instead of 60 °C, therefore disrupt the mesomorphic layer and enable higher chain mobility necessary for breakout crystallization of the PE-*b*-PEO chains.

## 6.4. Summary

In this study, the effect of SVA on the morphology of PE-*b*-PEO thin films has been discussed. It was found that the presence of a weakly selective solvent (ethanol) enhances the mobility of the PE-*b*-PEO chains, allowing for structural rearrangement into vertical lamellae at lower temperatures than under thermal annealing conditions. The intake of solvent could not be quantified due to a lack of swelling of the film. On a longer timescale film thickness changes were associated with thermally activated diffusion of chains and partial structural rearrangement, possibly supported by ethanol presence in the film and vapor. We assume that the effect of ethanol is limited to promoting chain mobility in the thin film and has little effect on interfacial energies or surface tension, since the vertical lamellae-producing, breakout-crystallization mechanism appears to be the same as for thermal annealing. This emphasizes the strong tendency for crystallization of the PEO block even in the presence of a weakly selective solvent.

Temperature was found to have a greater effect on chain mobility than the solvent exposure. This was attributed to the low vapor pressure of the ethanol, which was limited by the experimental setup. For example, the dewetting and wetting dynamics of the film were significantly slowed at low SVA temperatures. As a result, structural reorganization was limited, which restricted the film's ability to form vertical surface nanopatterns in the as-cast sample. Furthermore, incomplete melting of the pre-annealed sample at low SVA temperatures led to the re-crystallization of the vertical lamellae as standing cylinders. It is reasonable to assume that the melting of the double-crystalline PE-*b*-PEO is a multi-step process. The melting of the crystalline domains first produces a preordered mesomorphic layer, which has to be further heated to transition to a microphase separated morphology, and finally, an isotropic melt. When re-crystallization occurs in the mesomorphic state, the initial crystalline morphology is mostly restored because the intermolecular forces between chains hinder morphological reorganization towards a thermodynamic equilibrium structure. Therefore, we conclude that the standing cylinder morphology is a kinetically trapped morphology. The standing cylinder morphology has a larger PE-*b*-PEO interface than the lamellae. Whether this is caused by a lowered $\chi_{eff}$ due to ethanol exposure or results from the slow kinetics associated with partial melting and re-crystallization remains unclear.

Our results demonstrate that the kinetics and morphology of the ordering of crystallizable PE-*b*-PEO thin films during SVA are highly dependent on the processing pathway.[95] Despite the pronounced tendency of the PE-*b*-PEO to form vertical lamellae, the kinetics and crystal 'history' of the film become increasingly important at lower annealing temperatures. It would be of great interest to further study the effect of solvent on PE-*b*-PEO thin films at higher vapor pressures, and to investigate the effect that different selective solvents have on thin film morphology, potentially in combination with directed self-assembly (DSA). This could unlock new possibilities for producing vertical nanostructures of PE-*b*-PEO in addition to the lamellae in the sub-10 nm regime.

# 7. Conclusion and Outlook

Today, polymers are essential materials that permeate nearly every aspect of daily life, underscoring their significance and the importance of continued research in this field. Their remarkable structural and functional diversity enables a wide range of applications across many technological fields. The structure of polymers is closely linked to their properties, allowing them to be precisely tailored for specific applications. However, a comprehensive understanding of each polymer system is crucial, since properties are significantly affected by preparation methods, environmental factors, etc. Interfaces of polymers play a significant role in the design of novel functional materials, as they can influence properties such as adhesion, wettability, electrical conductivity, mechanical performance, and more. Thin polymer films exhibit properties distinct from their bulk counterparts, making them ideal systems for investigating interfacial effects.

Atomic Force Microscopy (AFM) is an ideal technique for investigating thin polymer film systems under a variety of conditions that closely resemble real operational environments. In this thesis, two exemplary thin polymer film systems were studied: a conductive polymer in an electrolyte under applied electrical potential, and a crystallizable, short-chain block copolymer (BCP) examined across different temperatures and environmental conditions.

The conductive polypyrrole (PPY) film was studied to uncover how its internal structure and topography relate to the microscopic distribution of its elastic properties, which is highly relevant for interfacial design in the engineering of functional electroactive devices. Our results showed that the film thickness and elastic modulus closely follow the applied electric potential, demonstrating that the electrolyte diffusion is dominated by anions. Furthermore, we found that the nodular topography of the PPY film is closely linked to the heterogeneous modulation of the elastic modulus on the film surface. The findings highlight that in the development of electroactive devices particular emphasis should be placed on the deliberate design of interfaces, as surface heterogeneities largely govern overall device behavior, including device performance and operational lifetime.

Interface-related phenomena are particularly important in block copolymer thin films because they influence the orientation of microdomains, which is crucial for the development of novel bottom-up nanopatterning techniques. Therefore, the formation of vertical surface nanostructures via crystallization of a thin poly(ethylene)-*block*-poly(ethylene oxide) (PE-*b*-PEO) film was investigated in

pursuit of a novel pathway for bottom-up nanofabrication in the sub-10 nm regime. We observed that thermal annealing (TA) of a PE-*b*-PEO thin film first transformed the as-cast film into a microphase-separated horizontal morphology, which was then overwritten by breakout crystallization of the vertical, extended-chain crystal lamellae. In consideration of interfacial effects, we conclude that the vertical extended-chain lamellae are thermodynamically favored, while other observed morphologies form through kinetic pathways. Additionally, the vertical lamellae can be aligned over large areas using trench guiding patterns, demonstrating their potential for the preparation of ordered nanoarrays. We also described the effects of solvent exposure and temperature on self-assembly kinetics, revealing that sufficient kinetic energy of the chains is pivotal for breakout crystallization and the formation of vertical nanostructures. As an outcome, this work suggests a unique approach for nanofabrication based on extended-chain crystallization of short-chain block co-oligomers. We believe that extended-chain crystallization can mitigate some of the challenges associated with low-$N$ BCPs by providing a means to increase the effective interaction parameter $\chi_{eff}$, thereby enabling the development of regular sub-10 nm nanopatterned arrays.

However, the post-processing capabilities of short-chain PE-*b*-PEO remain unclear. Initial attempts at sequential infiltration synthesis using atomic layer deposition suffered from insufficient temperature stability of the BCP film and the presence of water in the process. The preliminary infiltration experiments indicate a need to either fixate the BCP on the substrate after nanopattern formation, or employ a low-temperature, water-free process to enhance stability.

Besides stability, different selective infiltration procedures and their effect on morphology could be explored in the future, e.g. dissolving the BCP together with a precursor prior to drop-casting or spin-coating of the film. If feasible, X-ray techniques with well-defined, attenuated beams could be used to avoid irradiation damage to the BCP while elucidating the chain orientation in the crystalline BCP film. Furthermore, future studies could investigate how higher vapor partial pressures or different selective solvents or solvent mixtures during solvent vapor annealing (SVA) impact film morphology. Potentially, highly aligned arrays of conducting polymers using BCP templates[96], or BCPs with a conductive, crystallizable block could be fabricated for a new class of functional, structured nanomaterials in the sub-10 nm regime.

In summary, this thesis has explored the interfacial effects of thin functional polymer films, highlighting key concepts as strategies for the development of novel

nanomaterials and devices. Given the vast diversity of polymers and their wide-ranging applications, the field continues to offer significant opportunities for innovation. Nevertheless, further advances will require continued efforts in characterization and a deeper understanding of the complex structure-property relationships that govern the majority of polymer materials.

# Bibliography


[1] P. Hiemenz, T. Lodge, *Polymer Chemistry*, 2nd ed., CRC Press, **2007**.

[2] H. Nalwa, *Handbook of Organic Conductive Molecules and Polymers, Conductive Polymers: Synthesis and Electrical Properties*, Wiley, **1997**.

[3] R. Baughman, *Synthetic Metals* **1996**, *78*, 339–353.

[4] T. Otero, J. Martinez, J. Arias-Pardilla, *Electrochimica Acta* **2012**, *84*, 112–128.

[5] C. Li, H. Bai, G. Shi, *Chem. Soc. Rev.* **2009**, *38*, 2397–2409.

[6] M. J. Fasolka, A. M. Mayes, *Annual Review of Materials Research* **2001**, *31*, 323–355.

[7] C. Park, J. Yoon, E. L. Thomas, *Polymer* **2003**, *44*, 6725–6760.

[8] S. Darling, *Progress in Polymer Science* **2007**, *32*, 1152–1204.

[9] D. Wang, T. P. Russell, *Macromolecules* **2018**, *51*, 3–24.

[10] C. Beebee, E. B. Watkins, R. M. Sapstead, V. C. Ferreira, K. S. Ryder, E. L. Smith, A. R. Hillman, *Electrochimica Acta* **2019**, *295*, 978–988.

[11] A. Gelmi, M. J. Higgins, G. G. Wallace, *Biomaterials* **2010**, *31*, 1974–1983.

[12] C. M. Bates, M. J. Maher, D. W. Janes, C. J. Ellison, C. G. Willson, *Macromolecules* **2014**, *47*, 2–12.

[13] C. Sinturel, F. S. Bates, M. A. Hillmyer, *ACS Macro Letters* **2015**, *4*, 1044–1050.

[14] K. Brassat, D. Kool, C. G. A. Nallet, J. K. N. Lindner, *Advanced Materials Interfaces* **2020**, *7*, 1901605.

[15] L. Wilson, *Emerging Research Materials (ERM)* **2013**, *1*.

[16] M. Luo, T. H. I. Epps, *Macromolecules* **2013**, *46*, 7567–7579.

[17] C. De Rosa, R. Di Girolamo, A. Malafronte, M. Scoti, G. Talarico, F. Auriemma, O. Ruiz de Ballesteros, *Polymer* **2020**, *196*, 122423.

[18] J. R. Fried, *Polymer Science & Technology*, third edition, Pearson Education, **2014**.

[19] W. Hu, *Polymer Physics - A Molecular Approach*, 1st ed., Springer Vienna, **2013**.

[20] T. Vernitskaya, O. Efimov, *Russian Chemical Reviews* **1997**, *66*, 443–457.

[21] J. Lauritzen, John I., J. D. Hoffman, *The Journal of Chemical Physics* **1959**, *31*, 1680–1681.

[22] J. D. Hoffman, J. I. Lauritzen, *Journal of Research of the National Bureau of Standards Section A: Physics and Chemistry* **1961**, *65A*, 297.

[23] T. Arakawa, B. Wunderlich, *Journal of Polymer Science Part A-2: Polymer Physics* **1966**, *4*, 53–62.

[24] M. Hikosaka, K. Amano, S. Rastogi, A. Keller, *Macromolecules* **1997**, *30*, 2067–2074.

[25] K. Saalwächter, T. Thurn-Albrecht, W. Paul, *Macromolecular Chemistry and Physics* **2023**, *224*, 2200424.

[26] R. L. Miller, *Polymer* **1992**, *33*, 1783–1784.

[27] M. C. Scharber, N. S. Sariciftci, *Advanced Materials Technologies* **2021**, *6*, 2000857.

[28] L. Bay, T. Jacobsen, S. Skaarup, K. West, *The Journal of Physical Chemistry B* **2001**, *105*, 8492–8497.

[29] J. G. Ibanez, M. E. Rincón, S. Gutierrez-Granados, M. Chahma, O. A. Jaramillo-Quintero, B. A. Frontana-Uribe, *Chemical Reviews* **2018**, *118*, 4731–4816.

[30] M. F. Suárez, R. G. Compton, *Journal of Electroanalytical Chemistry* **1999**, *462*, 211–221.

[31] R. Z. Pytel, E. L. Thomas, I. W. Hunter, *Polymer* **2008**, *49*, 2008–2013.

[32] T. Otero, J. López Cascales, G. Vázquez Arenas, *Materials Science and Engineering: C* **2007**, *27*, 18–22.

[33] W. Zheng, P. G. Whitten, G. M. Spinks, *Multifunctional Materials* **2018**, *1*, 014002.

[34] A. H. Hofman, G. ten Brinke, K. Loos, *Polymer* **2016**, *107*, 343–356.

[35] M. W. Matsen, F. S. Bates, *Macromolecules* **1996**, *29*, 1091–1098.

[36] J. N. Albert, T. H. Epps, *Materials Today* **2010**, *13*, 24–33.

[37] J.-U. Sommer, G. Reiter in *Ordered Polymeric Nanostructures at Surfaces*, (Ed.: G. J. Vancso), Springer Berlin Heidelberg, Berlin, Heidelberg, **2005**, pp. 1–36.

[38] X. Chevalier, G. Pound-Lana, C. Gomes Correia, S. Cavalaglio, B. Cabannes-Boué, F. Restagno, G. Miquelard-Garnier, S. Roland, C. Navarro, G. Fleury, M. Zelsmann, *Nanotechnology* **2023**, *34*, 175602.

[39] D. K. Owens, R. C. Wendt, *Journal of Applied Polymer Science* **1969**, *13*, 1741–1747.

[40] G. Reiter, G. Castelein, P. Hoerner, G. Riess, A. Blumen, J.-U. Sommer, *Phys. Rev. Lett.* **1999**, *83*, 3844–3847.

[41] W. Xu, Y. Zheng, P. Pan, *Journal of Polymer Science* **2022**, *60*, 2136–2152.

[42] R. M. Michell, A. J. Müller, *Progress in Polymer Science* **2016**, *54-55*, 183–213.

[43] S. Nakagawa, H. Marubayashi, S. Nojima, *European Polymer Journal* **2015**, *70*, 262–275.

[44] R. M. Van Horn, M. R. Steffen, D. O'Connor, *POLYMER CRYSTALLIZATION* **2018**, *1*, e10039.

[45] W.-N. He, J.-T. Xu, *Progress in Polymer Science* **2012**, *37*, 1350–1400.

[46] W. Hu, D. Frenkel, *Faraday Discuss.* **2005**, *128*, 253–260.

[47] L. Sun, Y. Liu, L. Zhu, B. S. Hsiao, C. A. Avila-Orta, *Polymer* **2004**, *45*, 8181–8193.

[48] J.-P. Yang, Q. Liao, J.-J. Zhou, X. Jiang, X.-H. Wang, Y. Zhang, S.-D. Jiang, S.-K. Yan, L. Li, *Macromolecules* **2011**, *44*, 3511–3516.

[49] Y. Wang, C.-M. Chan, K.-M. Ng, L. Li, *Macromolecules* **2008**, *41*, 2548–2553.

[50] Y. Ma, Hu, G. Reiter, *Macromolecules* **2006**, *39*, 5159–5164.

[51] J. Fu, Y. Wei, L. Xue, B. Luan, C. Pan, B. Li, Y. Han, *Polymer* **2009**, *50*, 1588–1595.

[52] J. G. Murphy, J. G. Raybin, S. J. Sibener, *Journal of Polymer Science* **2022**, *60*, 1042–1058.

[53] R. Garcia, R. Pérez, *Surface Science Reports* **2002**, *47*, 197–301.

[54] R. Garcia, *Chem. Soc. Rev.* **2020**, *49*, 5850–5884.

[55] H.-J. Butt, B. Cappella, M. Kappl, *Surface Science Reports* **2005**, *59*, 1–152.

[56] E. Smela, *Advanced Materials* **2003**, *15*, 481–494.

[57] B. Roschning, J. Weissmüller, *Electrochimica Acta* **2019**, *318*, 504–512.

[58] S. Alam, S. Jadoon, M. Z. Iqbal, H. H. Hegazy, Z. Ahmad, I. S. Yahia, *Journal of Energy Storage* **2024**, *85*, 110955.

[59] P. H. Lakner, M. Brinker, C. Seitz, L. Jacobse, V. Vonk, M. Lippmann, S. Volkov, P. Huber, T. F. Keller, *Langmuir* **2020**, *36*, 13448–13456.

[60] A. Meinhardt, P. Lakner, P. Huber, T. F. Keller, *Nanoscale Adv.* **2024**, *6*, 102–110.

[61] L. A. McCullough, K. M. and, *Molecular Crystals and Liquid Crystals* **2010**, *521*, 1–55.

[62] Y.-H. Chung, J. K. Oh, *Biosensors* **2024**, *14*, 542.

[63] P. P. Angelopoulou, I. Moutsios, G.-M. Manesi, D. A. Ivanov, G. Sakellariou, A. Avgeropoulos, *Progress in Polymer Science* **2022**, *135*, 101625.

[64] R. Schulze, M. M. L. Arras, G. Li Destri, M. Gottschaldt, J. Bossert, U. S. Schubert, G. Marletta, K. D. Jandt, T. F. Keller, *Macromolecules* **2012**, *45*, 4740–4748.

[65] W. Cao, K. Tashiro, H. Masunaga, S. Sasaki, M. Takata, *The Journal of Physical Chemistry B* **2009**, *113*, 8495–8504.

[66] X. Zhang, R. Schulze, P. Zhang, C. Lüdecke, X. Zhang, Z. Su, K. D. Jandt, *Polymer* **2014**, *55*, 1893–1900.

[67] A. Meinhardt, P. Qi, C. David, I. Maximov, T. F. Keller, *Advanced Materials Interfaces* **2025**, *12*, 2400661.

[68] G. Miquelard-Garnier, S. Roland, *European Polymer Journal* **2016**, *84*, 111–124.

[69] G. Reiter, J.-U. Sommer, *The Journal of Chemical Physics* **2000**, *112*, 4376–4383.

[70] G. Reiter, L. Vidal, *Eur. Phys. J. E* **2003**, *12*, 497–505.

[71] P. Zhang, H. Huang, D. Yan, T. He, *Langmuir* **2012**, *28*, 6419–6427.

[72] P. W. Majewski, K. G. Yager, *Journal of Physics: Condensed Matter* **2016**, *28*, 403002.

[73] C. Sinturel, M. Vayer, M. Morris, M. A. Hillmyer, *Macromolecules* **2013**, *46*, 5399–5415.

[74] R. Ma, X. Zhang, D. Sutherland, V. Bochenkov, S. Deng, *International Journal of Extreme Manufacturing* **2024**, *6*, 062004.

[75] P. Pula, A. Leniart, P. W. Majewski, *Soft Matter* **2022**, *18*, 4042–4066.

[76] H. Hulkkonen, T. Salminen, T. Niemi, *Soft Matter* **2019**, *15*, 7909–7917.

[77] B. Nandan, M. K. Vyas, M. Böhme, M. Stamm, *Macromolecules* **2010**, *43*, 2463–2473.

[78] W. A. Phillip, M. A. Hillmyer, E. L. Cussler, *Macromolecules* **2010**, *43*, 7763–7770.

[79] P. Yang, X. Yu, Y. Han, *Polymer* **2010**, *51*, 4948–4957.

[80] S. H. Kim, M. J. Misner, T. Xu, M. Kimura, T. P. Russell, *Advanced Materials* **2004**, *16*, 226–231.

[81] C. B. Kretschmer, R. Wiebe, *Journal of the American Chemical Society* **1949**, *71*, 1793–1797.

[82] D. Van Krevelen, K. Te Nijenhuis in *Properties of Polymers (Fourth Edition)*, (Eds.: D. Van Krevelen, K. Te Nijenhuis), Elsevier, Amsterdam, **2009**, pp. 229–244.

[83] B. Bessif, B. Heck, T. Pfohl, C. M. Q. Le, A. Chemtob, V. Pirela, J. Elgoyhen, R. Tomovska, A. J. Müller, G. Reiter, *Macromolecules* **2023**, *56*, 1461–1470.

[84] P. Wang, A. Anderko, R. D. Young, *Fluid Phase Equilibria* **2004**, *226*, 71–82.

[85] G. Vazquez, E. Alvarez, J. M. Navaza, *Journal of Chemical & Engineering Data* **1995**, *40*, 611–614.

[86] A. Zdziennicka, J. Krawczyk, K. Szymczyk, B. Jańczuk, *Colloids and Surfaces A: Physicochemical and Engineering Aspects* **2017**, *529*, 864–875.

[87] M. A. Hillmyer, F. S. Bates, *Macromolecular Symposia* **1997**, *117*, 121–130.

[88] C. Weiyu, K. Tashiro, M. Hanesaka, S. Takeda, H. Masunaga, S. Sasaki, M. Takata, *Journal of Physics: Conference Series* **2009**, *184*, 012003.

[89] E. O. Ningrum, W.-T. Lin, C.-T. Lo, *Polymer Engineering & Science* **2011**, *51*, 1339–1346.

[90] C. Huang, G. Wen, J. Li, T. Wu, L. Wang, F. Xue, H. Li, T. Shi, *Journal of Colloid and Interface Science* **2016**, *478*, 236–245.

[91] S. Majumder, P. Poudel, H. Zhang, J. Xu, G. Reiter, *Polymer International* **2020**, *69*, 1058–1065.

[92] G. Strobl, *The European Physical Journal E* **2000**, *3*, 165–183.

[93] J. Xu, G. Reiter, R. G. Alamo, *Crystals* **2021**, *11*, 304.

[94] S. Magonov, V. Elings, M.-H. Whangbo, *Surface Science* **1997**, *375*, L385–L391.

[95] K. Sharma, A. Agrawal, A. Masud, S. K. Satija, J. F. Ankner, J. F. Douglas, A. Karim, *ACS Applied Materials & Interfaces* **2023**, *15*, 21562–21574.

[96] J. I. Lee, S. H. Cho, S.-M. Park, J. K. Kim, J. K. Kim, J.-W. Yu, Y. C. Kim, T. P. Russell, *Nano Letters* **2008**, *8*, 2315–2320.

[97] M. Pyo, C.-H. Kwak, *Synthetic Metals* **2005**, *150*, 133–137.

[98] T. Silk, Q. Hong, J. Tamm, R. G. Compton, *Synthetic Metals* **1998**, *93*, 59–64.

[99] S. Sadki, P. Schottland, N. Brodie, G. Sabouraud, *Chem. Soc. Rev.* **2000**, *29*, 283–293.

[100] R. Adhikari, B. Lamsal, T. R. Bhandari, S. P. Khatiwada, G. H. Michler in *Conjugated Polymers for Next-Generation Applications*, (Eds.: V. Kumar, K. Sharma, R. Sehgal, S. Kalia), Woodhead Publishing Series in Electronic and Optical Materials, Woodhead Publishing, **2022**, pp. 113–146.

[101] M. Brinker, M. Thelen, M. May, D. Rings, T. Krekeler, P. Lakner, T. F. Keller, F. Bertram, N. Huber, P. Huber, *Phys. Rev. Mater.* **2022**, *6*, 116002.

[102] M. Brinker, G. Dittrich, C. Richert, P. Lakner, T. Krekeler, T. F. Keller, N. Huber, P. Huber, *Science Advances* **2020**, *6*, eaba1483.

[103] M. Gandhi, P. Murray, G. Spinks, G. Wallace, *Synthetic Metals* **1995**, *73*, 247–256.

[104] E. Smela, N. Gadegaard, *The Journal of Physical Chemistry B* **2001**, *105*, 9395–9405.

[105] L. Kim, C. Gabrielli, A. Pailleret, H. Perrot, *Electrochimica Acta* **2011**, *56*, 3516–3525.

[106] M. J. Higgins, S. T. McGovern, G. G. Wallace, *Langmuir* **2009**, *25*, 3627–3633.

[107] S. Vlassov, S. Oras, M. Antsov, I. Sosnin, B. Polyakov, A. Shutka, M. Y. Krauchanka, L. M. Dorogin, *Rev. Adv. Mater. Sci* **2018**, *56*, 62–78.

[108] P. Knittel, M. J. Higgins, C. Kranz, *Nanoscale* **2014**, *6*, 2255–2260.

[109] J. Roa, G. Oncins, J. Diaz, F. Sanz, M. Segarra, *Recent Patents on Nanotechnology* **2011**, *5*, 27–36.

[110] B. Cappella, G. Dietler, *Surface Science Reports* **1999**, *34*, 1–104.

[111] T. Young, M. Monclus, T. Burnett, W. Broughton, S. Ogin, P. Smith, *Meas. Sci. Technol.* **2011**, *22*, 125703.

[112] D. Passeri, A. Alippi, A. Bettucci, M. Rossi, E. Tamburri, M. Terranova, *Synthetic Metals* **2011**, *161*, 7–12.

[113] M. E. Dokukin, I. Sokolov, *Langmuir* **2012**, *28*, 16060–16071.

[114] J. Kámán, R. Huszánk, A. Bonyár, *Micron* **2019**, *125*, 102717.

[115] L. Sirghi in *Microscopy: Science, Technology, Applications and Education*, (Eds.: A. Mendez-Vilas, J. Diaz), Microscopy Book Series 4, Formatex Research Center, **2010**, pp. 433–440.

[116] K. Lepicka, M. Majewska, R. Nowakowski, W. Kutner, P. Pieta, *Electrochimica Acta* **2019**, *297*, 94–100.

[117] A. Stierle, T. Keller, H. Noei, V. Vonk, R. Roehlsberger, *Journal of large-scale research facilities* **2016**, *2*, 1–9.

[118] A. Diaz, J. I. Castillo, J. Logan, W.-Y. Lee, *Journal of Electroanalytical Chemistry and Interfacial Electrochemistry* **1981**, *129*, 115–132.

[119] S. J. Hahn, W. E. Stanchina, W. J. Gajda, P. Vogelhut, *Journal of Electronic Materials* **1986**, *15*, 145–149.

[120] U. Paramo-García, J. Ibanez, N. Batina, *International Journal of Electrochemical Science* **2013**, *8*, 2656–2669.

[121] J.-H. Hwang, M. Pyo, *Synthetic Metals* **2007**, *157*, 155–159.

[122] K. K. Keiichi Kaneto, Y. S. Yasuaki Sonoda, W. T. Wataru Takashima, *Japanese Journal of Applied Physics* **2000**, *39*, 5918.

[123] E. Smirnova, A. Ankudinov, I. Chepurnaya, A. Timonov, M. Karushev, *Inorganics* **2023**, *11*, 1–11.

[124] S. Jafarzadeh, P. M. Claesson, P.-E. Sundell, J. Pan, E. Thormann, *ACS Applied Materials & Interfaces* **2014**, *6*, 19168–19175.

[125] G. Spinks, L. Liu, G. Wallace, D. Zhou, *Advanced Functional Materials* **2002**, *12*, 437–440.

[126] H. J. G. J. F. Waters, P. R. Guduru, *The Journal of Adhesion* **2011**, *87*, 194–213.

[127] A. G. Peressadko, N. Hosoda, B. N. J. Persson, *Phys. Rev. Lett.* **2005**, *95*, 124301.

[128] J. N. Murphy, K. D. Harris, J. M. Buriak, *PLOS ONE* **2015**, *10*, 1–32.

[129] E. Matxinandiarena, A. Múgica, M. Zubitur, V. Ladelta, G. Zapsas, D. Cavallo, N. Hadjichristidis, A. J. Müller, *Polymers* **2021**, *13*, 3133.

[130] O. Dolynchuk, T. Thurn-Albrecht, *Macromolecular Chemistry and Physics* **2023**, *224*, 2200455.

[131] A. Cicolella, F. De Stefano, M. Scoti, G. Talarico, J. M. Eagan, G. W. Coates, R. Di Girolamo, C. De Rosa, *Macromolecules* **2024**, *57*, 2230–2245.

[132] L. Sangroniz, B. Wang, Y. Su, G. Liu, D. Cavallo, D. Wang, A. J. Müller, *Progress in Polymer Science* **2021**, *115*, 101376.

[133] C. Pinto-Gómez, F. Pérez-Murano, J. Bausells, L. G. Villanueva, M. Fernández-Regúlez, *Polymers* **2020**, *12*, 2432.

[134] D. Lu, V. A. Bobrin, *Biomacromolecules* **2024**, *25*, 7058–7077.

[135] C. M. Papadakis, C. Darko, Z. Di, K. Troll, E. Metwalli, A. Timmann, G. Reiter, S. Förster, *The European Physical Journal E* **2011**, *34*, 1–8.

[136] G. Reiter, G. Castelein, P. Hoerner, G. Riess, J.-U. Sommer, G. Floudas, *The European Physical Journal E* **2000**, *2*, 319–334.

[137] G. Reiter, G. Castelein, J.-U. Sommer, *Macromolecular Symposia* **2002**, *183*, 173–178.

[138] Y. Ming, T. Hao, Z. Zhou, S. Zhang, Y. Nie, *Crystal Growth & Design* **2023**, *23*, 7653–7661.

[139] D. Lin, H. Wei, J. Wei, J. Xu, C. Zhang, X. Wang, *Macromolecules* **2024**, *57*, 2801–2809.

[140] R. Castillo, A. Müller, *Progress in Polymer Science* **2009**, *34*, 516–560.

[141] C. De Rosa, R. Di Girolamo, A. Cicolella, G. Talarico, M. Scoti, *Polymers* **2021**, *13*, 2589.

[142] H. Schmalz, V. Abetz, *Polymers* **2022**, *14*, 696.

[143] L. Chu, W. J. B. Grouve, M. van Drongelen, E. G. de Vries, R. Akkerman, M. B. de Rooij, *Advanced Materials Interfaces* **2021**, *8*, 2001894.

[144] H. Zhang, B. Wang, G. Wang, C. Shen, J. Chen, G. Reiter, B. Zhang, *Macromolecules* **2020**, *53*, 9631–9640.

[145] L. Li, X. Jia, Q. Dong, J. Zhou, W. Li, *Macromolecules* **2023**, *56*, 5932–5940.

[146] M. J. Fasolka, P. Banerjee, A. M. Mayes, G. Pickett, A. C. Balazs, *Macromolecules* **2000**, *33*, 5702–5712.

[147] R. V. Castillo, M. L. Arnal, A. J. Müller, I. W. Hamley, V. Castelletto, H. Schmalz, V. Abetz, *Macromolecules* **2008**, *41*, 879–889.

[148] C. D. Bain, E. B. Troughton, Y. T. Tao, J. Evall, G. M. Whitesides, R. G. Nuzzo, *Journal of the American Chemical Society* **1989**, *111*, 321–335.

[149] S. Sugden, *J. Chem. Soc., Trans.* **1924**, *125*, 1177–1189.

[150] G. Dee, T. Ougizawa, D. Walsh, *Polymer* **1992**, *33*, 3462–3469.

[151] J. D. Hoffman, *Polymer* **1991**, *32*, 2828–2841.

[152] J. D. Hoffman, R. L. Miller, *Polymer* **1997**, *38*, 3151–3212.

[153] Y. K. Godovsky, G. L. Slonimsky, N. M. Garbar, *Journal of Polymer Science Part C: Polymer Symposia* **1972**, *38*, 1–21.

[154] F. Zhang, Y. Chen, H. Huang, Z. Hu, T. He, *Langmuir* **2003**, *19*, 5563–5566.

[155] Z. Püspöki, M. Storath, D. Sage, M. Unser in *Focus on Bio-Image Informatics*, (Eds.: W. H. De Vos, S. Munck, J.-P. Timmermans), Springer International Publishing, Cham, **2016**, pp. 69–93.

[156] J. Zhang, X. Yu, P. Yang, J. Peng, C. Luo, W. Huang, Y. Han, *Macromolecular Rapid Communications* **2010**, *31*, 591–608.

[157] A. Löfstrand, A. Vorobiev, M. Mumtaz, R. Borsali, I. Maximov, *Polymers* **2022**, *14*, 654.

[158] T. Ghoshal, C. Ntaras, J. O'Connell, M. T. Shaw, J. D. Holmes, A. Avgeropoulos, M. A. Morris, *Nanoscale* **2016**, *8*, 2177–2187.

[159] D. David, T. Sincock, *Polymer* **1992**, *33*, 4505–4514.

[160] C. M. Hansen, *Hansen Solubility Parameters: A User's Handbook*, Second Edition (2nd ed.), CRC Press, **2007**.

[161] K. Brassat, J. K. N. Lindner, *Advanced Materials Interfaces* **2020**, *7*, 1901565.

[162] C. van Oss, *Interfacial Forces in Aqueous Media*, 2nd ed., CRC Press, **2006**.

[163] K. Brassat, D. Kool, J. Bürger, J. K. N. Lindner, *Nanoscale* **2018**, *10*, 10005–10017.

[164] A. Knoll, A. Horvat, K. S. Lyakhova, G. Krausch, G. J. A. Sevink, A. V. Zvelindovsky, R. Magerle, *Phys. Rev. Lett.* **2002**, *89*, 035501.

# 8. Appendix

## Contents

# Mapping the nanoscale elastic property modulations of polypyrrole thin films in liquid electrolyte with EC-AFM

*Alexander Meinhardt[1,2], Pirmin Lakner[1,2], Patrick Huber[1,3,4], Thomas F. Keller[1,2*]*

[1]Centre for X-ray and Nano Science (CXNS), Deutsches Elektronen-Synchrotron DESY, Hamburg, Germany

[2]Department of Physics, University of Hamburg, Hamburg, Germany

[3]Hamburg University of Technology, Institute for Materials and X-Ray Physics, Hamburg, Germany

[4]Center for Hybrid Nanostructures CHyN, Hamburg University, Hamburg, Germany

Keywords: polypyrrole, conductive polymer, electropolymerization, in situ EC-AFM, Young modulus, elastic properties, electrochemistry

**Supporting Information**

Details of the electrochemical cell used for electropolymerization, the in situ AFM setup, cyclic voltammogram and complementary AFM data.

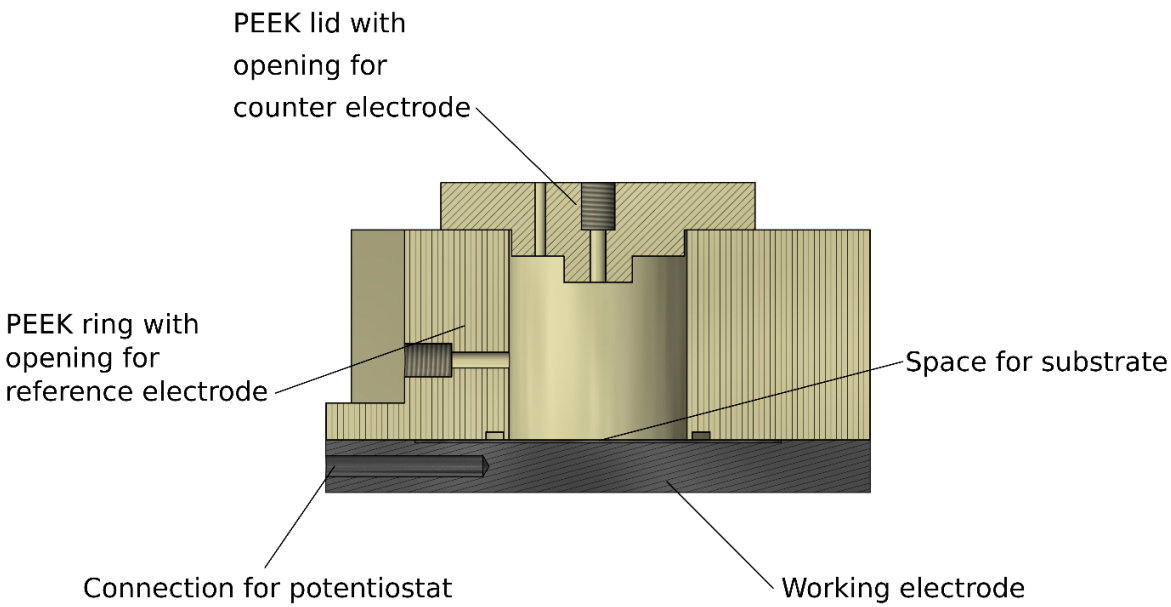


**Figure S1.** EC cell used for electropolymerization of PPy thin film.

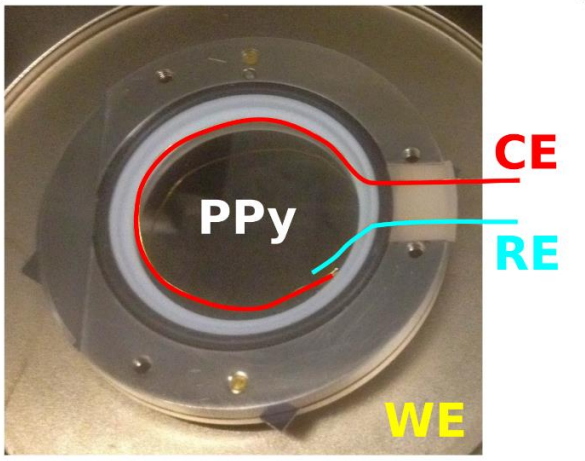


**Figure S2.** Fluid AFM cell with electrode arrangement used for the *in situ* electrochemistry experiments.

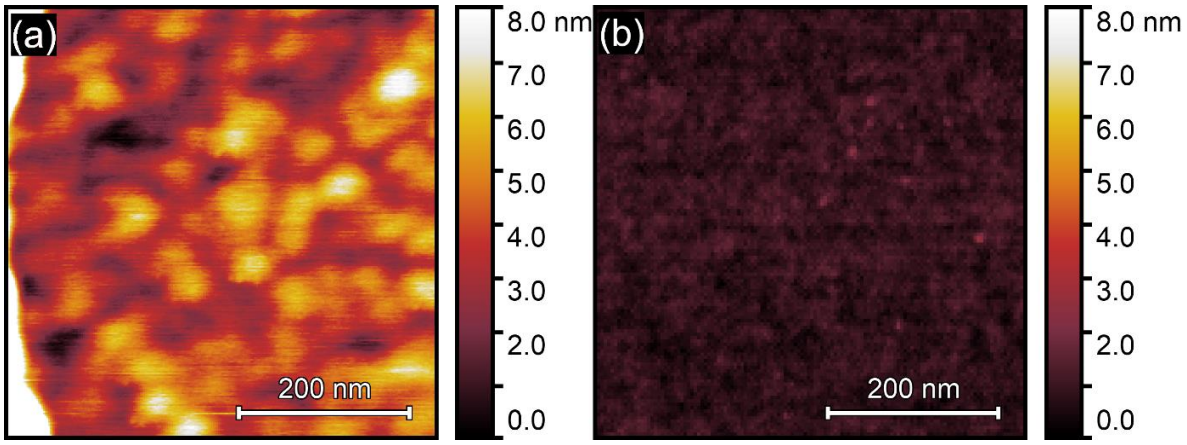


**Figure S3.** AFM tapping mode height image in air showing the surface roughness of substrate area that was previously covered by PPy (left). Some residual PPy may cause the roughness. Clean Si substrate without any PPy showing clearly lower surface roughness (right).

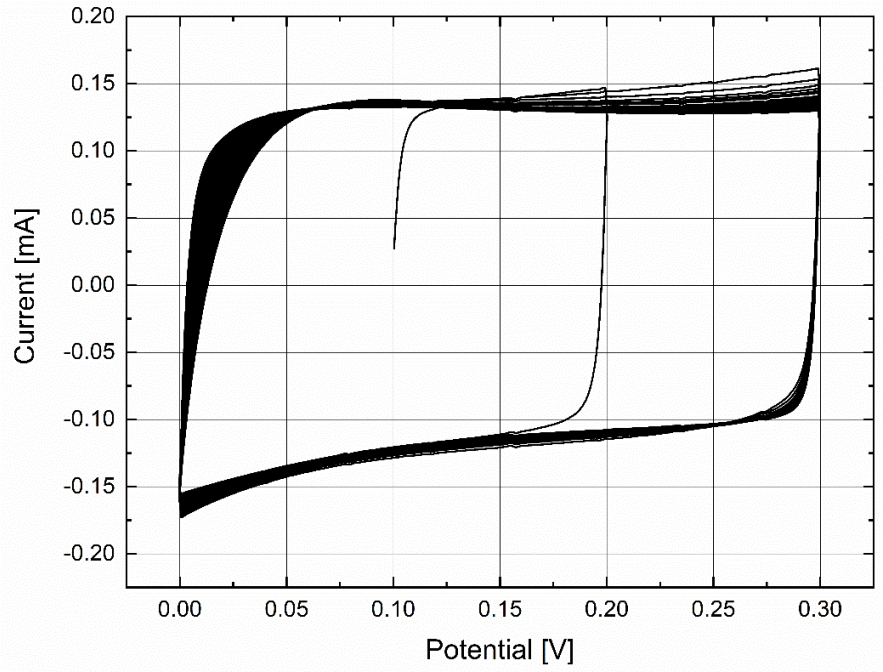


**Figure S4.** Cyclic voltammogram of PPy film ranging from 0.0 V to 0.3 V with a potential cycling rate of 10 mV/s for 50 cycles during the *in situ* EC AFM experiments. The box-like shape indicates that no faradaic processes or degradation take place within the chosen potential window.

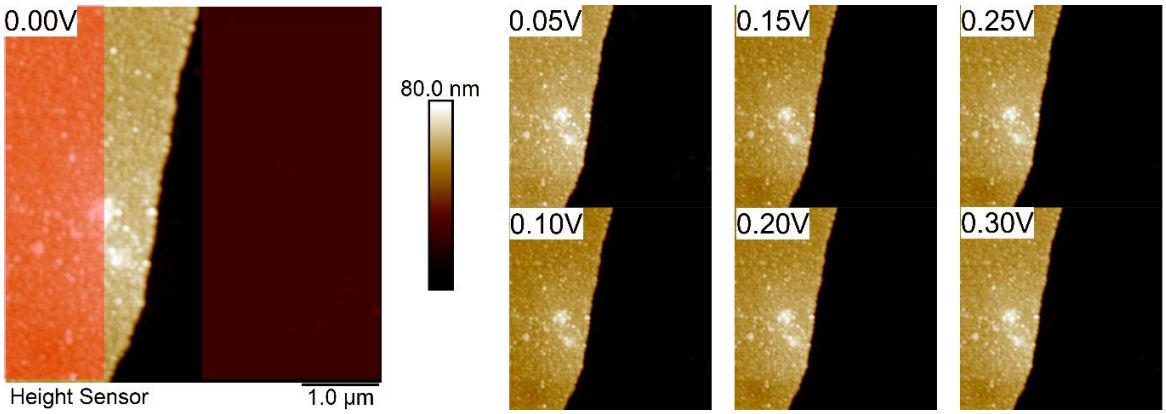


**Figure S5.** AFM images taken at every potential step for the static method. The average film thickness is determined from the marked areas.

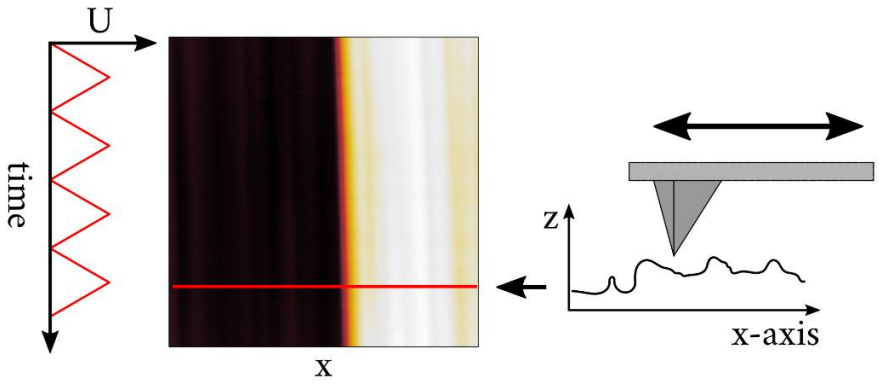


**Figure S6.** Schematic image illustrating how the dynamic method works. The AFM tip scans repeatedly over the same line while the electrical potential is varied.

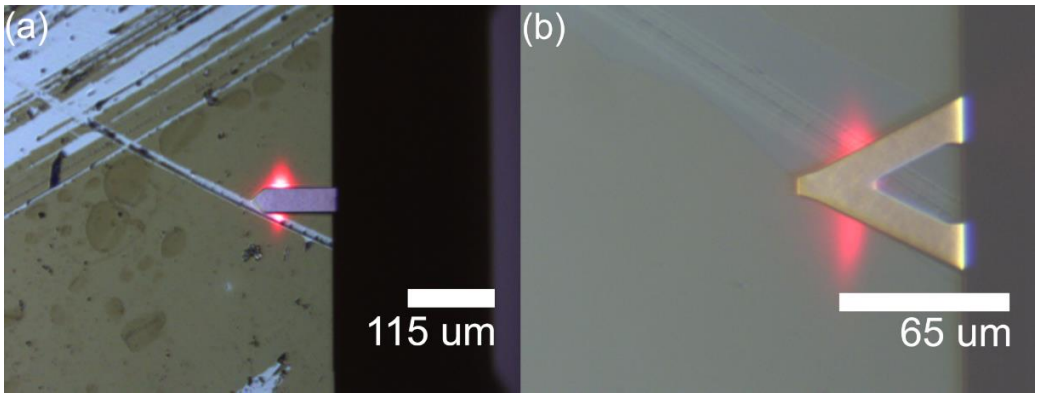


**Figure S7.** Optical microscopy images recorded by the build-in optical microscope of the AFM. In (a), a rectangular silicon tapping mode cantilever (RTESPA-300, Bruker) scans across a scratch of the polypyrrole film. In (b), a similar scan is performed in fluid using a triangular silicon nitride cantilever (SCANASYST-FLUID+).

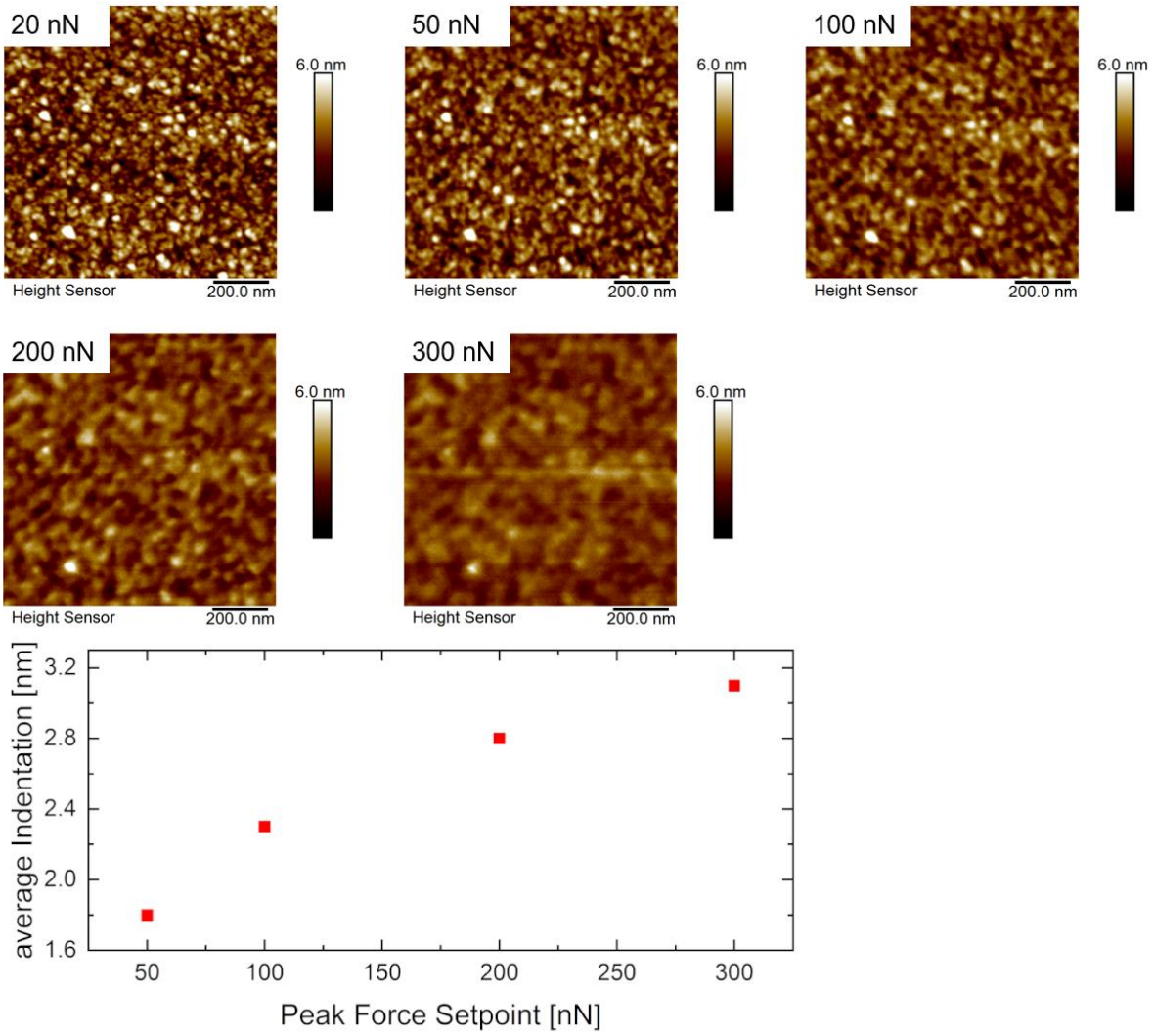


**Figure S8.** QNM-AFM images of the polypyrrole film topography measured at different maximum force setpoints. The higher force leads to larger indentation depth, but also clearly damages the film.

# Supporting Information

## A pathway towards sub-10 nm surface nanostructures utilizing block copolymer crystallization control

*Alexander Meinhardt*, Peng Qi, Christian David, Ivan Maximov, Thomas F. Keller**

A. Meinhardt, T. F. Keller
Centre for X-ray and Nano Science CXNS, Deutsches Elektronen-Synchrotron (DESY), 22607 Hamburg, Germany
Department of Physics, University of Hamburg, 22607 Hamburg, Germany
E-mail: alexander.meinhardt@desy.de, thomas.keller@desy.de

P. Qi, C. David
Paul Scherrer Institut, 5232 Villigen PSI, Switzerland

I. Maximov
NanoLund and Solid State Physics, Lund University, Box 118, SE-221 00 Lund, Sweden

### Extended crystalline PE-b-PEO chain length calculation

Due to the tendency of crystallizable short chain oligomers to form extended chain crystals, one can calculate the block length and corresponding extended chain length $d_{ext}$ from the molar mass:

$$\mathrm{M_n} = 2250 \frac{\mathrm{g}}{\mathrm{mol}} \text{with 80 wt\% PEO}$$

c-axis of orthorhombic PE:

$$c_{PE} = 0.2546 \text{ nm}$$

and monoclinic PEO (7/2 helix)[1]:

$$c_{PEO} = 1.948 \text{ nm}$$

Molar masses of PE and PEO block:

$$M_n(PE) = 450 \frac{\mathrm{g}}{\mathrm{mol}}$$

$$M_n(PEO) = 2250 * 0.8 = 1800 \frac{\mathrm{g}}{\mathrm{mol}}$$

Masses of PE and PEO blocks, as well as mass of a PE/PEO mer unit:

$$m_{PE-block} = \frac{M_n(PE)}{N_A} = \frac{450}{6.022 * 10^{23}} \frac{\frac{\text{g}}{\text{mol}}}{\frac{1}{\text{mol}}} = 7.473 * 10^{-22}\text{g}$$

$$m_{PEO-block} = \frac{M_n(PEO)}{N_A} = \frac{1800}{6.022 * 10^{23}} \frac{\frac{\text{g}}{\text{mol}}}{\frac{1}{\text{mol}}} = 2.989 * 10^{-21}\text{g}$$

$$m_{E-mer} = \frac{M_E}{N_A} = \frac{28\,\frac{\text{g}}{\text{mol}}}{6.022 * 10^{23}\,\frac{1}{\text{mol}}} = 4.650 * 10^{-23}\text{g}$$

$$m_{EO-mer} = \frac{M_{EO}}{N_A} = \frac{44\,\frac{\text{g}}{\text{mol}}}{6.022 * 10^{23}\,\frac{1}{\text{mol}}} = 7.307 * 10^{-23}\text{g}$$

Number of PE/PEO repeating units:

$$N_{PE} = \frac{m_{PE-block}}{m_{E-mer}} = \frac{7.473 * 10^{-22}\text{g}}{4.650 * 10^{-23}\text{g}} = 16.071 \approx 16\ \text{PE units}$$

$$N_{PEO} = \frac{m_{PEO-block}}{m_{EO-mer}} = \frac{2.989 * 10^{-21}\text{g}}{7.307 * 10^{-23}\text{g}} = 40.906 \approx 41\ \text{PEO units}$$

Extended chain length of fully crystalline PE-b-PEO (PE has a 22° angle to accommodate the different crystal structures):

$$d_{ext} = 16 * 0.2546\ \text{nm} * \cos(22°) + 41 * \left(\frac{1.948}{7}\text{nm}\right)$$
$$= 3.777\ \text{nm (PE)} + 11.410\ \text{nm (PEO)} = 15.187\ \text{nm}$$

**Molar volumes of PE/PEO taken from literature for surface tension calculation**

**Table S1.** Overview of specific volumes and molar volumes of PE and PEO at different temperatures calculated from reported measurements of a PE homopolymer analogue ($C_{36}H_{84}$) and a PEO homopolymer analogue ($M_n$=1540 g mol$^{-1}$) by Dee et al.[2]

| $T$ [°C] | $\rho_{PE}^{-1}$ [mL g$^{-1}$] | $\rho_{PEO}^{-1}$ [mL g$^{-1}$] | $V_{m,PE}$ [mL mol$^{-1}$] | $V_{m,PEO}$ [mL mol$^{-1}$] |
|---|---|---|---|---|
| 120 | 1.33 | 0.95 | 37.24 | 41.8 |
| 80 | - | 0.92 | - | 40.48 |
| 40 | - | 0.90 | - | 39.6 |

**Estimation of $\chi$ from solubility parameters**

The Flory-Huggins interaction parameter $\chi$ can be estimated using the Hildebrand solubility parameters for PE and PEO:[3–6]

Segregation appears at:

$$\chi_{crit} = \frac{1}{2}\left(\frac{1}{\sqrt{N_A}} + \frac{1}{\sqrt{N_B}}\right)^2 = 0.5 * \left(\frac{1}{\sqrt{16}} + \frac{1}{\sqrt{41}}\right)^2 = 0.0825$$

Formula for $\chi$:

$$\chi_{12} \cong \frac{V}{RT}(\delta_1 - \delta_2)^2$$

With molar volume V (geometric mean), and the Hildebrand solubility parameters $\delta_{1,2}$.
The solubility parameter can be divided into their dispersive, polar, and hydrogen bonding parts as shown by Hansen[6]:

$$\delta = \sqrt{\delta_d^2 + \delta_p^2 + \delta_h^2}\ [MPa^{0.5}]$$

Each component can be calculated using group contributions (e.g., Hoftyzer-Van Krevelen, see **Table S2** and **Table S3**):

$$\delta_d = \frac{\Sigma \mathrm{F_{di}}}{V} \text{ and}$$

$$\delta_p = \frac{\mathrm{sqrt}\left(\Sigma \mathrm{F_{pi}^2}\right)}{V} \text{ and}$$

$$\delta_h = \mathrm{sqrt}\left(\frac{\Sigma E_{hi}}{V}\right)$$

And the molar volumes ($\rho_{PE}$ = 0.94 g mL$^{-1}$ and $\rho_{PEO}$ = 1.125 g mL$^{-1}$ from literature):

$$V_{m,PE} = 29.787\ \frac{\mathrm{cm^3}}{\mathrm{mol}}$$

$$V_{m,PEO} = 39.111 \frac{\mathrm{cm^3}}{\mathrm{mol}}$$

**Table S2.** Solubility parameter group contributions for the functional groups of PE and PEO[3]

| structural group: | $F_{di}\left[\sqrt{\mathrm{MPa}} * \mathrm{cm^3} * \mathrm{mol^{-1}}\right]$ | $F_{pi}\left[\sqrt{\mathrm{MPa}} * \mathrm{cm^3} * \mathrm{mol^{-1}}\right]$ | $E_{hi}\left[\frac{\mathrm{J}}{\mathrm{mol}}\right]$ |
|---|---|---|---|
| $-\mathrm{CH_2}-$ | 270 | 0 | 0 |
| $-\mathrm{O}-$ (ether) | 100 | 400 | 3000 |

**Table S3.** Overview of the calculated solubility parameters.

| | $\delta_d$ | $\delta_p$ | $\delta_h$ | $\delta\left[\sqrt{\mathrm{MPa}}\right]$ |
|---|---|---|---|---|
| PE | 18.129 | 0 | 0 | 18.129 |

| | | | | |
|---|---|---|---|---|
| PEO | 16.364 | 10.227 | 8.758 | 21.191 |

Flory-Huggins interaction parameter $\chi$ at room temperature:

$$\chi_{PE-PEO} \cong \frac{\sqrt{V_{PE} * V_{PEO}}}{RT}(\delta_{PE} - \delta_{PEO})^2$$

$$= \frac{\sqrt{29.787 * 10^{-6} * 39.111 * 10^{-6}}\,\frac{\mathrm{m}^3}{\mathrm{mol}}}{8.314\,\frac{\mathrm{J}}{\mathrm{mol} * \mathrm{K}} * 300\ \mathrm{K}} * \left(18.129\,\sqrt{\mathrm{MPa}} - 21.191\,\sqrt{\mathrm{MPa}}\right)^2 = 0.128$$

At 120 °C during the thermal annealing:

$$\chi_{PE-PEO} = 0.096$$

Close to $\chi_{crit}$ = 0.0825 for isotropic melt structure.

Segregation strength:

$$\rightarrow \chi * N = 0.128 * 57 = 7.296$$

PE-b-PEO is not necessarily strongly segregating due to the very short chains, but the crystallization likely supports the microphase segregation, especially since the crystallization of the blocks is sequential ($T_{c,PE} > T_{c,PEO}$). However, these calculations only show a general trend. The actual values can be significantly different, depending on the chosen densities, molar volumes, and solubility parameters.[7]

**PE/PEO surface energy and interfacial energy calculations**

To calculate the surface tensions of the PE and PEO blocks in their respective melt state, we estimate the surface tension $\gamma$ of the copolymer block melts from the parachor $\mathbf{P_s}$, an additive function of atomic and functional group contributions originally introduced by Sudgen, and the temperature dependent molar volume **V**, as shown in below:[3,8]

$$\gamma = \left(\frac{\mathbf{P_s}}{\mathbf{V}}\right)^4$$

We use the values assigned by Sudgen for the structural contribution to the parachor of PE (78 $(\mathrm{mJ\ m^{-2}})^{1/4}$ $(\mathrm{mL\ mol^{-1}})$) and PEO (98 $(\mathrm{mJ\ m^{-2}})^{1/4}$ $(\mathrm{mL\ mol^{-1}})$) and the temperature dependent molar volumes of PE and PEO extracted from measurements of homopolymer analogues with similar molar mass reported by Dee et al. as given in **Table S1**.[2] Our estimations yield a surface

tension of 19.2 mJ $m^{-2}$ for the PE block at 120 °C, while the surface tension of the PEO block ranges from 30.2 mJ $m^{-2}$ at 120 °C to 37.5 mJ $m^{-2}$ at 40 °C.

For temperatures below the respective $T_c$ of the PE (~80 °C) and PEO (~30 °C) oligomer blocks in the BCP, the crystallizing chains form anisotropic polymer crystals with a significantly different surface energy compared to the amorphous state.

Crystallizable short chain oligomers tend to form extended chain crystals as a result of their limited length and, in consequence, low conformational entropy. Crystal surface energies of PE and PEO extended chain crystals have been estimated from crystallization studies by investigating crystallization kinetics from calorimetry. Literature values for the surface energy of a ciliated surface of extended chain PE crystals of around 23 – 29 mJ $m^{-2}$ have been reported. For the ciliated surface of extended chain PEO crystals, values of 15 – 17 mJ $m^{-2}$ were found. The lateral crystal surfaces of PE and PEO extended chain crystals were found to be 13.8 mJ $m^{-2}$ and 9.8 mJ $m^{-2}$, respectively.[9–12] In summary, **Figure 3** shows an overview of the temperature dependent changes of free surface energies of the PE, the PEO, and the M3M from 120 °C to 20 °C.

The either symmetric, asymmetric, or neutral wetting conditions depend on the interfacial energies of the co-oligomer blocks with the air and substrate interface. The co-oligomer block with the lowest surface energy will generally favor exposure to the air and migrate to the air interface, while the co-oligomer block with the lowest substrate interfacial energy will migrate to the substrate interface. In the case of neutral wetting, both blocks will favor exposure to air and substrate interface. The wetting affinity of the co-oligomers with M3M can be estimated by comparing the surface energy differences between the M3M and both copolymer blocks. Taking both the dispersive and polar contributions to the surface tension into account, the Owens-Wendt formula shown below can be used to calculate the interfacial energy between the oligomer blocks and the M3M, thus offering an accurate description of the interactions:[13,14]

$$\gamma_{A-S} = \gamma_A + \gamma_S - 2\sqrt{\gamma_A^d \gamma_S^d} - 2\sqrt{\gamma_A^p \gamma_S^p}$$

with the interfacial energy $\gamma_{A\text{-}S}$, the surface energy of oligomer and substrate $\gamma_{A,S}$, and the disperse $\gamma^d_{A,S}$ and polar $\gamma^p_{A,S}$ contributions to the surface energy of oligomer and substrate, where the indices A and S refer to an oligomer block A and the substrate S.

The interfacial energies of the PE and PEO with the M3M are shown in Figure 3 B. Since the co-oligomer block with the lowest interfacial energy will preferably wet the substrate, the formation of crystalline lamellae upon crystallization may lead to a change in orientation caused by the appearance of the lateral and ciliated crystal surfaces.

**Self-assembled monolayer (M3M) surface energy**

*Monolayer surface energy calculation (OWRK):*

The surface energy of the M3M functionalized substrate can be determined by the Owens, Wendt, Rabel and Kälble (OWRK) method of measuring the advancing contact angles of liquids with different polarities on the sample. Extensive literature exists on thiol-functionalized self-assembled monolayers on gold. It is known that the terminal tail group of the organic compound determines the surface energy.[15] The M3M tail group is a methyl ether functionality. Similar compounds have been investigated by Bain et al., who performed contact angle measurements with hexadecane (Θ = 35°) and water (Θ = 74°) on $HS(CH_2)_{11}OCH_3$ on a gold surface.[15] Control measurements confirmed the M3M functionalized substrate possesses nearly the same water contact angle. From the polar and disperse components of the liquids surface tensions, one can use the linearized OW formula to calculate the surface tension of the M3M surface.

**Table S4.** Surface tensions of water and hexadecane including their disperse and polar contributions.

| | $\gamma$ [mJ m$^{-2}$] | $\gamma_{Disperse}$ [mJ m$^{-2}$] | $\gamma_{Polar}$ [mJ m$^{-2}$] |
|---|---|---|---|
| water[3] | 72.8 | 21.8 | 51.0 |
| hexadecane[16] | 27.6 | 27.6 | 0 |

Combining the OWRK equation (geometric means of dispersion and polar components of liquid and solid):[14]

$$\gamma_{sl} = \gamma_s + \gamma_l - 2\sqrt{\gamma_s^d \gamma_l^d} - 2\sqrt{\gamma_s^p \gamma_l^p}$$

And Young's equation:

$$\gamma_l \cos\theta_C = \gamma_s - \gamma_{sl}$$

Yields:

$$\rightarrow \gamma_l \cos\theta_C = \gamma_s - \gamma_s - \gamma_l + 2\sqrt{\gamma_s^d \gamma_l^d} + 2\sqrt{\gamma_s^p \gamma_l^p}$$

$$\rightarrow \gamma_l \cos\theta_C = -\gamma_l + 2\sqrt{\gamma_s^d \gamma_l^d} + 2\sqrt{\gamma_s^p \gamma_l^p}$$

$$\rightarrow \gamma_l(1 + \cos\theta_C) = 2\sqrt{\gamma_s^d \gamma_l^d} + 2\sqrt{\gamma_s^p \gamma_l^p}$$

$$\rightarrow \frac{\gamma_l(1 + \cos\theta_C)}{2} = \sqrt{\gamma_s^d \gamma_l^d} + \sqrt{\gamma_s^p \gamma_l^p}$$

$$\rightarrow \frac{\gamma_l(1 + \cos\theta_C)}{2\sqrt{\gamma_l^d}} = \sqrt{\frac{\gamma_l^p}{\gamma_l^d}} * \sqrt{\gamma_s^p} + \sqrt{\gamma_s^d}$$

After linearization, the values for the polar and disperse contribution of the substrate can be extracted from a linear fit of the data shown below in

**Figure S1**

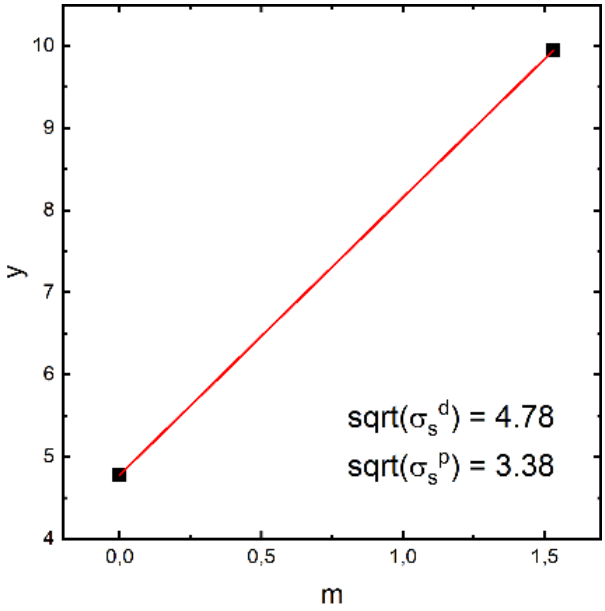


**Figure S1.** OWRK plot of the linearized equation with a linear fit in red.

Plotting the results of the linear regression yields $\gamma_s^d$ = 22.85 mJ m$^{-2}$ and $\gamma_s^p$ = 11.42 mJ m$^{-2}$. The total surface tension is the sum of disperse and polar surface tensions:

$$\gamma_s = \gamma_s^d + \gamma_s^p = 34.27 \text{ mJ m}^{-2}$$

*Calculation of the temperature dependence:*

We use the Parachor-equation for estimating the surface energy at elevated temperatures for the functionalized monolayer from the temperature dependent molar density. The M3M molecules are covalently tethered to the Au sputtered substrate. Therefore, the relative

thermal expansion of the Au lattice should lead directly to a proportional change in molar density of the M3M monolayer. Using the linear thermal expansion coefficient of Au ($\alpha$ = 14.2 * $10^{-6}$ $K^{-1}$) and the Au lattice constant ($d_{Au}$ = 407.82 pm) for a temperature window of $\Delta T$ = 120 – 20 = 100 K yields:

$$\Delta L \approx \alpha * L * \Delta T$$

$$\rightarrow \frac{\Delta L}{L} = \alpha \Delta T = 0.00142\ (+0.142\%)$$

And for a square sample area:

$$A = L^2 \rightarrow A' = L'^2\ with\ L' = L + \Delta L$$

$$\rightarrow A' = L^2 + 2\Delta L * L + \Delta L^2$$

The relative area changes by:

$$\rightarrow \frac{A'}{A} = 1 + \frac{\Delta L^2}{L^2} + 2 * \frac{\Delta L}{L} = 1 + 0.00142^2 + 2 * 0.00142 = 1.00284\ (+0.284\%)$$

Using Equation 1 (since only the tail group density is relevant for the surface energy, we use area instead of volume):

$$\frac{\sigma_{M3M}(120°C)}{\sigma_{M3M}(20°C)} = \left(\frac{P_s}{A_m(120°C) * d}\right)^4 : \left(\frac{P_s}{A_m(20°C) * d}\right)^4$$

With $A_m(120°C) = 1.00284 * A_m(20°C)$ leads to:

$$\ldots = \frac{A_m(20°C)}{1.00284 * A_m(20°C)} = \frac{1}{1.00284} = 0.99717\ (-0.283\%)$$

Therefore, our calculations show that the temperature dependent decrease in surface energy of the M3M functionalized monolayer going from 20 °C to 120 °C can be neglected.[17]

**Large AFM height scans of PE-b-PEO while heating**

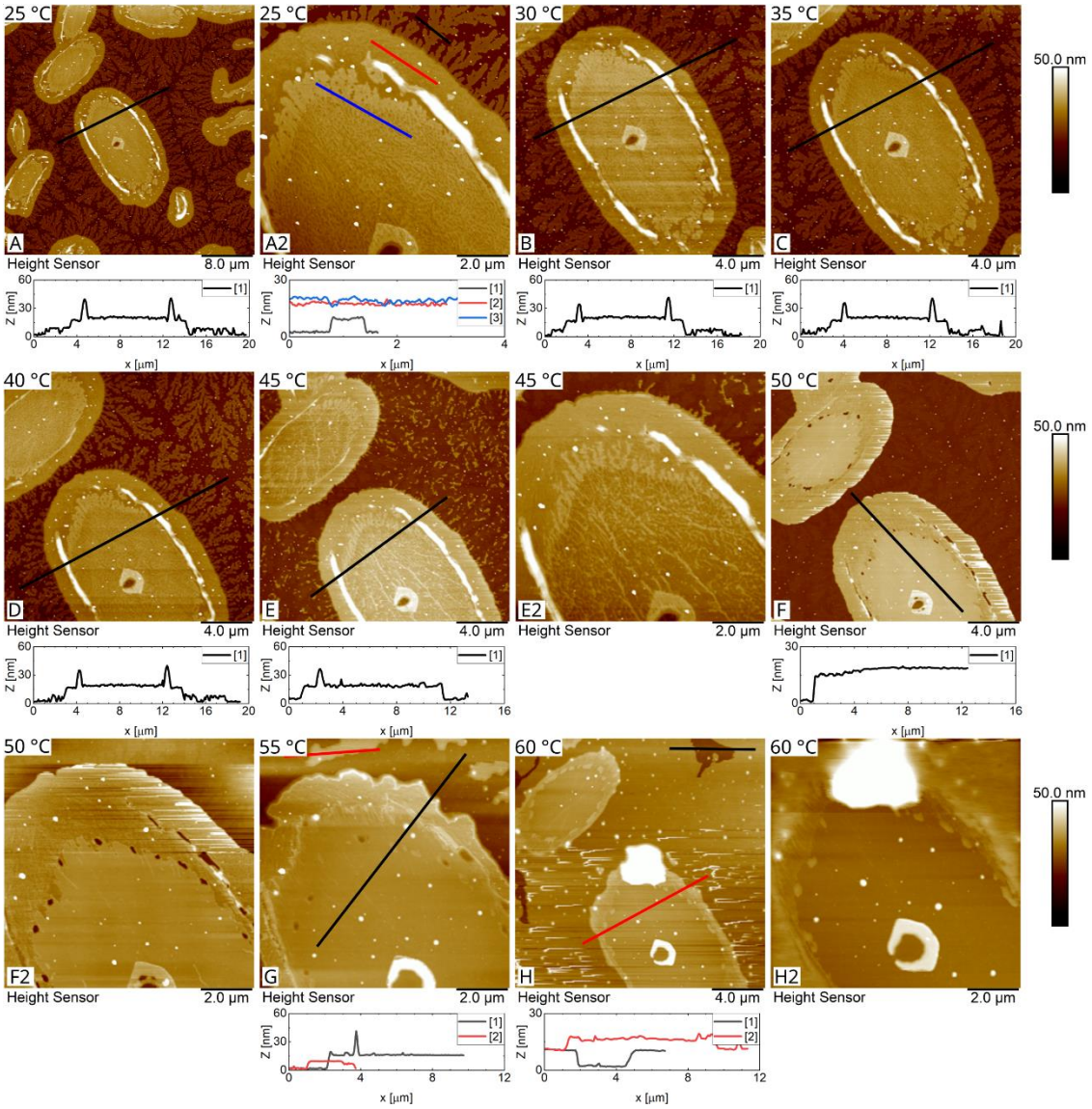


**Figure S2.** (A-N) Large in situ AFM images of heating process (height, from 25 to 120 °C).

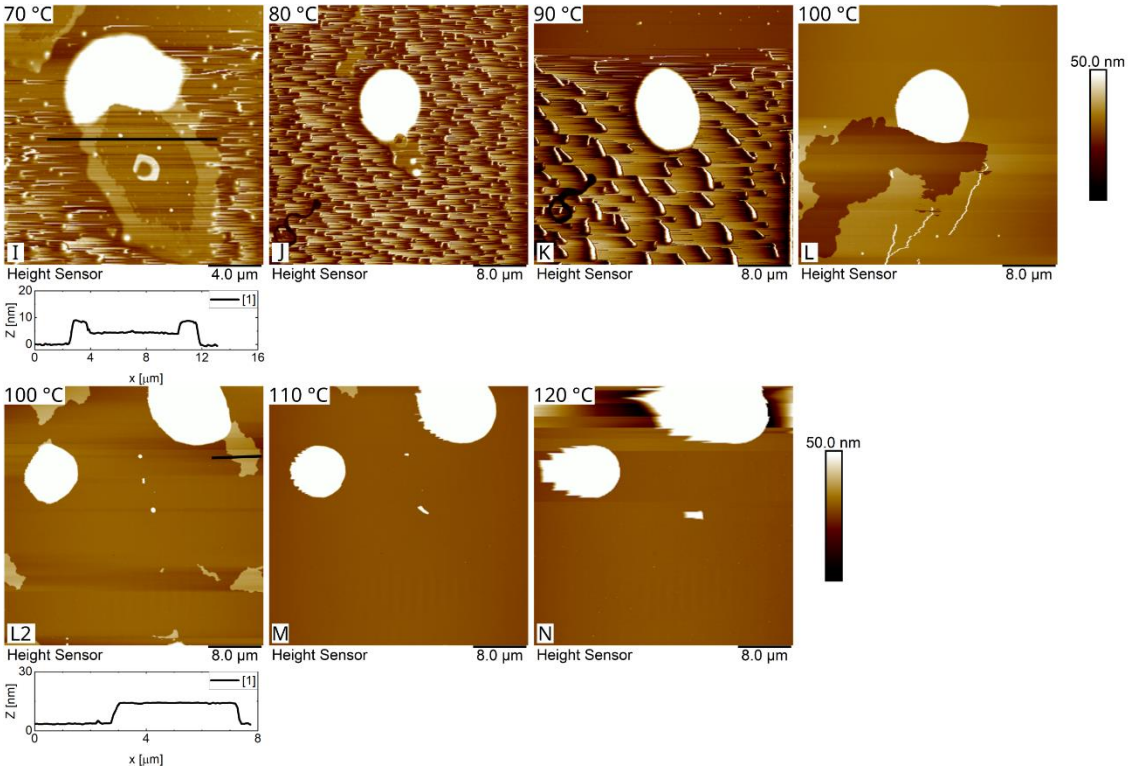


(Figure S2 continued)

**Droplets change height with temperature**

Chains diffuse to the existing droplets while heating up. Upon cooling, the droplets then function as reservoir for the lateral PE-b-PEO island layer growth and shrink with decreasing temperature.

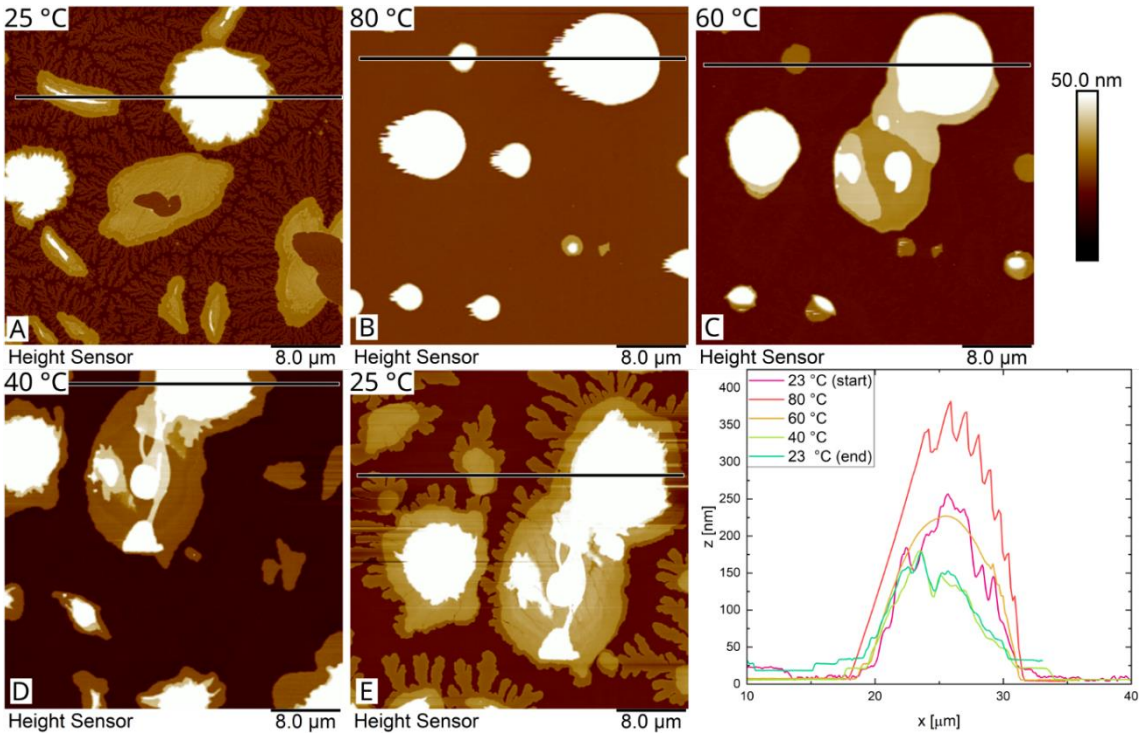


**Figure S3.** AFM images and line profiles performed on the droplets/agglomerates during heating/cooling show the migration of material from/to the droplets.

**Dendrite surface topography**

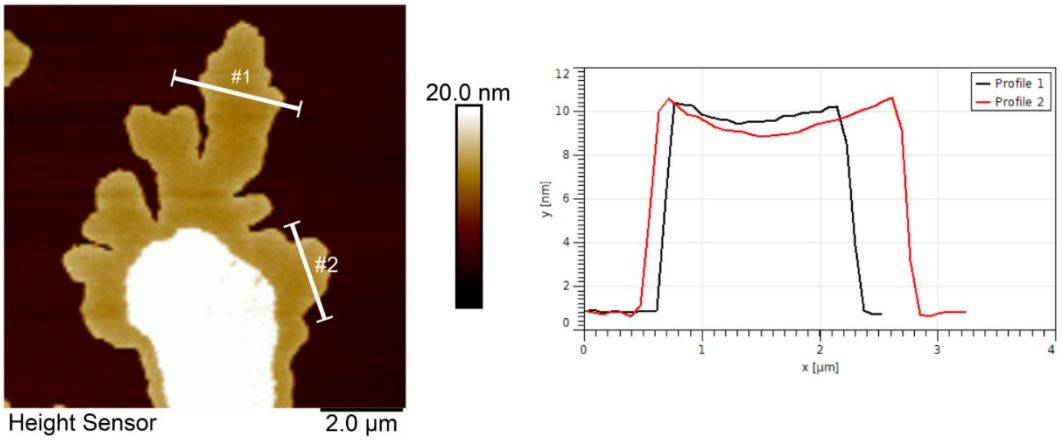


**Figure S4.** AFM height image of the PE-b-PEO dendrite area. The line profiles on the right show that the finger-like structures are not perfectly planar. Instead, the rims of the fingers are slightly higher as the result of chain reorientation during growth, similarly as described by Sommer et al.[18]

References:

[1] R. Schulze, M. M. L. Arras, G. Li Destri, M. Gottschaldt, J. Bossert, U. S. Schubert, G. Marletta, K. D. Jandt, T. F. Keller, *Macromolecules* **2012**, *45*, 4740.

[2] G. T. Dee, T. Ougizawa, D. J. Walsh, *Polymer.* **1992**, *33*, 3462.

[3] D. W. Van Krevelen, *Properties of Polymers: Their Correlation with Chemical Structure; Their Numerical Estimation and Prediction from Additive Group Contributions: Fourth Edition*, **2009**.

[4] J. R. Fried, *Polymer Science & Technology*, Pearson, **2014**.

[5] D. DAVID, T. SINCOCK, *Polymer.* **1992**, *33*, 4505.

[6] C. M. Hansen, *Hansen Solubility Parameters*, CRC Press, **2007**.

[7] G. Miquelard-Garnier, S. Roland, *Eur. Polym. J.* **2016**, *84*, 111.

[8] S. Sugden, *J. Chem. Soc., Trans.* **1924**, *125*, 1177.

[9] G. Reiter, G. Castelein, P. Hoerner, G. Riess, J.-U. Sommer, G. Floudas, *Eur. Phys. J. E* **2000**, *2*, 319.

[10] J. D. Hoffman, *Polymer.* **1991**, *32*, 2828.

[11] J. D. Hoffman, R. L. Miller, *Polymer.* **1997**, *38*, 3151.

[12] Y. K. Godovsky, G. L. Slonimsky, N. M. Garbar, *J. Polym. Sci. Part C Polym. Symp.* **1972**, *38*, 1-21.

[13] K. Brassat, J. K. N. Lindner, *Adv. Mater. Interfaces* **2020**, *7*, DOI 10.1002/admi.201901565.

[14] D. K. Owens, R. C. Wendt, *J. Appl. Polym. Sci.* **1969**, *13*, 1741.

[15] C. D. Bain, E. B. Troughton, Y. T. Tao, J. Evall, G. M. Whitesides, R. G. Nuzzo, *J. Am. Chem. Soc.* **1989**, *111*, 321.

[16] C. J. van Oss, *Interfacial Forces in Aqueous Media, 2nd Edition*, CRC Press, Boca Raton, FL, **2006**.

[17] J.-P. Yang, Q. Liao, J.-J. Zhou, X. Jiang, X.-H. Wang, Y. Zhang, S.-D. Jiang, S.-K. Yan, L. Li, *Macromolecules* **2011**, *44*, 3511.

[18] J.-U. Sommer, G. Reiter, in *Adv. Polym. Sci.*, **2005**, 200, pp. 1–36.

## 8.3. Supporting Information - Solvent Vapor Annealing of PE-b-PEO

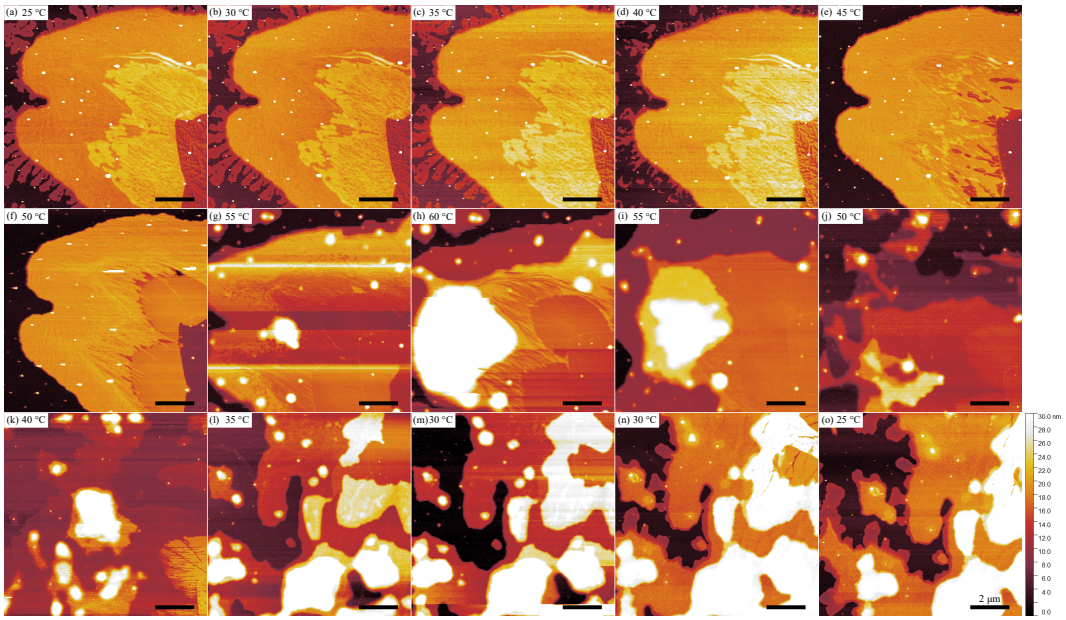


***SI. 8.1.*** In situ AFM height images ($10 \times 10$ $\mu$m) of a pre-annealed PE-*b*-PEO film (sample I) during SVA under ethanol vapor. The sample was heated to 60 °C and cooled back to room temperature. The images after (k) are rotated 90° counterclockwise.

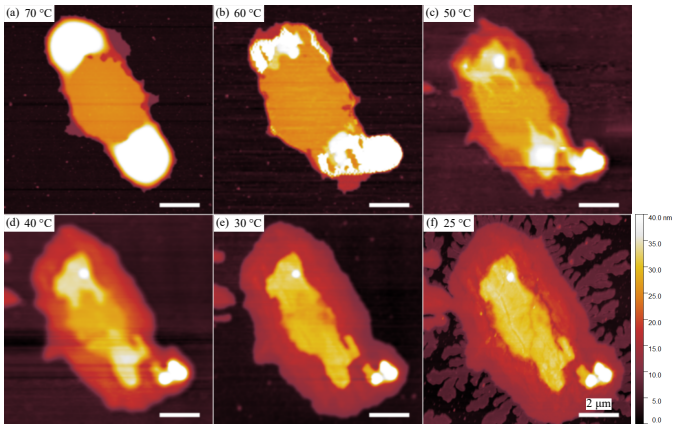


***SI. 8.2.*** In situ AFM height images (10 × 10 $\mu$m) of a pre-annealed PE-*b*-PEO film (sample II) during SVA under ethanol vapor. The sample was heated to 70 °C and cooled back to room temperature.

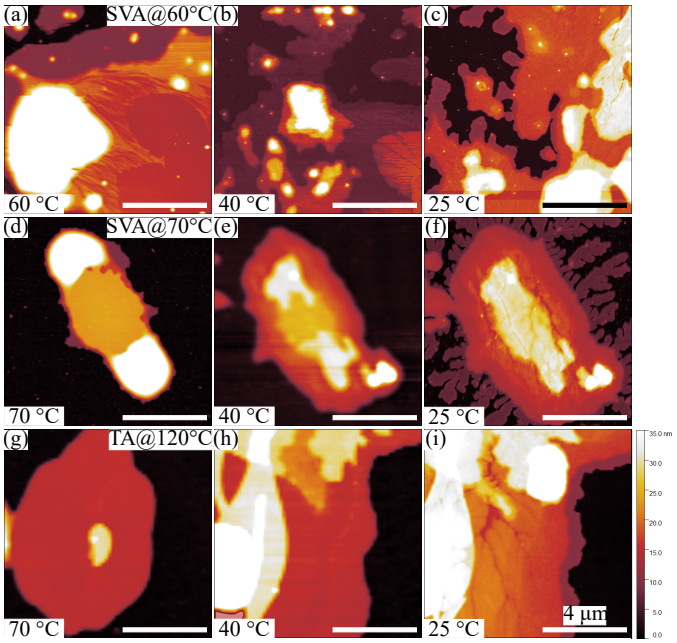


***SI. 8.3.*** AFM height images from Fig. 6.3.2 without the markings.

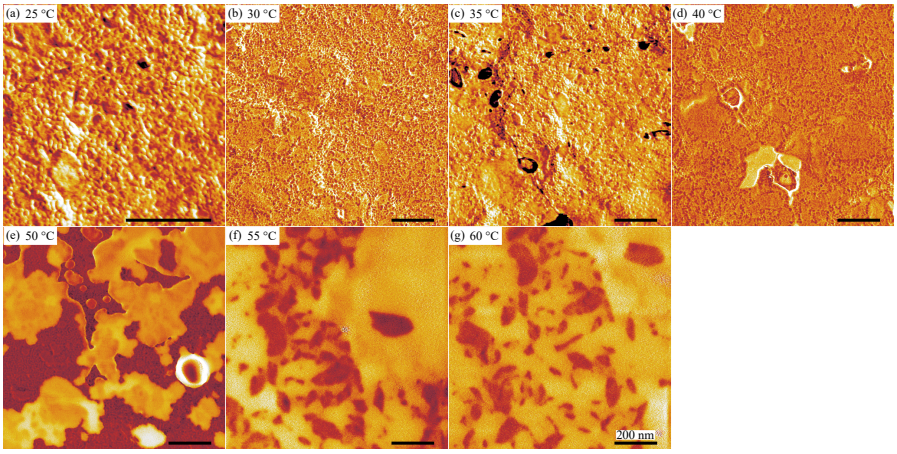


***SI. 8.4.*** In situ AFM phase images (1 × 1 $\mu$m) of an as-cast PE-*b*-PEO film (sample III) during SVA under ethanol vapor. The sample was heated to 60 °C while imaging.

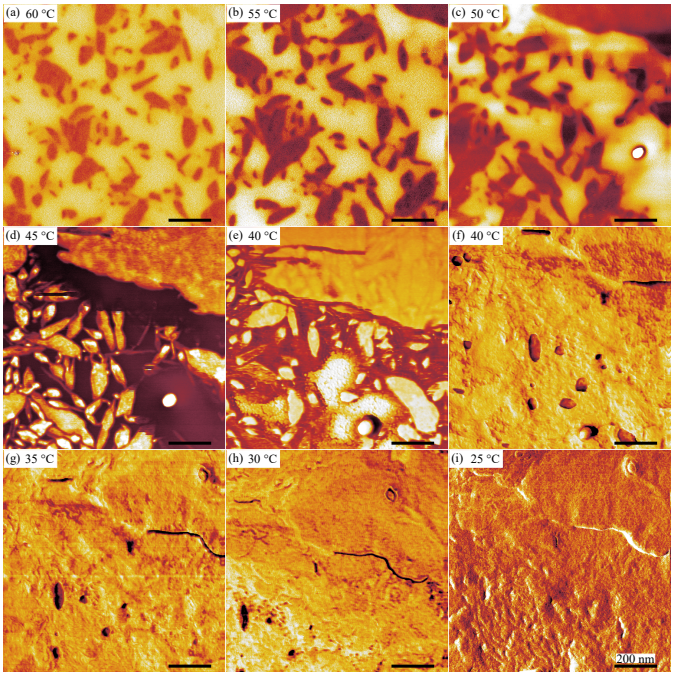


***SI. 8.5.*** Continuation of the in situ AFM phase images in Fig. 8.4 of an as-cast PE-*b*-PEO film (sample III) during SVA under ethanol vapor. The sample was cooled to room temperature after reaching 60 °C.

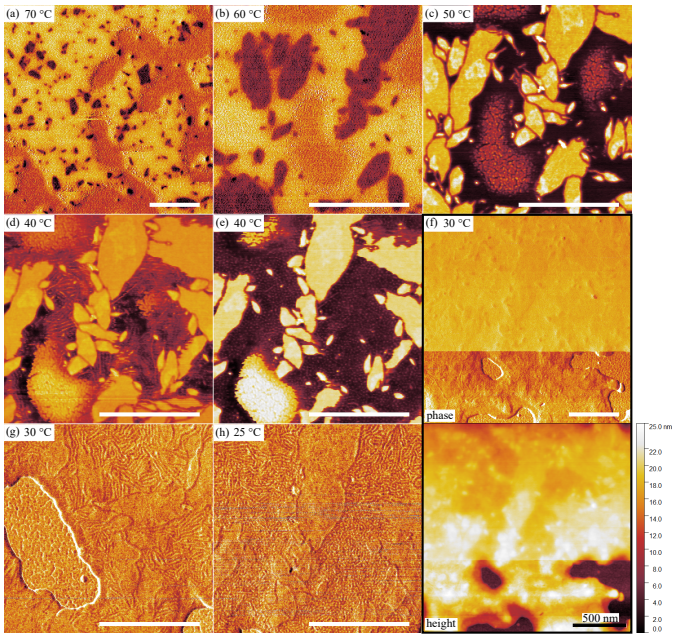


***SI. 8.6.*** In situ AFM phase images of an as-cast PE-*b*-PEO film (sample IV) during SVA under ethanol vapor. The sample was heated to 70 °C while imaging and then cooled back to room temperature. (a) and (f) are $2 \times 2$ $\mu$m scan size, (b-e) and (g-h) are $1 \times 1$ $\mu$m scan size. In (f) the phase and height are depicted.

# List of Publications

## As First-Author

A. Meinhardt, P. Qi, C. David, I. Maximov, and T. F. Keller, Mapping the nanoscale elastic property modulations of polypyrrole thin films in liquid electrolyte with EC-AFM, *Adv. Mater. Interfaces* **2025**, *12*, 2400661.

A. Meinhardt, P. Lakner, P. Huber, and T. F. Keller, A Pathway Toward Sub-10 nm Surface Nanostructures Utilizing Block Copolymer Crystallization Control, *Nanoscale Adv.* **2024**, *6*, 102 – 110.

## As Co-Author

S. Karmakar, M. K. Mukhopadhyay, M. K. Sanyal, A. Meinhardt, T. F. Keller, Evidence of quadratic time dependence of the kinetics in a continuous order-disorder transition, *Phys. Rev. B* **2025**, *111*, 024105.

S. Chen, C. Harder, I. Ribca, B. Sochor, E. Erbes, Y. Bulut, L. Pluntke, A. Meinhardt, B. Schummer, M. Oberthür, T. F. Keller, L. D. Söderberg, S. A. Techert, A. Stierle, P. Müller-Buschbaum, M. K. G. Johansson, J. Navarro, S. V. Roth, Sprayed water-based lignin colloidal nanoparticle-cellulose nanofibril hybrid films with UV-blocking ability, *Nanoscale Adv.* **2024**, *6*, 5031 – 5041.

Y. Bulut, B. Sochor, K. A. Reck, B. Schummer, A. Meinhardt, J. Drewes, S. Liang, T. Guan, A. Jeromin, A. Stierle, T. F. Keller, T. Strunskus, F. Faupel, P. Müller-Buschbaum, S. V. Roth, Investigating Gold Deposition with High-Power Impulse Magnetron Sputtering and Direct-Current Magnetron Sputtering on Polystyrene, Poly-4-vinylpyridine, and Polystyrene Sulfonic Acid, *Langmuir* **2024**, *40*, 22591 – 22601.

M. Kohantorabi, A. Ugolotti, B. Sochor, J. Roessler, M. Wagstaffe, A. Meinhardt, E. E. Beck, D. S. Dolling, M. B. Garcia, M. Creutzburg, T. F. Keller, M. Schwartzkopf, S. K. Vayalil, R. Thuenauer, G. Guédez, C. Löw, G. Ebert, U. Protzer, W. Hammerschmidt, R. Zeidler, S. V. Roth, C. Di Valentin, A. Stierle, H. Noei, Light-Induced Transformation of Virus-Like Particles on TiO2, *ACS Applied Materials & Interfaces* **2024**, *16*, 37275 – 37287.

Y. Bulut, B. Sochor, C. Harder, K. Reck, J. Drewes, Z. Xu, X. Jiang, A. Meinhardt, A. Jeromin, M. Kohantorabi, H. Noei, T. F. Keller, T. Strunskus, F. Faupel, P. Müller-Buschbaum, S. V. Roth, Diblock copolymer pattern protection by silver cluster reinforcement, *Nanoscale* **2023**, *15*, 15768 – 15774.

# Acknowledgements

Ich bin kein Freund langer Reden (oder Vorträgen), daher halte ich mich kurz: Ich danke meiner Familie für ihre Unterstützung und meinen Freunden, sowie meinen Kolleginnen und Kollegen vom DESY NanoLab. Insbesondere gilt mein Dank Thomas F. Keller für die zahlreichen fruchtbaren Diskussionen und seiner ständigen Unterstützung, auf die ich im Master und im PhD immer zählen konnte, sowie Katharina Röper, die beste Gruppensekretärin, die man sich wünschen kann. Mein Dank gilt vor allem den Kollegen und Kolleginnen, die häufig Kuchen mitgebracht haben und mit denen ich eine schöne Zeit hier am DESY hatte. Schlussendlich gilt mein Dank auch den Kooperationspartnern aus dem HELIOS Programm, dem PSI, Bruker, und der Basketball-Betriebssportgruppe.

## Eidesstattliche Versicherung

Hiermit versichere ich an Eides statt, die vorliegende Dissertationsschrift selbst verfasst und keine anderen als die angegebenen Hilfsmittel und Quellen benutzt zu haben.

Sofern im Zuge der Erstellung der vorliegenden Dissertationsschrift generative Künstliche Intelligenz (gKI) basierte elektronische Hilfsmittel verwendet wurden, versichere ich, dass meine eigene Leistung im Vordergrund stand und dass eine vollständige Dokumentation aller verwendeten Hilfsmittel gemäß der Guten wissenschaftlichen Praxis vorliegt. Ich trage die Verantwortung für eventuell durch die gKI generierte fehlerhafte oder verzerrte Inhalte, fehlerhafte Referenzen, Verstöße gegen das Datenschutz- und Urheberrecht oder Plagiate.

28.05.2025 J. Meichsner

Datum Unterschrift des Doktoranden

Ich versichere, dass dieses gebundene Exemplar der Dissertation und das in elektronischer Form eingereichte Dissertationsexemplar (über den Docata-Upload) und das bei der Fakultät (zuständiges Studienbüro bzw. Promotionsbüro Physik) zur Archivierung eingereichte gedruckte gebundene Exemplar der Dissertationsschrift identisch sind.

28.05.2025 J. Meichsner

Datum Unterschrift des Doktoranden